SHAPE MORPHING OF SOFT ACTIVE SHEETS

by
DANIELE BATTISTA

THESIS SUBMITTED IN PARTIAL FULFILLMENT OF THE

REQUIREMENTS FOR THE DEGREE OF

DOCTOR OF PHILOSOPHY

IN THE SUBJECT OF

THEORETICAL AND APPLIED MECHANICS

Sapienza University of Rome
Rome, Italy

Advisor:
Prof. Paola Nardinocchi

January 2022

ABSTRACT

Biological systems often exploit their capability to respond to environmental stimuli to achieve complex shapes and perform some necessary living functions. Inspired by nature, scientists developed synthetic soft active materials whose deformation is induced by non-mechanical actions, and that mimic, for example, the shape transformation of plants, in which a variety of organs such as flowers, leaves, pods and tendrils respond to variations of light, humidity or temperature. As in plants the tissue composition and its microstructural cell anisotropy play an important role, so also for synthetic materials the design of the material structure is fundamental for programming its final shape. Up to date, some exciting achievements have been made and successfully applied in a variety of fields, including biomedical devices, drug delivery, soft robotics, sensors and actuators.

This thesis aims to investigate the morphing of soft active sheets, focusing on flat metric structures such as beams, plates and cylindrical shells, via theoretical analysis, numerical simulation and experimental validation. The work focuses on those soft materials in which the morphing can be driven by elastic or inelastic growth such as gels, nematic elastomers or biological tissues. The adopted strategy to achieve bending is based on a through-the-thickness mismatch realized by stacking two homogeneous layers with different properties on top of each other. Specifically, three processes that induce bending in bilayer structures are explored: the differential swelling between two layers with different elastic moduli, the shrinking of a layer containing solvent glued to a passive layer, the diffusion of the solvent from one layer to the other.

The first process is used in the study of the swelling-induced eversion and flattening of naturally curved gel beams, and in the shaping from sphere-like to nearly developable shapes of rectangular gel plates. In the latter, the final shape depends on several geometrical and mechanical factors. Reinforcing fibers can be crucial in controlling shaping under swelling and greatly influence the characteristics of the final shapes. Swelling is analyzed with a fully coupled nonlinear three-dimensional stress-diffusion model. A revised version of the Flory-Rehner free energy is adopted to model the presence of the fibers.

The second process is carried out experimentally through the fabrication of bilayer sheets with one passive layer of polydimethylsiloxane (PDMS) and one layer of PDMS mixed with silicone oil; the morphing is induced by extracting the oil from the elastomer. The experiment concerns the study of bending of shrinking beams. The problem is

also set within the context of three-dimensional finite elasticity with distortions, considering the total extraction of oil as an isotropic bulk contraction. The latter is also used to investigate the eversion of cylindrical bilayer shells after oil extraction. It is shown how the geometry and the initial fraction of oil affect the shape at equilibrium, which can be in the form of cylindrical shells with axes orthogonal to the original one, saddle-like shapes and doubly curved shapes.
The third and last process is explored starting from the experiment described above, letting the oil initially contained in a single layer diffuse into the layer made of only PDMS, without extracting it. The resulting transient bending is numerically simulated through the stress-diffusion model and a simplified way to predict the steady-state curvature is proposed.
Furthermore, as regards swelling/shrinking of bilayer beams, the problem is also addressed from an energetic point of view, highlighting the importance of the choice of the deformation measures for the formulation of reduced analytical models. In particular, explicit formulas for the curvature and the stretch of the middle axis are provided for naturally curved growing beams.

ACKNOWLEDGEMENTS

First and foremost I would like to express my gratitude to my supervisor Prof. Paola Nardinocchi for her guidance, support and encouragement during the PhD. I am greatly indebted for her patience, inspiration and sharing her knowledge on the mechanics of soft active solids and structures.

I am grateful to Dr Michele Curatolo for computational assistance and for sharing his ideas and opinions during our meetings and lunch breaks.

Many thanks to Dr Valeriy Luchnikov for hosting me at the CNRS research unit Institut de Science des Matériaux de Mulhouse (IS2M) where I had the chance to run my experiments.

I would like to extend my deepest gratitude to my family for their great love and encouragement for everything. Finally, a special thanks goes to my sweetheart Lucia who has always supported me and with whom I have shared every single moment of this experience, including the hard times that the COVID-19 pandemic has brought, making my journey less tiring.

CONTENTS

1 INTRODUCTION: THE MORPHING PROBLEM 1
1.1 Applications . . . 4
1.2 Research theme . . . 7

2 GLOSSARY 9

3 ENERGY CONSIDERATIONS ON GROWING BEAMS 19
3.1 Flat beams . . . 20
3.1.1 Biot energy . . . 20
3.1.2 Green energy . . . 22
3.1.3 Iso-curvature and iso-stretching transformations 24
3.2 Naturally curved beams . . . 26
3.3 Flattening . . . 28

4 ELASTIC AND INELASTIC PROCESSES IN POLYMER GELS 31
4.1 Swelling processes in polymer gels . . . 32
4.2 Finite elasticity with distortions . . . 35
4.3 Computational analysis of growing beams . . . 36
4.4 Eversion and flattening under swelling . . . 36
4.5 From computational analysis to explicit formulas . . . 46
4.6 Eversion and flattening under shrinking . . . 47

5 DYNAMICS OF POLYMER BEAMS DRIVEN BY SOLVENT DIFFUSION 55
5.1 Internal diffusion . . . 56
5.2 Explicit prediction of the steady-state . . . 58

6 NATURALLY FLAT SHEETS: PLATES AND CYLINDERS 61
6.1 Anisotropic swelling . . . 61
6.2 Enforcing shaping of gel sheets by anisotropic swelling 62
6.3 Eversion of polymer cylinders . . . 71

7 CONCLUSION AND FUTURE STUDIES 73

BIBLIOGRAPHY 78

1

INTRODUCTION: THE MORPHING PROBLEM

In solid mechanics, *shape-morphing* means changing smoothly and gradually the shape of a body from one configuration to another. The design of structures with such characteristics is a complex and multidisciplinary task. For this reason, unlike their rigid structure and mechanism counterparts, morphing structures are yet to be fully understood or utilized.
Nature offers a wide range of shape-changing phenomena, particularly in the kingdom of plants, and it is increasingly recognized as sources of inspiration for the development of bioinspired morphing devices [42, 65]. Because of the limited chemical resources and processing conditions, plants have evolved mechanisms that rely on their internal spatial arrangement of the structural elements to achieve shape change upon different types of external stimuli. Motions of plants can be subdivided into nastic and tropistic. In the first case, the deformation processes of the organs always follow the same kinematical patterns, regardless of the direction of the stimulus. On the contrary, in the second case the motion is influenced by the direction of the stimulus, as the sun-tracking of young sunflowers (heliotropism) and the tendency of most plant stems to grow upward (gravitropism) [68] (Figure 1).

Figure 1: Gravitropic response of *Arabidopsis thaliana*. Adapted from [53].

Hydration-triggered shape change in natural systems offers a passive response with only changes in surrounding humidity levels, as happens, for instance, in the locomotion and dispersion mechanism of Equisetum spores (Figure 2-bottom). Each spore consists of four elaters with a bilayer structure, where each layer has a different degree of water absorption. The consequent differential volume change due to humidity variations of one layer with respect to the other is responsible of a change in the curvature of the elaters, and this allows the spores to "walk" and "jump" [52].
A key role in the shape change of some plant tissues is played by stiff cellulose microfibrils within the extracellular matrices, which confers

anisotropic properties to the structure and hampers swelling or shrinking of the surrounding matrix in the direction of the reinforcing fibril. Depending on the architecture of such fibrils, various shape-morphing are enabled in response to humidity variations, such as bending in pinecones (Figure 2-top right) or twisting in orchid tree seedpods (Figure 2-top left) [22].

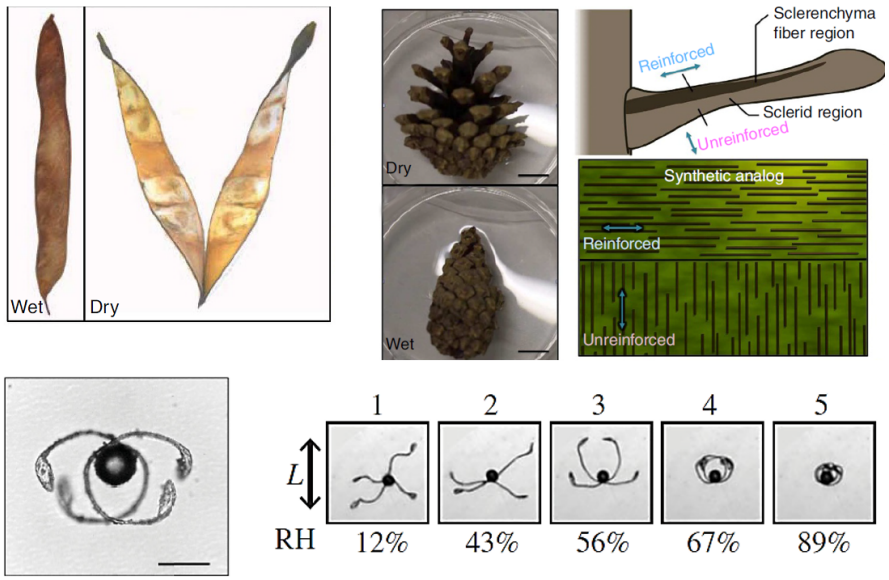

Figure 2: Top left: closed-hydrated and open-dried out orchid tree seedpod. Top right: closed-hydrated and open-dried out conifer pinecone. Adapted from [22]. Bottom: curving of the four elaters of an Equisetum spore as a function of the relative humidity (RH). Adapted from [52]

Swelling-based actuation occurs over a timescale of milliseconds to hours and crosses length scales from stomata on the leaf surface, composed of just two cells, to the entire plant structure [78]. Some plants combine volume-changes with other structural features to achieve faster responses through the sudden release of energy stored in other formats. Some examples include the fracture-based explosive seed dispersal of the filaree [23], the cavitation-induced catapult system of the Sporangium fern to disperse its spores [46], and the fast snap-through transition of the Venus flytrap to capture highly mobile prey [27].
Advances in materials engineering are enabling the design of polymer-based structures subject to large deformations, giving the possibility of making more complex shape changes. A large library of stimuli-responsive soft synthetic materials exists, not to mention the potential active composites that can be obtained by combining together active and non-active materials. It includes three main classes:

- *Polymer gels*, in which the amount of solvent uptake inside the crosslinked network could be changed in response of different

stimuli such as temperature and light, resulting in reversible volumetric expansion or shrinkage.

- *Shape memory polymers (SMP)*, in which a temporary shape can be stored as memory inside the structure by deforming the material at a temperature higher than the glass transition temperature T_g, and then reducing the temperature below T_g. Recovery of the original shape can then be triggered by different stimuli such as high temperature or light.

- *Liquid crystalline elastomers (LCE)*, which combine the properties of liquid crystals with the elastic properties of conventional elastomers. As a result, they show anisotropic properties due to the alignment of those molecules and display highly anisotropic dimensional changes in response to different stimuli such as temperature or humidity.

Controlling the shape-morphing of soft matter without applying external loads is a problem that has aroused the interest of many researchers in recent decades, often taking inspiration from nature [2, 72]. In all this, the material plays a central role in the programming of the final shape: *the material is the machine*, quoting verbatim Bhattacharya et al. [6].
The simplest programmable bodies are beams, namely elastic three-dimensional structures characterized by one length scale much larger than the other two scales. They may develop curvature and torsion induced by non-mechanical actions when points in a cross-section grow axially at different rates. The kingdom of plants is full of biofilament structures which grow in response to environmental stimuli, such as stems [74], tendrils [29] and roots [58]. In the engineering world, the pivotal example of shape-morphing of active beams is the Timoshenko's pioneering work on bimetallic strips that bend due to difference in thermal expansion of the two materials [87].
When initially flat sheets are involved, the deformative process may induce, if appropriately programmed, curving and storage of stretching and bending energies. The programming strategies are based on the generation of through-the-thickness or in-plane stress gradients inside the materials, which can result in bending torques or axial forces, respectively. The first ones induce out-of plane bending, whereas the second out-of-plane buckling. The most common strategies used to induce shape change in initially flat soft active sheets are reviewed in [51] and resumed in Figure 3. Typically, for generating bending moments the approaches consist of using multilayer materials, through-the-thickness material gradients, or through-the-thickness non-homogeneous activation; buckling can be generated using material tessellation, in-plane material gradients, or in-plane non-homogeneous exposure. Moreover, shape changes can be driven by introducing anisotropy of the material, for instance inserting stiffer

fibers. In addition to the material properties, the geometry of the structure, such as the shape of the surface [66], is equally important in governing the final shape, especially when the initial geometry is far to be flat [67].

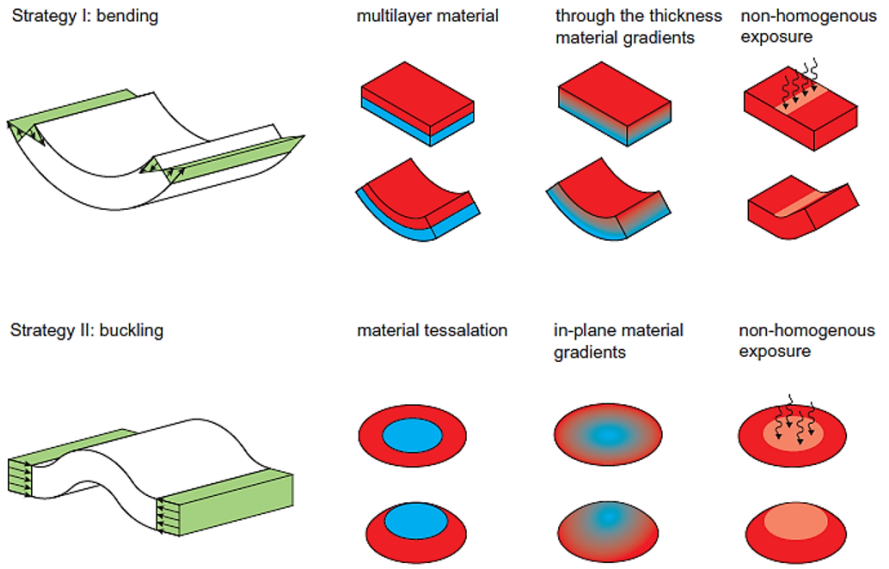

Figure 3: Bending (top) and buckling (bottom) strategies for programming the shape-morphing of initially flat sheets. Adapted from [51]

1.1 APPLICATIONS

The shape-morphing of soft active sheets is applied at different length scales, from micro/nanoelectromechanical systems (MEMS/NEMS) [45] to aerospace applications [44], passing through various fields of application including biotechnology, soft robotics, sensing and actuation, self-folding devices, 3D electronics.
Initially flat structures are the most used both because they provide access to the material surface and because of the simplicity of 2D production techniques, such as 2D photolithography, which allow to program the material in order to achieve a precise 3D transformation. However, the spread of 3D printing as a manufacturing technology has made it possible to facilitate the construction of initially non-flat structures, and the use of active inks has allowed the development of the so-called 4D printing [7, 83], which adds the dimension of transformation over time.
One of the most extensive and promising fields of application is the biomedical field [69]. Self-folding methods are important for drug delivery applications since it is often required to package therapeutic cargo such as small molecules, proteins and living cells. They provide a means to realize 3D, biocompatible, all-polymeric containers with features like porosity, size, shape and surface texture, which are

necessary for accurate control of targeting and release of drugs [24]. Furthermore, the use of polymers that respond to a specific stimulus, such as pH changes, allows for a smart drug delivery, where it is possible to program the folding or unfolding of the structure in a specific location inside the human body. Self-folding devices may be applied also for cell and microorganism encapsulation to create a safe microenvironment for culture [3] (Figure 4-top left).
In tissue engineering applications and regenerative medicine, self-folding methods are used to build precisely patterned scaffolds in anatomically relevant geometries, namely cylinders (vasculature, ducts), spirals (glandular coils, cochlea) and bidirectionally folded sheets (gyri/sulci, villi) [69] (Figure 4-top right). The control of the geometric and mechanical properties of the 3D scaffolds allows to mimic the situation in vivo and to program the growth of cells [35] and the differentiation of stem cells [30].
In microsurgery, self-folding microgrippers are explored as surgical tools for performing biopsies. The folding of mechanism can be triggered by heating or on exposure to a variety of chemicals, while a magnetic guidance allows microgrippers with embedded ferromagnetic layers to be guided in small, twisted passages without the need for a tether [41] (Figure 4-bottom).

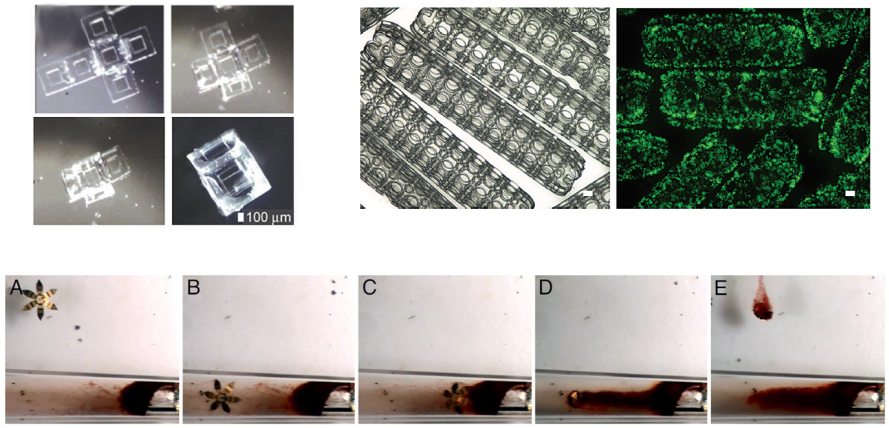

Figure 4: Top left: self-folding of a cubic container for cell encapsulation [3]. Top right: self-folded hydrogel cylindrical scaffolds with micropatterned holes loaded with cells [35]. Bottom: optical microscopy sequence showing capture and retrieval of neutral red-stained cells from a cell culture mass at the end of a tube [41].

Numerous advanced applications in several fields including biotechnology, cell analysis and drug delivery require the use of microtubular structures. Self-rolling of polymers or composite bilayer films due to differential swelling/shrinking is the approach to the formation of such mesoscopic tubes proposed in [21, 50].
Shape-morphing of soft active sheets can be exploited also in many nonmedical applications including sensors/actuators [4, 34] and self-

folding devices.
In the field of electronics, the incorporation of flexible circuits into active soft matrices has allowed the creation of morphing circuits. For example, printed flat substrate and assembled functional electronics on top of it are realized in [88]. The flat structure can then self-morph into a preprogrammed 3D shape when triggered by external heating. In [55] is shown a technique for manufacturing self-folded electrical components, namely stretchable and variable resistors, capacitors, and inductors, suitable as sensors and actuators in flexible circuits. In several engineering fields, features such as stowability, portability, and deployability often drive the project of key products, and origami structures are suitable for this purposes. Such characteristics are fundamental in the aerospace field. Different space-deployable components made of shape memory polymer composites (SMPC), such as SMPC hinges and booms, are reviewed in [44]. Structures based on SMPC components in aerospace include solar arrays and deployable panels, reflector antennas and expandable lunar habitat.
Active origami structures may be used not only for the aforementioned features, but also for their mechanical functional characteristics. Potential applications include metamaterial absorbers [73], deformable energy storage devices [76] and auxetic mechanical metamaterials [71]. Finally, morphing mechanisms for space optimization are also proposed in the food industry. For instance, in [84] a manufacturing process is proposed to create flat pasta that can morphs into a target 3D shape during cooking, and that can be flat-packed to reduce the air space in the packaging (Figure 5).

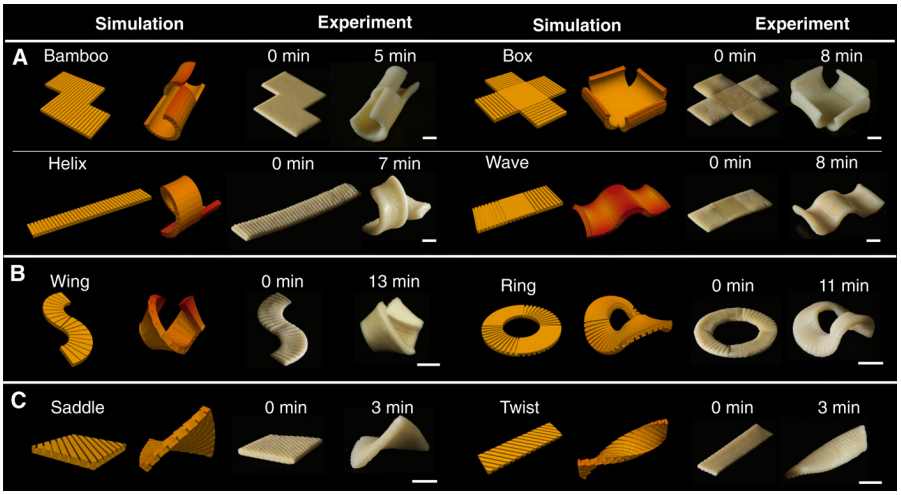

Figure 5: Simulations and experiments of different morphing pasta shapes before and after cooking [84].

This research aims at investigating the shape-morphing of soft active sheets. By "soft active sheets" we mean thin structures made with stimuli-responsive polymeric-based materials that can undergo large displacements in the elastic field during the deformation process in response of stimuli, without the application of external mechanical actions. In particular, the attention is focused on narrow sheets (beams) and naturally flat sheets (plates and cylinders), that is structures with a zero Gaussian middle surface. The programming strategy used is to induce bending via through-the-thickness inhomogeneity of the material, obtained by stacking two homogeneous layers with different properties on top of each other. The materials referred to are gels, so the deformation is induced by swelling or shrinking.
Chapter 2 is dedicated to the literature reviewing through a glossary that identifies the main key words concerning the topics covered in the thesis. Specifically, the differences between elastic and inelastic growth, and between passive, active and swelling fibers are highlighted. In addition, the techniques, both experimental and theoretical, used to induce bending in bilayer gel structures, both in transient and steady state, are explored.
Chapter 3 illustrates the energetic aspects of growing bilayer beams, showing the differences in deriving reduced models by selecting different strain measures. First of all, reduced models of flat bilayer flat beams in plane bending, obtained using the Biot energy or the Green energy, are compared in terms of curvature and stretching formulas. Then, starting from a Biot strain measure, the energy for a bilayer naturally curved beam in plane bending is derived.
Chapter 4 deals with elastic and inelastic processes in polymer gels. They are studied, respectively, within the stress-diffusion continuum model, and within a context of finite elasticity with distortions. The first is applied to the numerical study of the swelling-induced eversion and flattening in naturally curved gel beams, for which explicit formulas for curvature and stretching are derived. The second is used to describe the experiment of the bending of a naturally curved bilayer beam made of PDMS/(PDMS + silicone oil) caused by the extraction of oil. Both studies are conducted in steady-state conditions.
In Chapter 5 the experiment briefly described above is resumed, but this time the curvature of an initially flat beam is induced by the progressive diffusion of the oil from one layer to another. The transient bending is then numerically simulated through the stress-diffusion model and a simplified way to predict the steady-state curvature is proposed.
Chapter 6 deals with the shape-morphing of bilayer naturally flat sheets. The transition from spherical to cylindrical configuration induced by swelling of rectangular bilayer gel plates is numerically inves-

tigated, and the possibility of forcing the shaping through anisotropic swelling is evaluated. Besides, the eversion of shrinking bilayer cylindrical surfaces is explored, studying them numerically in a context of finite elasticity with distortions.
Finally, Chapter 7 summarizes the research outcomes and presents recommendations for future studies.

2

GLOSSARY

A review of the literature is proposed here in the form of a glossary. The main key words concerning the topics covered in the thesis are listed in alphabetical order.

ACTIVE FIBERS

For *active fibers* we mean fibers which can grow inelastically in response to external stimuli. Typically, synthetic active fibers can be divided into two main groups where either volume or molecular order change dominates. The first group includes, for example, fibers subject to thermal expansion or a phase transition such as crystallization. Some materials that fall into the second group are amorphous polymers, shape memory polymers, dielectric elastomers, or liquid crystal elastomers [79]. For example, in [39], multilayer core-shell fibers where a dielectric polymer separates two coaxial electrodes are presented. Following the application of a high voltage to the electrodes, the electrostatic attraction between the conductive layers causes a decrease in diameter and a corresponding elongation of the fiber. In [94], two families of SMP fibers with different glass transition temperatures are embedded within two stacked flat passive layers. After a thermomechanical programming process, the fiber families can be sequentially activated when the temperature is increased, inducing the bending of the sheet.
The effect of active fibers can be also simulated by appropriately orienting the microstructure, as in nematic solids, which have the ability to deform spontaneously and anisotropically in response to temperature change and illumination. Typically, one achieves contraction along and elongation perpendicular to the director on heating or illumination and vice versa on cooling or on recovery in the dark. A wide range of analytical studies on the shape changes of nematic elastomers with patterned director fields is explored by Warner and coworkers [56, 57, 90, 91]. The behavior of a particular class of nematic elastomers, which features large anistropic transformation both due to temperature (reversible) and to solvent evaporation (irreversible), is investigated experimentally in [70] and through numerical and analytical models in [85]. The model is set within the theory of finite elasticity with anisotropic distortions and the transition between spiral ribbons and helicoids of slender bars made of nematic elastomers with through-the-thickness twisting nematic directors is studied.

The solvent-induced changing in volume of gels in response to external stimuli inspired a wide range of theoretical and applied research. The combination of two gel-based layers with different chemical properties into a *bilayer gel* construct is a widely applied way for realizing soft structures able to bend without applying external actions. Many researchers have designed and manufactured devices of this type by combining materials with both different capacities to absorb the solvent, and responsive properties to different stimuli.
A common strategy is to spread a gel layer over a passive polymer layer. Kim et al. [37] synthesize self-bending passive/pH-responsive hydrogel bilayer microstructures via micro-molding, and design a flower-like soft actuator. They also show through numerical simulations and experiments that the final shape is governed by geometrical factors, such as the thickness ratio and the aspect ratio. Finally, they realize a flower-like soft actuator (Figure 6) with controlled numbers of petals and control their motion through the application of an external magnetic field, thanks to magnetic nanoparticles incorporated into the structure.

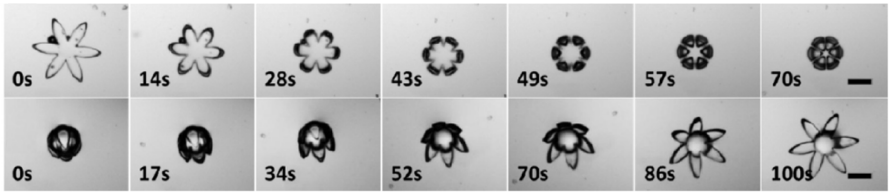

Figure 6: Shape transformation of a flower-shaped via pH variations. Top: bending from planar sheet to 3D at pH 11. Bottom: unbending from 3D to planar sheet at pH 3. Adapted from [37].

Copolymerization between different types of stimuli-responsive monomers is a clever strategy that is sometimes adopted to give the active layer of the bilayer structure multi-responsive properties. For instance, Bassik et al. [5] copolymerize N-isopropylacrylamide (NIPAm) with Acrylic Acid (AAc) or poly-hydroxyl ethyl methacrylate (HEMA) via photocrosslinking to result in a pH- and Ionic Strength (IS)-sensitive hydrogel, and use poly-ethylene oxide diacrylate (PEODA) as passive layer. They experiment the bilayer structures as active hinges in reversible folding rigid panels. Another example is shown by Li et al. [43]. They attach a thermo- and pH-responsive hydrogel-based layer onto a hydrophobic passive layer. In response to temperature and pH variations the active layer is able to swell and shrink, giving the bilayer the ability to bend bidirectionally. The latter property is achieved also by Wang et al. [89] through the implementation of a solvent-responsive actuator consisting of a quasi-passive hydrogel layer and a layer able to swell in deionized water and to shrink in acetone/water solution. They also compare the experimental results with

numerical simulation by modeling the chemically-induced swelling and shrinking as a thermal expansion/contraction.
The fabrication of bilayer gels through the dispersion of the responsiveness to stimuli into two layers rather than one layer extends the adaptability and applicability of such devices. Cheng et al. [11] design a poly(N-isopropylacrylamide) (pNIPAm) and poly(2-(dimethylamino ethyl methacrylate) based bilayer hydrogel which separately serve as temperature and pH-sensitive layers. Considering the bidirectional bending in acid and ethanol media, they use the bilayer hydrogel as a soft switch in a circuit.
Some authors exploit the hydrophilic and hydrophobic behavior of thermo-responsive hydrogels like pNIPAm below and above a volume phase transition temperature (VPTT). Indeed, such hydrogels have the property of swelling below the VPTT and shrinking above the VPTT. For instance, Wei et al. [92] and Zhang et al. [96] use for their experiments bilayers consisting of two thermo-responsive hydrogel-based layers with different VPTT.
Bending of bilayer structures can also be induced using the same type of gel for each layer but with different shear moduli, for example by varying the degree of crosslinking during the fabrication process. In fact, when embedded in a solvent bath, each homogeneous part, if it was free from the rest of the system, would have a swelling ratio at equilibrium strongly dependent on the shear modulus: the higher the elastic modulus of the gel, the less solvent it is able to absorb. This well known property is shown, for example, by Oh et al. [64], which fabricate pH-responsive Janus hydrogel microstrips consisting of two layers with large difference in the elastic moduli.

ELASTIC GROWTH

Gels are elastic solids consisting of long polymer chains joined between them with crosslinks, whose density determine the global mechanical properties. If a dried gel is placed in a solvent bath, it absorbs the solvent and its volume increases. If allowed to swell freely, its state is determined by a trade-off between the chemical energy and the elastic energy. The first due to the solvent permeation, the second due to the elastic deformation of the polymeric lattice [19]. Therefore, since gel bodies store elastic energy during a swelling process, the latter can be viewed as an *elastic growth*.

INELASTIC GROWTH

Unlike the volumetric growth that occurs in gels, thermal expansion in solids does not involve mass exchange. Furthermore, if a homogeneous metal body is uniformly heated and leaved to expand freely, no elastic energy is stored during the volume change. This phenomenon is the

simplest example of *inelastic growth*, which is usually described in solid mechanics as local changes of the zero-stress reference state through the notion of distortion.

PASSIVE FIBERS

Reinforcing active or swellable isotropic sheets with aligned stiffer *passive fibers* gives the structure anisotropic properties, limiting the growth of the matrix along their alignment.
Examples of anisotropic swelling can be found in the kingdom of plants, where the orientation of cellulose fibrils contained in a highly swellable matrix control the shape-morphing of systems like pinecones and seedpods, showing swelling-induced bending and twisting modes, respectively [22].
Inspired by nature, scientists program the morphing of multilayer gel-based sheets suitably orienting the fibers in the different layers.
For instance, the swelling-induced twisting of narrow sheets yielding to helices or ribbons, obtained by orienting the fibers at an angle $\pm\theta$ with respect to the longitudinal axis, is widely studied. Two orthogonally oriented arrays of cotton wires embedded in a thermoresponsive gel matrix are employed by Sharon and coworkers [1] to program such morphing. In [36] temperature-sensitive hydrogel films are sandwiched between stripes of a rigid glassy polymer into a trilayer structure. Seedpod-like architectures with different orientation angle θ are concatenated to form complex multihelical frameworks (Figure 7).

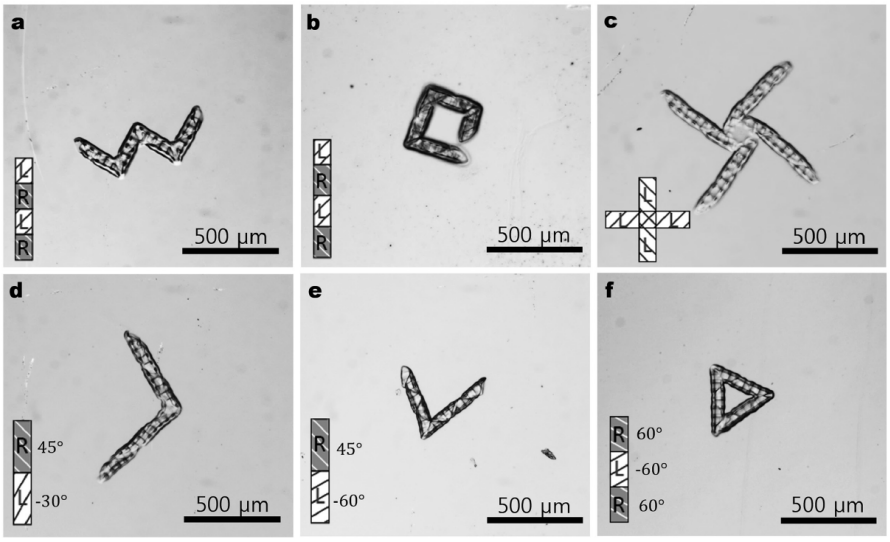

Figure 7: Examples of multihelical structures consisting of n regular seedpod-like architectures. Adapted from [36].

In [59] the anisotropic swelling-induced helicoid-ribbon transition of narrow sheets is described within an extension of the Flory-Rehner thermodynamic model which takes into account the oriented hamper-

ing of the swelling-induced deformations due to the presence of stiffer fibers [60, 63].

SWELLING FIBERS

The incorporation of *swelling fibers* into a soft matrix is another valid technique for the anisotropic actuation of soft composite structures through solvent absorption or release.
In [10] gel-based fibers are 3D printed upon a gel-based substrate, and both are thermo-responsive. Because of the higher density of crosslink, the patterned lines exhibit lower swelling ratio respect to the substrate upon varied temperature, resulting in a through-the-thickness swelling mismatch and out-of-plane morphing controlled by temperature variations.
Hydrogel composite ink embedding stiff cellulose fibrils is used in [83] to print composite hydrogel bilayer textures. During printing, fibrils undergo shear-induced alignment, which leads to anisotropic stiffness and swelling behaviour in the longitudinal direction compared to the transverse direction (Figure 8).

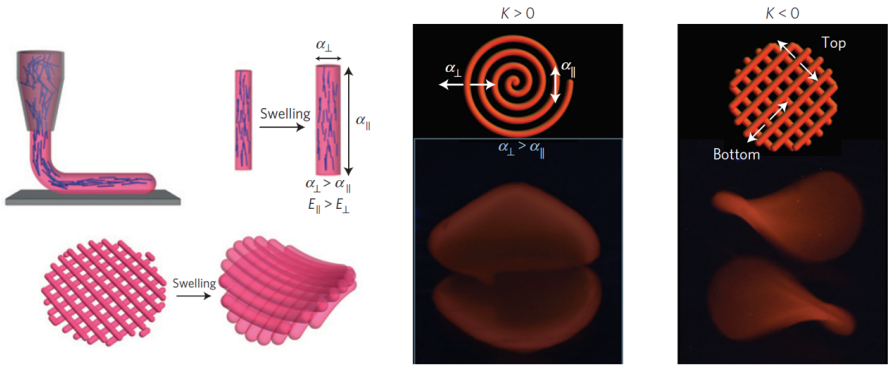

Figure 8: Left: schematic of the shear-induced alignment of cellulose fibrils during ink printing and subsequent effect on anisotropic swelling Right: print pattern and final swollen shape with positive and negative Gaussian curvature. Adapted from [83].

Another manufacturing technique is patterning photo-crosslinkable hydrogel sheets with alternating in-plane parallel stiffer and softer strips, as discussed in [8]. Specifically, they study the dependency of the buckling transition between flat and rolled configuration on the width of the strips, and find that the sheet prefers to swell anisotropically in the plane rather then roll when the strip width falls below a critical size proportional to the sheet thickness.
The photolithographic method is also used in [86] to build planar composite gel sheets with more than one family of parallel strips, each responding to a particular external trigger. For example, as shown in Figure 9, starting from a swollen flat state, the buckling transition

from flat to rolled configuration can be achieved around two axes by orienting a family of swelling fibers and one of shrinking fibers orthogonally to each other, the one responding to pH variations and the others to the addition of NaCl in the solvent bath.
The possibility of obtaining multiple shape transformations of composite hydrogels through swelling/shrinking controlled by multiple stimuli is also described in [98] by embedding printed active- or passive-swelling fibers into active- or passive-swelling matrices, and exploring their combinations.

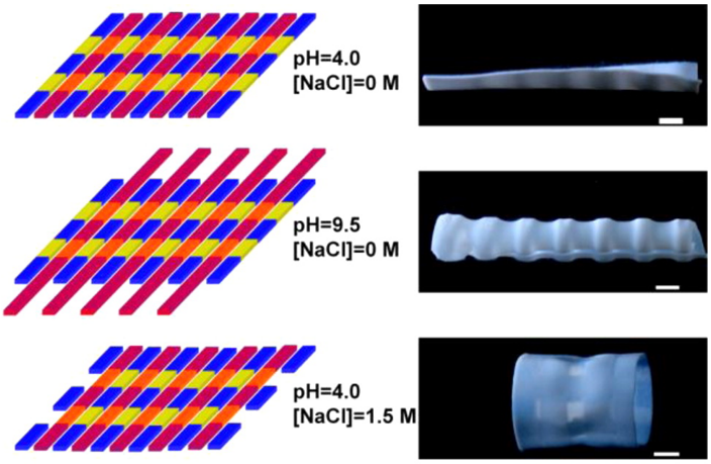

Figure 9: Multiple shape transformations of a rectangular flat gel sheet (top) through the swelling of the red stripes by increasing the pH of the solution (center), or the shrinking of the yellow stripes by increasing the concentration of NaCl in the solution (bottom). Adapted from [86].

TRANSIENT DIFFUSION-INDUCED BENDING

In gel-based materials, the spatial distribution of the solvent within the matrix and the amount of solvent absorbed or released determine the shape and size reached by the body. At equilibrium, in structures presenting inhomogeneities in the material, the spatial distribution of the solvent is inhomogeneous as well. However, even in homogeneous gels non-equilibrium phenomena that take place during the solvent absorption and migration through the network involve the stress state in the gel and a change of shape. For instance, Figure 10 shows a simulation of the swelling process of a homogeneous initially dry gel cube (from left to right). The final steady-state (right) is clearly again a cube and the solvent is evenly distributed. The intermediate state (center), on the other hand, is not homogeneous due to the faster absorption at the edges which gives the boundary a curved shape during the evolution.

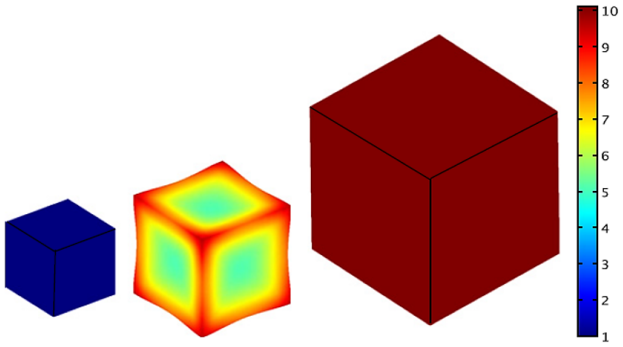

Figure 10: Simulation of the swelling process of a homogeneous initially dry gel cube (from left to right). Color map shows the volume increase. Adapted from [48].

In homogeneous gel sheets, the diffusion of the solvent can generate a through-the-thickness inhomogeneity which produces a transient bending of the structure as a global effect. In [31] the top surface of a crosslinked polydimethylsiloxane (PDMS) beam is swollen by placing a drop of a favorable solvent. As the top of the beam expands the remainder of the beam is required to bend to accommodate this deformation. In this experiment the curving occurs only transiently. Indeed, the beam bends as the fluid permeates through the thickness; at steady-state, when the fluid is homogeneously distributed, the beam relaxes and recovers its original shape.
However, under certain boundary conditions the diffusion can never stop also at steady-state, as shown in [15]. Here, the Authors induce a permanent bending of a homogeneous hydrogel thin structure which is in contact at its top and bottom faces with two environments at different chemical conditions; such differential chemical conditions causes a uniform water flux through the thickness attained at steady-state.
Transient diffusion-induced bending of bilayer sheets is investigated by several researchers as well. Zhao et al. [97] investigate the time response of hydrophilic/hydrophobic water-responsive bilayer structures by using photopolymers, whose rubbery nature, compared with conventional hydrogels, provides higher actuation speed and force. They also develop a simple analytical model to capture the transient deformation of a bilayer flat beam during swelling. Because of the small swelling ratio of the materials adopted, much lower than that of hydrogels, they ignore the coupling between diffusion and deformation and describe the diffusion of water into the hydrophilic layer through the one-dimensional diffusion equation (Fick's second law)

$$\frac{\partial c(z,t)}{\partial t} = D\frac{\partial^2 c(z,t)}{\partial z^2}, \tag{2.0.1}$$

being $c(z,t)$ the mole concentration of water at thickness coordinate z and at time t, and D the diffusion coefficient. The profile of $c(z,t)$

admits an explicit expression once boundary and initial conditions are assigned. A similar approach is also adopted in [95] to describe the diffusion-induced bending of bilayer hydrogen sensors. They then compute the distortion λ_o acting on the swelling layer through the volumetric constraint $\lambda_o = (1 + \Omega c)^{1/3}$, where Ω is the molar volume of water, and calculate the linear elastic strain ε_a by decomposing it additively as $\varepsilon_a = \varepsilon_0 + \kappa z - \ln \lambda_o$, with ε_0 the visible axial strain and κ the visible curvature. For the hydrophobic passive layer the elastic strain is $\varepsilon_p = \varepsilon_0 + \kappa z$. Finally, they find a formula of the bending curvature $\kappa(t)$ by imposing the static equilibrium at all times of total external force and torque on the cross-section.

Due to the slow diffusion of solvent into the polymer network, the deformation speed of gel-based sheets is limited. During the diffusion process, the onset of phenomena like cavitation [46] or mechanical instabilities [40] can quickly morph such soft structures. Stoychev et al. [80, 81] investigated the actuation of patterned bilayer films consisting of an hydrophobic (passive) layer and a thermoresponsive hydrophilic (active) layer. The bilayer is undeformed at temperature $T > 70$ °C and folding occurs after cooling below 70 °C. It is not homogeneously activated, but edge-activated so that the active layer progressively swells as water diffuses from the lateral sides, triggering the rolling of the periphery of the film, which in turn changes its macrosopic mechanical properties. As the water penetrates towards the center of the film, swelling causes more stress which then becomes large enough to overcome the energetic barrier, thus allowing for a very fast switching of shape (see Figure 11).

Fast and repetitive shaping can also overcome by designing devices that exploit processes of transient shrinking. Kim et al. [38] fabricate a poly(dimethylsiloxane) (PDMS) thin strip and select n-hexane as solvent because of its affinity with PDMS, its fast diffusion kinetics and its fast evaporation. As shown in the scheme of Figure 12 (left), they take a clamped-clamped swollen strip and impose an initial lateral confinement d_0, which induces an initial buckling of the beam. Once local buckling occurrs, on the concave and convex faces of the ribbon the surface area decreases and increases, respectively. They observe that such asymmetric change in surface area results in a differential evaporation speed of solvent between the two faces, that causes a shrinking of the convex face faster than the concave face until the critical threshold for snap-buckling is reached. The new local curvature obtained alters the local shrinking dynamics and can trigger a new snap-buckling of the beam, and so on. This process generates multiple snap-through transitions without the need for additional solvent (see Figure 12 (right)).

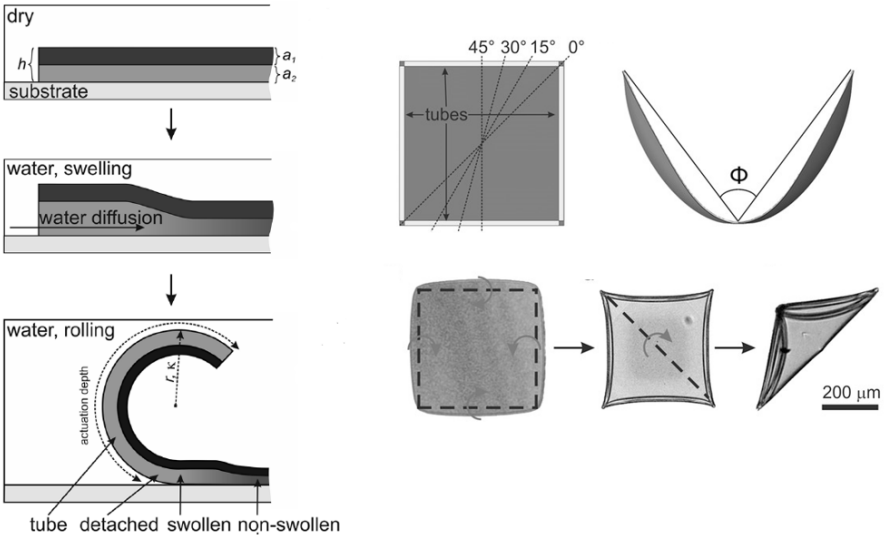

Figure 11: Left: scheme of the bending of the edge of a polymer bilayer. Right: experimentally observed folding of a square polymer bilayer. Arrows and dashed lines indicate the folding direction. Adapted from [80].

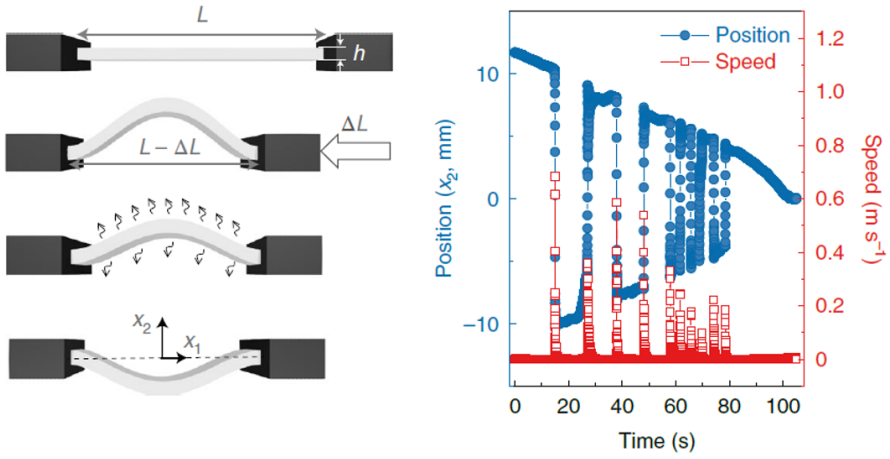

Figure 12: Left: schematic of the process for generating multiple snap transitions through an assigned initial lateral confinement of the beam. Right: vertical displacement and speed of middle point of the beam. Adapted from [38].

3

ENERGY CONSIDERATIONS ON GROWING BEAMS

In elasticity theory the choice of a strain measure is arbitrary. Any symmetric tensor $\mathbf{E} = f(\mathbf{U})$ that is in one-to-one correspondence with the right stretch tensor $\mathbf{U} = \mathbf{Q}^{-1}\mathbf{F}$, where $\mathbf{Q}$ is a rotation tensor, $\mathbf{F}$ is the deformation gradient, and holds $f(\mathbf{o}) = \mathbf{o}$, can be used as a strain measure [18]. The selection is influenced by the convenience in correlation with experimental observations on a particular material or the simplicity of the mathematical formulation. Some examples of usual definitions are

$$\begin{aligned} &\mathbf{E}_B = \mathbf{U} - \mathbf{I}\,, \quad \mathbf{E}_G = \frac{1}{2}(\mathbf{C} - \mathbf{I})\,, \\ &\mathbf{E}_A = \frac{1}{2}(\mathbf{I} - \mathbf{B}^{-1})\,, \quad \mathbf{E}_S = \mathbf{I} - \mathbf{V}^{-1}\,, \end{aligned} \tag{3.0.2}$$

which are commonly called *Biot*, *Green*, *Almansi* and *Swainger* strain tensor, respectively, where $\mathbf{C} = \mathbf{F}^T\mathbf{F}$ and $\mathbf{B} = \mathbf{F}\mathbf{F}^T$ are the left and right Cauchy-Green deformation tensors, and $\mathbf{V} = \mathbf{F}\mathbf{Q}^{-1}$ is the left stretch tensor.

Many soft matter researchers in the last few years have focused their studies on the non-Euclidean plate theory introduced by Efrati and co-workers [20], that is based on an elastic energy quadratic in invariants of Green strain. However, as evidenced by Wood and Hanna in [93], the choice of the strain measure with which an elastic energy is built is not trivial, and they demonstrate this with a simple example. They take a thin elastic plate, bend it into a cylindrical ring and fuse the ends. They observe that getting a positive stretch of the midplane involves dramatically different energy storage, if the energy involved in such process is estimated with different strain measures: the Almansi and Swainger models predict a decrease in bending energy, the Green model predicts an increase in bending energy, while, according to the Biot model, it is pure stretching since the bending energy does not change. The issue is more and more relevant when growth processes are involved and visible and elastic strain measures must be chosen.

In this section a comparison between the energies deriving from the use of two strain measures, Biot and Green, is shown. For this purpose, a simplified model of flat bilayer beam in plane bending regime is considered as an example. In this restricted situation the three-dimensional deformation tensor is reduced to its relevant component, corresponding to the axial direction of the beam.

Given the orthonormal basis $(\mathbf{e}_1, \mathbf{e}_2, \mathbf{e}_3)$ and the coordinate system (x, y, z), consider a flat beam with uniform thickness h and width w (Figure 13). It is composed of two stacked layers with equal thickness $h/2$ and Young moduli E_b and E_t, denoting, from now on, with b the bottom layer and with t the top layer.

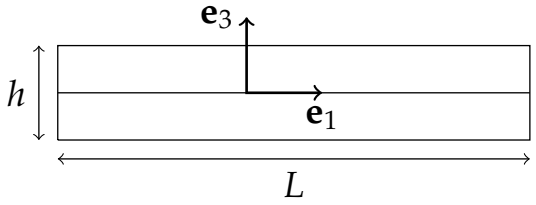

Figure 13: Reference configuration of the bilayer beam.

The beam suffers an incompatible three-dimensional distortion. Specifically, the bottom and top layers would freely, spherically and inelastically deform of an amount λ_{ob} and λ_{ot}, respectively, if they were not glued together. The visible longitudinal deformation λ can be multiplicatively decomposes into elastic and inelastic deformations, such that

$$\lambda = \lambda_{eb}\lambda_{ob} = \lambda_{et}\lambda_{ot}\,, \tag{3.1.3}$$

where λ_{eb} and λ_{et} represent the elastic deformations of the two layers. It is assumed isotropic stretch at x determined by $\Lambda_0(x)$. When there is plane bending and the cross sections remain flat and orthogonal to the beam axis, the visible longitudinal deformation may be expressed linearly in the thickness coordinate z as

$$\lambda(x, z) = \Lambda_0(x) + z\Lambda_1(x)\,, \tag{3.1.4}$$

where, from now on, Λ_0 and Λ_1 are assumed uniform. Inspired by the argument proposed in [93], two reduced two-dimensional, isotropic and quadratic energies are built in the following subsections starting from two different visible strain measures:

$$\text{Biot} \quad \delta = \lambda - 1\,, \tag{3.1.5}$$

$$\text{Green} \quad \delta = \frac{1}{2}(\lambda^2 - 1)\,. \tag{3.1.6}$$

3.1.1 *Biot energy*

The Biot elastic strain measure for each layer is:

$$\delta_{eb} = \lambda_{eb} - 1\,, \quad \text{and} \quad \delta_{et} = \lambda_{et} - 1\,, \tag{3.1.7}$$

From (3.1.7),(3.1.3) and (3.1.4), the Biot elastic energy per unit reference length may be written as

$$\begin{aligned}
\mathcal{U}^B =& \frac{1}{2} w E_b \lambda_{ob}^3 \int_{-\frac{h}{2}}^{0} \delta_{eb}^2 dz + \frac{1}{2} w E_t \lambda_{ot}^3 \int_{0}^{\frac{h}{2}} \delta_{et}^2 dz = \\
=& \frac{1}{2} w E_b \lambda_{ob}^3 \int_{-\frac{h}{2}}^{0} \left(\frac{\lambda}{\lambda_{ob}} - 1 \right)^2 dz + \frac{1}{2} w E_t \lambda_{ot}^3 \int_{0}^{\frac{h}{2}} \left(\frac{\lambda}{\lambda_{ot}} - 1 \right)^2 dz = \\
=& \frac{1}{2} w E_b \lambda_{ob}^3 \int_{-\frac{h}{2}}^{0} \left(\left(\frac{\Lambda_0}{\lambda_{ob}} - 1 \right)^2 + 2z \frac{\Lambda_1}{\lambda_{ob}} \left(\frac{\Lambda_0}{\lambda_{ob}} - 1 \right) + z^2 \left(\frac{\Lambda_1}{\lambda_{ob}} \right)^2 \right) dz + \\
&+ \frac{1}{2} w E_t \lambda_{ot}^3 \int_{0}^{\frac{h}{2}} \left(\left(\frac{\Lambda_0}{\lambda_{ot}} - 1 \right)^2 + 2z \frac{\Lambda_1}{\lambda_{ot}} \left(\frac{\Lambda_0}{\lambda_{ot}} - 1 \right) + z^2 \left(\frac{\Lambda_1}{\lambda_{ot}} \right)^2 \right) dz = \\
=& \frac{1}{4} w h \left[E_b \lambda_{ob}^3 \varepsilon_{eb}^2 + E_t \lambda_{ot}^3 \varepsilon_{et}^2 \right] + \frac{1}{8} w h^2 \left[E_t \lambda_{ot}^3 \varepsilon_{et} k_{et} - E_b \lambda_{ob}^3 \varepsilon_{eb} k_{eb} \right] + \\
&+ \frac{1}{48} w h^3 \left[E_b \lambda_{ob}^3 k_{eb}^2 + E_t \lambda_{ot}^3 k_{et}^2 \right] , \qquad (3.1.8)
\end{aligned}$$

where the Biot elastic mid-line strain measures ε_{eb} and ε_{et}, and elastic bending measures k_{eb} and k_{et} for each layer are introduced and defined as

$$\varepsilon_{em} = \frac{\Lambda_0}{\lambda_{om}} - 1 \quad \text{and} \quad k_{em} = \frac{\Lambda_1}{\lambda_{om}} , \quad m = b, t . \qquad (3.1.9)$$

The integral is computed on the current volume. The elementary actual volume is $dv = \lambda_{om}^3 dV$ $(m = b, t)$, being $dV = dl\, dw\, dz$ the elementary reference volume. The Biot energy density is exactly at quadratic order in the elastic measures. Alternatively, defining a visible mid-line strain ε and a visible bending measure k as

$$\varepsilon = \Lambda_0 - 1 \quad \text{and} \quad k = \Lambda_1 , \qquad (3.1.10)$$

the equations (3.1.9) become

$$\begin{aligned}
\varepsilon_{em} &= \frac{1}{\lambda_{om}} (\varepsilon - \varepsilon_{om}) , \quad \text{with} \quad \varepsilon_{om} = \lambda_{om} - 1 , \quad m = b, t , \\
k_{em} &= \frac{k}{\lambda_{om}} , \qquad (3.1.11)
\end{aligned}$$

and the energy density $\mathcal{U}^B$ can be expressed as a function of ε and k:

$$\begin{aligned}
\mathcal{U}^B = \hat{\mathcal{U}}^B(\varepsilon, k) =& \frac{1}{4} w h \left(E_b \lambda_{ob} (\varepsilon - \varepsilon_{ob})^2 + E_t \lambda_{ot} (\varepsilon - \varepsilon_{ot})^2 \right) + \\
&+ \frac{1}{8} w h^2 \left(E_t \lambda_{ot} (\varepsilon - \varepsilon_{ot}) - E_b \lambda_{ob} (\varepsilon - \varepsilon_{ob}) \right) k + \\
&+ \frac{1}{48} w h^3 \left(E_b \lambda_{ob} + E_t \lambda_{ot} \right) k^2 , \qquad (3.1.12)
\end{aligned}$$

The unknowns of the problem ε and k result from the minimization

$$\dot{\mathcal{U}}(\varepsilon, k) = \frac{\partial \mathcal{U}}{\partial \varepsilon} \dot{\varepsilon} + \frac{\partial \mathcal{U}}{\partial k} \dot{k} = 0 , \qquad (3.1.13)$$

which leads to the system of linear equations

$$\frac{\partial \mathcal{U}}{\partial \varepsilon} = 0\,, \quad \frac{\partial \mathcal{U}}{\partial k} = 0\,. \tag{3.1.14}$$

The system of equations (3.1.14) can be written explicitly for Biot when $\mathcal{U} = \mathcal{U}^B$:

$$\begin{cases} 4(\alpha\lambda_{ot} + \lambda_{ob})\varepsilon + h(\alpha\lambda_{ot} - \lambda_{ob})k = 4(\alpha\lambda_{ot}\varepsilon_{ot} + \lambda_{ob}\varepsilon_{ob}) \\ 3(\alpha\lambda_{ot} - \lambda_{ob})\varepsilon + h(\alpha\lambda_{ot} + \lambda_{ob})k = 3(\alpha\lambda_{ot}\varepsilon_{ot} - \lambda_{ob}\varepsilon_{ob}) \end{cases}, \tag{3.1.15}$$

where $\alpha = E_t/E_b$, and whose general solutions can be found as

$$\varepsilon = \hat{\varepsilon}(\alpha, \lambda_{ob}, \lambda_{ot}) \quad \text{and} \quad k = \hat{k}(\alpha, h, \lambda_{ob}, \lambda_{ot})\,. \tag{3.1.16}$$

Otherwise, introducing the curvature of the deformed mid-line $\kappa = \Lambda_1/\Lambda_0^2$, and being $\Gamma = \lambda_{ob}/\lambda_{ot}$, the solutions of the minimization problem can be expressed in geometric terms:

$$\Lambda_0 = f(\alpha, \Gamma)\lambda_{ob} \quad \text{and} \quad \kappa = g(\alpha, \Gamma)\frac{1}{\lambda_{ob}h}\,, \tag{3.1.17}$$

which derive from the relations (3.1.10):

$$\Lambda_0 = \varepsilon + 1 \quad \text{and} \quad \kappa = \frac{k}{\Lambda_0^2}\,, \tag{3.1.18}$$

and using the solutions (3.1.16).
Formulas (3.1.17) can also be obtained directly as solutions of the system of equations

$$\frac{\partial \mathcal{U}}{\partial \Lambda_0} = 0\,, \quad \frac{\partial \mathcal{U}}{\partial \kappa} = 0\,, \tag{3.1.19}$$

when $\mathcal{U} = \mathcal{U}^B$. In fact, by making the energy variations with respect to Λ_0 and κ for Biot:

$$\begin{aligned} \dot{\mathcal{U}}^B(\Lambda_0, \kappa) &= \frac{\partial \mathcal{U}^B}{\partial \Lambda_0}\dot{\Lambda}_0 + \frac{\partial \mathcal{U}^B}{\partial \kappa}\dot{\kappa} = \\ &= \left(\frac{\partial \mathcal{U}^B}{\partial \varepsilon} + \frac{2k}{(\varepsilon+1)}\frac{\partial \mathcal{U}^B}{\partial k}\right)\dot{\Lambda}_0 + \left((\varepsilon+1)^2\frac{\partial \mathcal{U}^B}{\partial k}\right)\dot{\kappa}\,, \end{aligned} \tag{3.1.20}$$

it can be shown that the systems of equations (3.1.14) and (3.1.19), with $\mathcal{U} = \mathcal{U}^B$, are equivalent.

3.1.2 *Green energy*

The Green elastic strain measure for each layer is:

$$\delta_{eb} = \frac{1}{2}(\lambda_{eb}^2 - 1)\,, \quad \text{and} \quad \delta_{et} = \frac{1}{2}(\lambda_{et}^2 - 1)\,. \tag{3.1.21}$$

Using the equations (3.1.21), (3.1.3) and (3.1.4), the Green energy density reads

$$\begin{aligned}
\mathcal{U}^G =& \frac{1}{2} w E_b \lambda_{ob}^3 \int_{-\frac{h}{2}}^{0} \delta_{eb}^2 dz + \frac{1}{2} w E_t \lambda_{ot}^3 \int_{0}^{\frac{h}{2}} \delta_{et}^2 dz = \\
=& \frac{1}{2} w E_b \lambda_{ob}^3 \int_{-\frac{h}{2}}^{0} \left(\frac{1}{2} \left(\frac{\lambda^2}{\lambda_{ob}^2} - 1 \right) \right)^2 dz + \\
&+ \frac{1}{2} w E_t \lambda_{ot}^3 \int_{0}^{\frac{h}{2}} \left(\frac{1}{2} \left(\frac{\lambda^2}{\lambda_{ot}^2} - 1 \right) \right)^2 dz = \\
=& \frac{1}{2} w E_b \lambda_{ob}^3 \int_{-\frac{h}{2}}^{0} (\varepsilon_{eb}^2 + 2z\varepsilon_{eb} k_{eb} + z^2 k_{eb}^2) dz \; + \; o(\varepsilon_{eb}^2, k_{eb}^2, \varepsilon_{eb} k_{eb}) + \\
&+ \frac{1}{2} w E_t \lambda_{ot}^3 \int_{0}^{\frac{h}{2}} (\varepsilon_{et}^2 + 2z\varepsilon_{et} k_{et} + z^2 k_{et}^2) dz \; + \; o(\varepsilon_{et}^2, k_{et}^2, \varepsilon_{et} k_{et}) \simeq \\
\simeq& \frac{1}{4} wh \left[E_b \lambda_{ob}^3 \varepsilon_{eb}^2 + E_t \lambda_{ot}^3 \varepsilon_{et}^2 \right] + \frac{1}{8} wh^2 \left[E_t \lambda_{ot}^3 \varepsilon_{et} k_{et} - E_b \lambda_{ob}^3 \varepsilon_{eb} k_{eb} \right] + \\
&+ \frac{1}{48} wh^3 \left[E_b \lambda_{ob}^3 k_{eb}^2 + E_t \lambda_{ot}^3 k_{et}^2 \right] , \qquad (3.1.22)
\end{aligned}$$

that is derived through an expansion to quadratic order in the Green elastic mid-line strain measures ε_{eb} and ε_{et}, and the elastic bending measures k_{eb} and k_{et}, defined as

$$\varepsilon_{em} = \frac{1}{2} \left(\frac{\Lambda_0^2}{\lambda_{om}^2} - 1 \right) \quad \text{and} \quad k_{em} = \frac{\Lambda_0 \Lambda_1}{\lambda_{om}^2} , \quad m = b, t , \qquad (3.1.23)$$

and dropping any pure or mixed terms of higher order. Alternatively, defining a visible mid-line strain ε and a visible bending measure k as

$$\varepsilon = \frac{1}{2} (\Lambda_0^2 - 1) \quad \text{and} \quad k = \Lambda_0 \Lambda_1 , \qquad (3.1.24)$$

the equations (3.1.23) become

$$\begin{aligned}
&\varepsilon_{em} = \frac{1}{\lambda_{om}^2} (\varepsilon - \varepsilon_{om}) , \quad \text{with} \quad \varepsilon_{om} = \frac{1}{2} (\lambda_{om}^2 - 1) , \quad m = b, t , \\
&k_{em} = \frac{k}{\lambda_{om}^2} , \qquad (3.1.25)
\end{aligned}$$

and the energy density $\mathcal{U}^G$ can be expressed as a function of ε and k:

$$\begin{aligned}
\mathcal{U}^G = \hat{\mathcal{U}}^G(\varepsilon, k) \simeq& \frac{1}{4} wh \left(\frac{E_b}{\lambda_{ob}} (\varepsilon - \varepsilon_{ob})^2 + \frac{E_t}{\lambda_{ot}} (\varepsilon - \varepsilon_{ot})^2 \right) + \\
&+ \frac{1}{8} wh^2 \left(\frac{E_t}{\lambda_{ot}} (\varepsilon - \varepsilon_{ot}) - \frac{E_b}{\lambda_{ob}} (\varepsilon - \varepsilon_{ob}) \right) k + \\
&+ \frac{1}{48} wh^3 \left(\frac{E_b}{\lambda_{ob}} + \frac{E_t}{\lambda_{ot}} \right) k^2 . \qquad (3.1.26)
\end{aligned}$$

The unknowns of the problem ε and k result from the minimization (3.1.13) that leads to the system of linear equations (3.1.14), which can be written explicitly when $\mathcal{U} = \mathcal{U}^G$:

$$\begin{cases} 4(\alpha\lambda_{ob} + \lambda_{ot})\varepsilon + h(\alpha\lambda_{ob} - \lambda_{ot})k = 4(\alpha\lambda_{ob}\varepsilon_{ot} + \lambda_{ot}\varepsilon_{ob}) \\ 3(\alpha\lambda_{ob} - \lambda_{ot})\varepsilon + h(\alpha\lambda_{ob} + \lambda_{ot})k = 3(\alpha\lambda_{ob}\varepsilon_{ot} - \lambda_{ot}\varepsilon_{ob}) \end{cases}, \tag{3.1.27}$$

whose general solutions are like equations (3.1.16), or they can be expressed in geometric terms like equations (3.1.17) by inverting the relations (3.1.24):

$$\Lambda_0 = (2\varepsilon + 1)^{\frac{1}{2}} \quad \text{and} \quad \kappa = \frac{k}{\Lambda_0^3}, \tag{3.1.28}$$

and using the solutions (3.1.16).
As for Biot, formulas (3.1.17) can also be obtained directly as solutions of the system of equations (3.1.19), setting $\mathcal{U} = \mathcal{U}^G$. In fact, by making the energy variations with respect to Λ_0 and κ:

$$\begin{aligned} \dot{\mathcal{U}}^G(\Lambda_0, \kappa) &= \frac{\partial \mathcal{U}^G}{\partial \Lambda_0}\dot{\Lambda}_0 + \frac{\partial \mathcal{U}^G}{\partial \kappa}\dot{\kappa} = \\ &= \left((2\varepsilon + 1)^{\frac{1}{2}} \frac{\partial \mathcal{U}^G}{\partial \varepsilon} + \frac{3k}{(2\varepsilon + 1)^{\frac{1}{2}}} \frac{\partial \mathcal{U}^G}{\partial k} \right) \dot{\Lambda}_0 + \left((2\varepsilon + 1)^{\frac{3}{2}} \frac{\partial \mathcal{U}^G}{\partial k} \right) \dot{\kappa}, \end{aligned} \tag{3.1.29}$$

it can be shown that the systems of equations (3.1.14) and (3.1.19), with $\mathcal{U} = \mathcal{U}^G$, are equivalent.

3.1.3 *Iso-curvature and iso-stretching transformations*

In order to compare different energy models, in [93] the following example is proposed: a monolayer passive beam of length L is bent into a circular arc with a fixed radius, and one wonders how the different energy models adopted behave when the elongation of this arc varies. Here, one want to reproduce the example in the context of active blilayer beams in absence of external loads. On the basis of the model presented in this section, a curvature κ and a mid-axis stretch Λ_0 cannot be freely assigned regardless of the distortions λ_{ob} and λ_{ot}, which cause the bending and elongation of the beam. Therefore, once the thickness h and the ratio between the Young's moduli α have been fixed, the problem consists in finding the pairs $(\lambda^\star_{ob}, \lambda^\star_{ot})$ that generate an assigned curvature $\kappa = \bar{\kappa}$ for any stretch Λ_0. On the other hand, a similar problem consists in finding the pairs $(\lambda^\star_{ob}, \lambda^\star_{ot})$ that identify an assigned stretch $\Lambda_0 = \bar{\Lambda}_0$ for any curvature κ.
For each pair $(\lambda_{ob}, \lambda_{ot})$, a pair (κ, Λ_0) can be calculated using the respective formulas for the Biot and Green models (equations (3.1.17)).

The morphological diagrams in Figure 14 show, for Biot (left diagram) and Green (right diagram), the configurations reached by a flat beam as a function of λ_{ob} and λ_{ot} ranging between 0.5 and 5, setting $h = 4$ mm and $\alpha = 1$ (same Young modulus for the two layers).

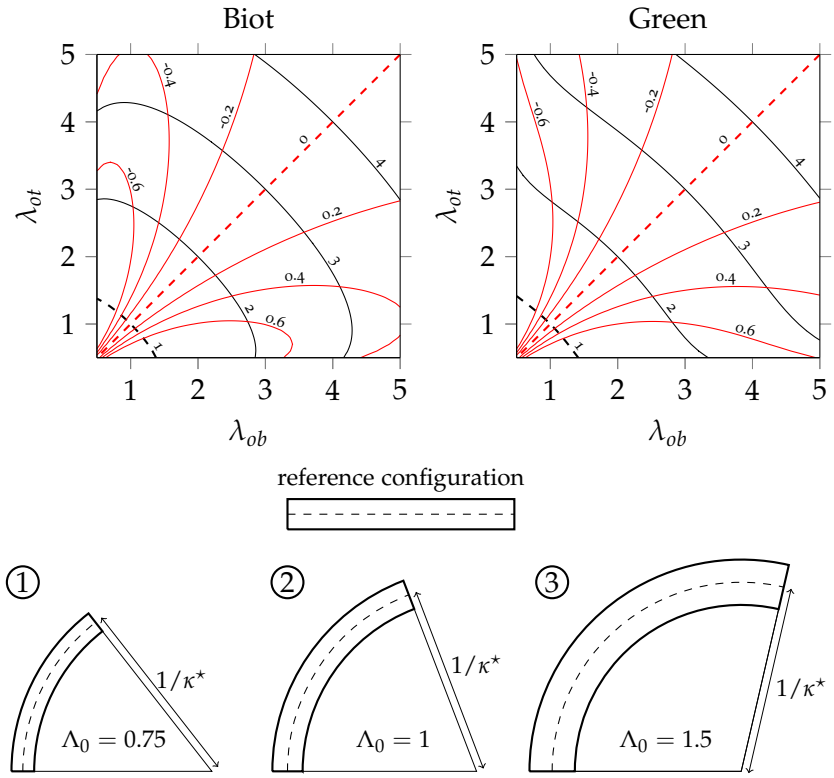

Figure 14: Morphological phase diagrams representing the configurations of a beam according to the Biot (top left) and Green (top right) models, for λ_{ob} and λ_{ot} ranging from 0.5 to 5. It is set $h = 4$ mm and $\alpha = 1$. Black and red lines are iso-Λ_0 and iso-κ lines, respectively. The black and red dashed lines correspond to $\Lambda_0 = 1$ (unstretched configuration) and $\kappa = 0$ (flat configuration), respectively. The cartoons (bottom) represent three configurations of the beam with constant curvature $\kappa = 50$ m^{-1} corresponding to the labels 1 ($\Lambda_0 = 0.75$), 2 ($\Lambda_0 = 1$), and 3 ($\Lambda_0 = 1.5$). The values on the iso-κ lines indicate the dimensionless curvature κh

The black solid lines are isolines of the realized stretch Λ_0 (iso-Λ_0) when $\Lambda_0 \neq 1$. The black dashed lines correspond to the isolines $\Lambda_0 = 1$, that is when the beam bends without stretching the mid-axis, and divide the diagrams into region with $\Lambda_0 < 1$ (shortening of the mid-axis) and a region with $\Lambda_0 > 1$ (elongation of the mid-axis). The red solid lines are isolines of the realized curvature (iso-κ) when $\kappa \neq 0$. The red dashed lines correspond to the isoline $\kappa = 0$ ($\lambda_{ob} = \lambda_{ot}$), that is when the beam grows without bending, and divide the diagrams into two regions with $\kappa > 0$ and $\kappa < 0$. Having set the same elastic modulus for the two layers, they are also line of symmetry for the diagrams.

Moving on an iso-κ line, it crosses the iso-Λ_0 lines identifying configurations of the beam with constant curvature and different stretch, as the three cartoons at the bottom of Figure (14) show. They correspond to beams with $\kappa = \bar{\kappa} = 50\ \mathrm{m}^{-1}$ and stretch values $\Lambda_0 = 0.75$ (1), $\Lambda_0 = 1$ (2) and $\Lambda_0 = 1.5$ (3). They also highlight that, as the beam undergoes isotropic stretch, there is simultaneously an elongation(shortening) of the mid-axis and a thickening(thinning) of the thickness. Likewise, moving on an iso-Λ_0 line, it crosses the iso-κ lines identifying configurations of the beam with different curvatures at constant stretch.
These graphs highlight an important aspect between the two models. When both the values of λ_{ob} and λ_{ot} are limited to around 1, i.e. when the distortions are small, the isolines are practically superimposable. However, as the distortions grow, and more evidently, as the mismatch $|\lambda_{ob} - \lambda_{ot}|$ between them grows, the two models diverge. This implies that each model realizes a certain configuration of the beam, identified by a pair $(\Lambda_0^\star, \kappa^\star)$, but with different pairs $(\lambda_{ob}^\star, \lambda_{ot}^\star)$ in Biot and Green.

3.2 NATURALLY CURVED BEAMS

Consider now a naturally curved bilayer beam with uniform curvature κ_d, thickness h and width w, composed of two stacked layers with thickness $h_i = \beta h$ and $h_e = (1-\beta)h$, being $\beta \in (0,1)$, and Young moduli E_i and E_e, denoting, from now on, with e the outer layer (extrados) and with i the inner layer (intrados). In III, the explicit formulas for the mid-axis stretch and curvature come from a constitutive prescription based on the Biot strain measure

$$\delta = \lambda - 1\,, \tag{3.2.30}$$

with the visible hoop deformation λ defined by

$$\lambda(\zeta) = (1+\kappa_d\zeta)^{-1}(\Lambda_0 + \zeta\Lambda_1)\,, \qquad \Lambda_1 = \kappa\Lambda_0^2\,, \tag{3.2.31}$$

being ζ the radial coordinate, Λ_0 the visible axis stretch and κ the curvature. As it is done in Section 3.1 for straight beams, also for naturally curved beams the elastic strain measures for the inner and outer layer can be defined as

$$\delta_{ee} = \frac{\lambda}{\lambda_{oe}} - 1 \quad \text{and} \quad \delta_{ei} = \frac{\lambda}{\lambda_{oi}} - 1\,, \tag{3.2.32}$$

and a Biot elastic energy per unit reference length can be written as[1]:

$$\begin{aligned}\mathcal{U}^B =&\frac{1}{2}wE_e\lambda_{oe}^3\int_{-\frac{h}{2}}^{-\frac{h}{2}+\beta h}\delta_{ee}^2(1+\kappa_d\zeta)d\zeta+\\&+\frac{1}{2}wE_i\lambda_{oi}^3\int_{-\frac{h}{2}+\beta h}^{\frac{h}{2}}\delta_{ei}^2(1+\kappa_d\zeta)d\zeta=\\=&\frac{1}{2}wE_e\lambda_{oe}^3\int_{-\frac{h}{2}}^{-\frac{h}{2}+\beta h}\left(\frac{\lambda}{\lambda_{oe}}-1\right)^2(1+\kappa_d\zeta)d\zeta+\\&+\frac{1}{2}wE_i\lambda_{oi}^3\int_{-\frac{h}{2}+\beta h}^{\frac{h}{2}}\left(\frac{\lambda}{\lambda_{oi}}-1\right)^2(1+\kappa_d\zeta)d\zeta\,.\end{aligned}\tag{3.2.33}$$

As an alternative to the balance of force and torque on the cross-section (4.5.60) and (4.5.61), the couple (Λ_0,Λ_1) (formulas III-A.2 and III-A.3) can be obtained as solution of the minimization of the elastic energy:

$$\frac{\partial\mathcal{U}^B}{\partial\Lambda_0}=0\,,\quad\frac{\partial\mathcal{U}^B}{\partial\Lambda_1}=0\,,\tag{3.2.34}$$

and the beam axis curvature evaluated as $\kappa=\Lambda_1/\Lambda_0^2$. Since $\lambda(\zeta)$ is nonlinear in the radial coordinate ζ, terms of order h, h^2 and h^3 do not appear in the equation of the elastic energy (3.2.33). Setting $\beta=1/2$, the asymptotic expansion of the elastic energy up to $\mathcal{O}(h^3)$ leads to a simplified equation

$$\begin{aligned}\mathcal{U}^B\simeq&\frac{1}{4}wh\left(E_i\lambda_{oi}(\Lambda_0-\lambda_{oi})^2+E_e\lambda_{oe}(\Lambda_0-\lambda_{oe})^2\right)\\&+\frac{1}{16}wh^2(E_i\lambda_{oi}(\Lambda_0-\lambda_{oi})(2\Lambda_1-\kappa_d(\Lambda_0+\lambda_{oi}))-\\&-E_e\lambda_{oe}(\Lambda_0-\lambda_{oe})(2\Lambda_1-\kappa_d(\Lambda_0+\lambda_{oe})))+\\&+\frac{1}{48}wh^3(E_i\lambda_{oi}+E_e\lambda_{oe})(\Lambda_1-\kappa_d\Lambda_0)^2\,,\end{aligned}\tag{3.2.35}$$

which reduces to the Biot energy density for a flat beam (3.1.12) by setting $\kappa_d=0$ and using formulas (3.1.18). The minimization of the approximate energy through the system (3.2.34) gives the solutions

$$\Lambda_0=\frac{\alpha^2(1+\bar\kappa_d)+\Gamma^3(1-\bar\kappa_d)+\alpha\Gamma(7(1+\Gamma)+\bar\kappa_d(1-\Gamma))}{\Gamma(14\alpha\Gamma+\Gamma^2(1-\bar\kappa_d)+\alpha^2(1+\bar\kappa_d))}\,\lambda_{oe}\,,\tag{3.2.36}$$

$$\begin{aligned}\Lambda_1=&\frac{\bar\kappa_d(\alpha^2(1+\bar\kappa_d)+\Gamma^3(1-\bar\kappa_d))}{\Gamma(14\alpha\Gamma+\Gamma^2(1-\bar\kappa_d)+\alpha^2(1+\bar\kappa_d))}\,\frac{\lambda_{oe}}{h}+\\&+\frac{\alpha\Gamma((\bar\kappa_d^2+24)(1-\Gamma)+7\bar\kappa_d(1+\Gamma))}{\Gamma(14\alpha\Gamma+\Gamma^2(1-\bar\kappa_d)+\alpha^2(1+\bar\kappa_d))}\,\frac{\lambda_{oe}}{h}\,,\end{aligned}\tag{3.2.37}$$

where $\alpha=E_i/E_e$, $\Gamma=\lambda_{oe}/\lambda_{oi}$ and $\bar\kappa_d=\kappa_d h$ are dimensionless parameters.

1 The elementary actual volume is $dv=\lambda_{om}^3dV$ $(m=i,e)$, being $dV=(1+\kappa_d\zeta)\,dl\,dw\,d\zeta$ the elementary reference volume.

In the plots of Figure 15, the solutions deriving from the minimization of the non-approximate energy (3.2.33) (solide line) and the approximate energy (3.2.35) (dash-dotted line) are compared. The dimensionless curvature κh (left panel) and the mid-axis stretch Λ_0 (right panel) are represented as a function of the distortion of the outer layer λ_{oe} for $\bar{\kappa}_d = 0$ (blue line) and $\bar{\kappa}_d = 0.8$ (orange line), setting $\alpha = 2$, $h = 4$ mm, $\lambda_{oi} = 1$. As for Λ_0, the curves are almost overlapping; as for κh the simplified formula is closer and closer to the full formula for λ_{oe} which tends to 1 and $\bar{\kappa}_d$ decreasing. In the limit of the flat beam ($\bar{\kappa}_d \to 0$) the two models match. The dashed lines (left panel) represent the Timoshenko's linear formula of dimensionless curvature which is tangent to the nonlinear formulas in $\lambda_{oe} = 1$ for small $\bar{\kappa}_d$, as seen in III.

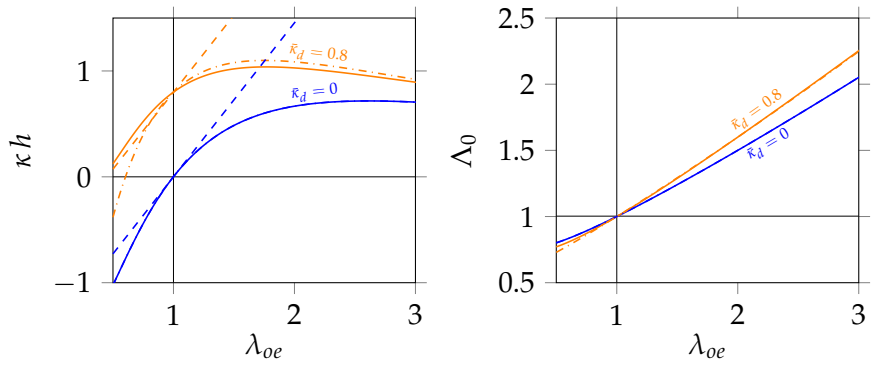

Figure 15: Dimensionless curvature κh (left) and mid-axis stretch Λ_0 (right) versus λ_{oe} for $\bar{\kappa}_d = 0$ (blue line) and $\bar{\kappa}_d = 0.8$ (orange line), fixing $\alpha = 2$, $h = 4$ mm, $\lambda_{oi} = 1$. Solid and dash-dotted lines correspond to the non-approximate and approximate models, respectively; dashed lines (only in the left plot) correspond to the Timoshenko's linear model.

3.3 FLATTENING

Flattening of bilayer naturally curved beams is numerically explored for gels in III. Results are shown in the morphological phase diagrams in Figure III-2 and III-3, where the red dashed isolines represent the locus of points (α, β) and $(\bar{\kappa}_d, \beta)$, respectively, that identify the flat configuration of the beam in stationary conditions.
For generic inelastic distortions, the value of the ratio $\Gamma^\star$ needed to straighten a beam with assigned geometrical and material properties can be found numerically by equating the full nonlinear formula III-4.22 to zero. However, it would be interesting to find an explicit formula that estimates the ratio $\Gamma^\star$ introducing some approximations. An easily usable formula can be derived for a slightly curved beam

equating to zero the expansion of the curvature III-4.22 at the first order in Γ and $\bar{\kappa}_d$ around $\Gamma = 1$ and $\bar{\kappa}_d = 0$:

$$\Gamma^\star = \frac{24\alpha(\alpha^2 + 14\alpha + 1) - \bar{\kappa}_d(43\alpha^3 + 99\alpha^2 - 15\alpha + 1)}{24\alpha(\alpha^2 + 14\alpha + 1) + \bar{\kappa}_d\alpha(\alpha^3 - 15\alpha^2 + 99\alpha + 43)}, \qquad (3.3.38)$$

where it is set $\beta = 1/2$ to ease the reading of the formula. In Figure 16 the approximate formula 3.3.38 (blue lines) is compared with the values of $\Gamma^\star$, obtained numerically, that make the complete formula III-4.22 equal to zero (green triangles), and the following explicit formula for $\Gamma^\star$ which derive from the Timoshenko's curvature III-5.36 (orange lines):

$$\Gamma^\star = \frac{24\alpha\lambda_{oe}}{\bar{\kappa}_d(\alpha^2 + 14\alpha + 1) + 24\alpha\lambda_{oe}}. \qquad (3.3.39)$$

The left panel shows $\Gamma^\star$ versus $\bar{\kappa}_d$ ranging between 0 (flat beam) and 1, fixing $\alpha = 2$, $h = 4$ mm and $\lambda_{oe} = 1$. The right panel shows $\Gamma^\star$ versus λ_{oe} ranging between 0.5 and 3, fixing $\alpha = 2$, $h = 4$ mm and $\bar{\kappa}_d = 0.4$. It can be seen that the three models match for slightly curved beams and when λ_{oe} is close to 1; whereas, for increasing values of $\bar{\kappa}_d$ the Timoshenko's and approximate formulas overestimate the ratio $\Gamma^\star$. Moreover, the approximate formula and the full model do not depend on λ_{oe}.

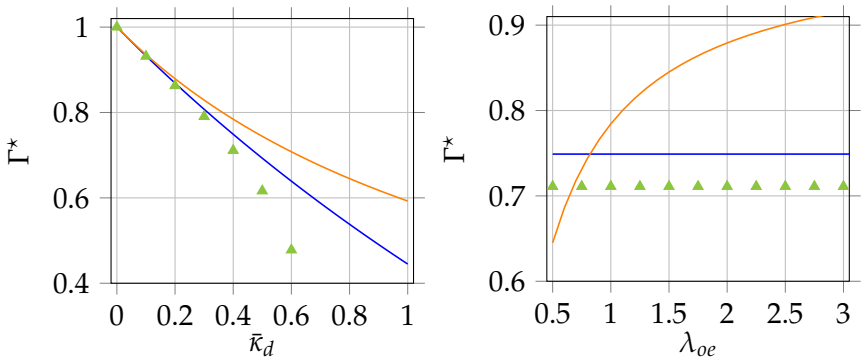

Figure 16: Value of the ratio $\Gamma^\star$ needed to straighten a naturally curved beam versus the dimensionless curvature $\bar{\kappa}_d$ (left panel) and the distortion of the external layer λ_{oe} (right panel). Triangles correspond to the values of $\Gamma^\star$ obtained numerically from the complete formula III-4.22; blue and orange lines correspond to approximate formula (3.3.38) and the Timoshenko's linear model (3.3.39). In the left plot the fixed parameters are $\alpha = 2$, $h = 4$mm, $\lambda_{oe} = 1$; in the right plot the fixed parameters are $\alpha = 2$, $h = 4$ mm, $\bar{\kappa}_d = 0.4$.

4

ELASTIC AND INELASTIC PROCESSES IN POLYMER GELS

As described in Chapter 2, elastic and inelastic growth are two distinct processes. The following example shows the difference in terms of energy between the two processes. Consider two flat bilayer beams with the same size and elastic moduli. Both beams have a passive elastic layer and an active layer. The latter, in one case grows inelastically, while in the other case it grows elastically through the absorption of solvent. The mismatch caused by the growth of a single layer generates both planar bending and elongation of the middle axis.
The plots in Figure 17 show some results of numerical simulations based on the 3D models of finite elasticity with distortions, for the inelastic growth, and stress-diffusion, for the elastic growth, presented in Sections 4.2 and 4.1, respectively. The total elastic energy (bottom panel of Figure 17) $\mathcal{U}_e$ is in both the cases based on the neo-Hookean form, suitable for rubber-like materials, and it is computed for different values of the average deformation $\bar{\lambda} = (1/V) \int J \, dV$, where V is the volume of the beam and $J = \det \mathbf{F}$, with $\mathbf{F}$ the visible deformation gradient. As growth in the beams is not compatible due to the presence of the passive layer, in both cases there is a storage of elastic energy, but of a different amount: in the inelastic case (blue line) it derives only from the incompatibility between the two layers; in the elastic case (orange line) another contribution is added due to the elastic stretching of the polymer chains after the absorption of solvent. Although the elastic energy is quite different in the two examples, the mid-axis stretch and the curvature attained is almost the same, as the top-left and top-right panels of Figure 17 show.
So, in terms of energy, swelling and growth are quite different phenomena, especially when they come together. There is a clear distinction between them and a full modeling of their interactions is crucial to accurately describe the combined processes [14]. Nevertheless, reduced models of growing beams have often been used to study swelling in thin structures [47, 61, 62]. The reason is that, for thin structures, the growth approach to the elastic problem, based on the multiplicative decomposition of the deformation gradient, yields simplified models which allow for semi-analytical solutions.

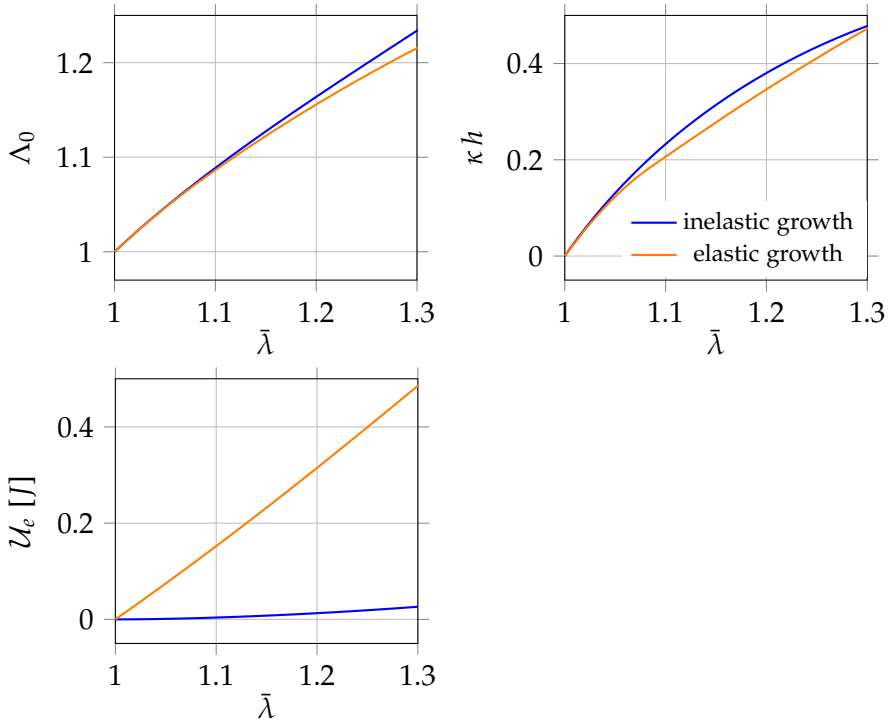

Figure 17: Mid-axis stretch Λ_0 (top-left), dimensionless curvature κh (top-right) and total elastic energy $\mathcal{U}_e$ (bottom) versus the average deformation $\bar{\lambda} = (1/V) \int J \, dV$ of two identical flat bilayer beams consisting of a passive layer and an active layer. In one case the active layer undergoes an inelastic distortion (blue lines), in the other case it swells due to solvent absorption (orange lines).

4.1 SWELLING PROCESSES IN POLYMER GELS

Swelling in polymer gels is studied within the stress-diffusion continuum model presented and discussed in [16, 47–49]. Water-polymer mixture is modeled as a homogenized continuum body where a flow of solvent is allowed [12, 32, 33]. Two states of a gel body are introduced: a reference configuration $\mathcal{B}_d$ identified with its dry state, and an actual configuration $\mathcal{B}_t$ identified with its swollen state (see Figure 18). The chemo-mechanical state of the body is described by two state variables: the displacement field $\mathbf{u}_d(X_d, t)$ ($[\mathbf{u}_d]$ =m) from $\mathcal{B}_d$ and the molar solvent concentration per unit dry volume $c_d(X_d, t)$ ($[c_d]$ =mol/m^3), where $X_d \in \mathcal{B}_d$ is a material point and $t \in \mathcal{T}$ is an instant of the time line $\mathcal{T}$. The displacement $\mathbf{u}_d$ gives the actual position $x \in \mathcal{B}_t$ at time t of a point X_d as $x = X_d + \mathbf{u}_d(X_d, t) = f_d(X_d, t)$.

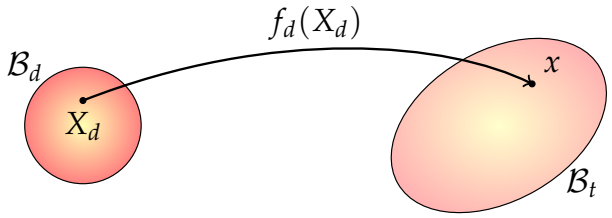

Figure 18: Reference and actual configurations.

The hypothesis that any change in volume of the gel body is due only to solvent uptake or release results in the following volumetric constraint:

$$J_d = \det \mathbf{F}_d = \hat{J}_d(c_d) = 1 + \Omega c_d \,, \tag{4.1.40}$$

which couples the two state variables. Therein, $\mathbf{F}_d = \mathbf{I} + \nabla \mathbf{u}_d$ is the deformation gradient and Ω ($[\Omega]$ =m^3/mol) is the molar volume of the solvent.
The classical Flory-Rehner theory describing the swelling of cross-linked polymer networks [25, 26] postulates the free-energy per unit dry volume $\psi(\mathbf{F}_d, c_d)$ to be additively decomposed into an elastic part $\psi_e(\mathbf{F}_d)$ and a mixing part $\psi_m(c_d)$. The volumetric constraint (4.1.40) is taken into account through a relaxed free-energy ψ_r defined as

$$\psi_r(\mathbf{F}_d, c_d, p) = \psi_e(\mathbf{F}_d) + \psi_m(c_d) - p(J_d - \hat{J}_d(c_d)) \,, \tag{4.1.41}$$

where the Lagrangian multiplier p ($[p]$ =Pa) represents the pressure which reacts to the volumetric constraint. The constitutive equations for the dry-reference stress $\mathbf{S}_d$ ($[\mathbf{S}_d]$ =Pa) and for the chemical potential μ ($[\mu]$ =J/mol) stem from the dissipation principle [13] and prescribe that

$$\mathbf{S}_d = \hat{\mathbf{S}}_d(\mathbf{F}_d) - p\mathbf{F}_d^\star \quad \text{and} \quad \mu = \hat{\mu}(c_d) + p\Omega \,, \tag{4.1.42}$$

with

$$\hat{\mathbf{S}}_d(\mathbf{F}_d) = \frac{\partial \psi_e}{\partial \mathbf{F}_d} \quad \text{and} \quad \hat{\mu}(c_d) = \frac{\partial \psi_m}{\partial c_d} \,, \tag{4.1.43}$$

being $\mathbf{F}_d^\star = J_d \mathbf{F}_d^{-T}$. The Flory-Rehner thermodynamic model prescribes that the elastic component ψ_e of the free-energy has a neo-Hookean form, and the polymer-water mixing energy ψ_m has the Flory-Huggins form:

$$\psi_e(\mathbf{F}_d) = \frac{G}{2}(\mathbf{F}_d \cdot \mathbf{F}_d - 3) \,, \quad \psi_m(c_d) = \frac{\mathcal{R}T}{\Omega} h(c_d) \,, \tag{4.1.44}$$

with

$$h(c_d) = \Omega c_d \log\left(\frac{\Omega c_d}{1 + \Omega c_d}\right) + \chi \frac{\Omega c_d}{1 + \Omega c_d} \,, \quad [h] = 1 \,, \tag{4.1.45}$$

being G ($[G]$ =J/m^3) the shear modulus of the dry polymer, $\mathcal{R}$ ($[\mathcal{R}]$ =J/(K mol)) the universal gas constant, T ($[T]$ =K) the temperature, and χ the dimensionless Flory parameter, which measure the dis-affinity between gel and solvent. From equations (4.1.44) and (4.1.45), together with the volumetric constraint (4.1.40) which provides the relation $c_d = (J_d - 1)/\Omega$, the constitutive prescriptions (4.1.43) give

$$\hat{\mathbf{S}}_d(\mathbf{F}_d) = G\mathbf{F}_d \quad \text{and} \quad \hat{\mu}(J_d) = \mathcal{R}T\left(\log\frac{J_d - 1}{J_d} + \frac{1}{J_d} + \frac{\chi}{J_d^2}\right). \tag{4.1.46}$$

The balance of forces, in absence of bulk loads and neglecting the inertial forces, and the conservation of solvent mass, in absence of bulk sources, are

$$\mathbf{o} = \operatorname{div}\mathbf{S}_d \quad \text{and} \quad \dot{c}_d = -\operatorname{div}\mathbf{h}_d \quad \text{in } \mathcal{B}_d\,, \tag{4.1.47}$$

with the reference solvent flux $\mathbf{h}_d$ ($[\mathbf{h}_d]$ =mol/(m^{2}s)), driven by the dissipation principle, constitutively determined in terms of the positive definite mobility tensor $\mathbf{M}$ as

$$\mathbf{h}_d = -\mathbf{M}\nabla\mu\,, \quad \text{with} \quad \mathbf{M} = \frac{D}{\mathcal{R}T}c_d\mathbf{C}_d^{-1}\,, \tag{4.1.48}$$

where $\mathbf{C}_d = \mathbf{F}_d^T\mathbf{F}_d$, and D ($[D]$ =m^2/s) is the diffusivity. Here $\mathbf{M}$ is assumed to be isotropic during any process as in [12], where a thorough discussion on constitutive issues about the mobility can be found. A full discussion on the different isotropic representations for $\mathbf{M}$ is reported in [48].
Balance equations (4.1.47) are supplemented by Neumann-type boundary conditions on the stress vector $\mathbf{S}_d\mathbf{m}$ and on the solvent flux $\mathbf{h}_d \cdot \mathbf{m}$:

$$\mathbf{S}_d\mathbf{m} = \bar{\mathbf{t}} \quad \text{in } \partial_t\mathcal{B}_d \quad \text{and} \quad \mathbf{h}_d \cdot \mathbf{m} = \bar{q}_s \quad \text{in } \partial_q\mathcal{B}_d\,, \tag{4.1.49}$$

and Dirichlet-type boundary conditions on the displacement $\mathbf{u}_d$ and the concentration c_d:

$$\mathbf{u}_d = \bar{\mathbf{u}} \quad \text{in } \partial_u\mathcal{B}_d \quad \text{and} \quad c_d = \bar{c}_s \quad \text{in } \partial_c\mathcal{B}_d\,, \tag{4.1.50}$$

being $\partial_t\mathcal{B}_d$, $\partial_q\mathcal{B}_d$, $\partial_u\mathcal{B}_d$ and $\partial_c\mathcal{B}_d$ the portion of the boundary $\mathcal{B}_d$ of unit normal $\mathbf{m}$ where tractions, fluxes, displacements and concentration, respectively, are prescribed. Usually, the chemical boundary condition (4.1.50) is replaced by the implicit condition $\hat{\mu}(c_s) + p\Omega = \mu_e$ on the concentration field c_s at the boundary $\partial_c\mathcal{B}_d$ controlled by assigning the external chemical potential μ_e. Finally, the model is completed by the initial conditions for the state variables $u_d = u_{do}$ and $c_d = c_{do}$ on $\mathcal{B}_d$ at $t = 0$.

The theory of bulk growth is based on the multiplicative decomposition of the visible deformation in an inelastic deformation $\mathbf{F}_o$ and in an elastic deformation $\mathbf{F}_e$, such that $\mathbf{F} = \mathbf{F}_e\mathbf{F}_o$ (Figure 19). The distortion $\mathbf{F}_o$ maps the reference state $\mathcal{B}$ into a natural state $\mathcal{B}_o$, which is stress-free, but usually do not correspond to any realizable deformation. The main difference with the stress-diffusion-model shown in Section 4.1 is the assumption that there is no exchange of mass, but a local change of the ground state.

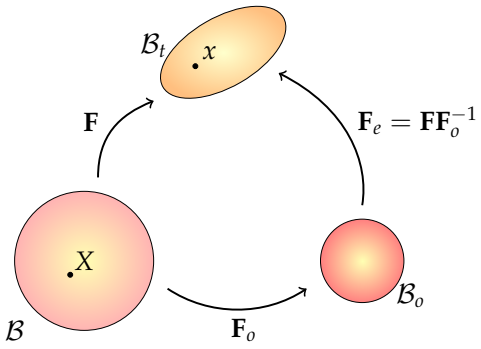

Figure 19: Multiplicative decomposition of the deformation gradient.

The problem is described by one state variable: the displacement field $\mathbf{u}(X)$, which gives the actual position $x = X + \mathbf{u}(X)$ of a material point $X \in \mathcal{B}$. There is no dependence on time as the aim is to determine only the equilibrium states of the polymer bodies. The tensor-valued field $\mathbf{F}_o$ is given and does not constitute a state variable; in addition, it is assumed that $\mathbf{F}_o$ is the only cause of volume changes. This translates into the volumetric constraint

$$J = \det \mathbf{F} = J_o = \det \mathbf{F}_o \,, \tag{4.2.51}$$

which is equivalent to assigning an isochoric constraint to the elastic deformation $\mathbf{F}_e$, that is, such that $J_e = \det \mathbf{F}_e = 1$. Introducing the pressure p as a Lagrangian multiplier, the volumetric constraint is included in the definition of the elastic free-energy $\psi_e(\mathbf{F}_e)$ as follows:

$$\psi_r(\mathbf{F}_e, p) = \psi_e(\mathbf{F}_e) - p(J - J_o) \,, \tag{4.2.52}$$

which provides, through the dissipation inequality, the constitutive equation for the reference stress $\mathbf{S}$:

$$\mathbf{S} = \hat{\mathbf{S}}(\mathbf{F}_e) - p\mathbf{F}^\star \,, \quad \text{with} \quad \hat{\mathbf{S}}(\mathbf{F}_e) = \frac{\partial \psi_e}{\partial \mathbf{F}_e} \,, \tag{4.2.53}$$

where, for a neo-Hookean material, the elastic free-energy has the form

$$\psi_e(\mathbf{F}_e) = \frac{G}{2}(\mathbf{F}_e \cdot \mathbf{F}_e - 3) \,, \tag{4.2.54}$$

and leads to the following equation for $\mathbf{S}$:

$$\mathbf{S} = G\mathbf{F}\mathbf{F}_o^{-1}\mathbf{F}_o^{\star} - p\mathbf{F}^{\star}\,, \tag{4.2.55}$$

being $\mathbf{F}^{\star} = J\mathbf{F}^{-T}$ and $\mathbf{F}_o = J_o\mathbf{F}_o^{-T}$. The actual (Cauchy) stress $\mathbf{T}$ can be obtained from $\mathbf{S}$ through $\mathbf{T} = J^{-1}\mathbf{S}\mathbf{F}^T$. For a spherical tensor $\mathbf{F}_o = \lambda_o\mathbf{I}$, as in I, the constitutive equation (4.2.55) becomes

$$\mathbf{S} = G\lambda_o\mathbf{F} - p\mathbf{F}^{\star}\,. \tag{4.2.56}$$

As $\mathbf{F}_o$ is a given of the problem, no balance law for the remodeling actions [9, 14] is here introduced; the only balance law considered is the balance of forces $\operatorname{div}\mathbf{S} = \mathbf{o}$, in absence of bulk loads and inertial forces. Finally, the boundary conditions on the displacement $\mathbf{u} = \bar{\mathbf{u}}$ or on the stress vector $\mathbf{S}\mathbf{m} = \bar{\mathbf{t}}$ complete the formulation of the problem.

4.3 Computational analysis of growing beams

The stress-diffusion continuum model is solved numerically with a finite element method through implementation in the finite element software COMSOL Multiphysics [48]. The balance equations (4.1.47) and the volumetric constraint (4.1.40) are reformulated in weak form, and the problem is set as follows: find $\mathbf{u}_d$, c_d, p such that it holds

$$0 = \int_{\mathcal{B}_d} \left(-\mathbf{S}_d\cdot\nabla\tilde{\mathbf{u}}_d - \dot{c}_d\cdot\tilde{c}_d + \mathbf{h}_d\cdot\nabla\tilde{c}_d + [J_d - \hat{J}(c_d)]\cdot\tilde{p}\right)\,, \tag{4.3.57}$$

for all test fields $\tilde{\mathbf{u}}_d$, compatible with the kinematic constraints, $\tilde{c}_d$ and $\tilde{p}$. The constitutive equations shown in the previous section hold for the stress $\mathbf{S}_d$ and the flux $\mathbf{h}_d$. As for the boundary conditions, it is assumed zero traction and assigned a displacement $\bar{\mathbf{u}}$ that eliminates any rigid motion without generating reaction forces. The implicit boundary condition on the concentration field c_s in weak form is

$$0 = \int_{\partial_c\mathcal{B}_d} [\hat{\mu}(c_s) + p\Omega - \mu_e]\cdot\tilde{c}_s\,. \tag{4.3.58}$$

Also the problem of finite elasticity with distortions presented in Section 4.2 is solved numerically through a finite element method, and stated as follows: find a displacement $\mathbf{u}$ and a pressure p such that, for all test functions $\tilde{\mathbf{u}}$, compatible with the kinematic constraints, and $\tilde{p}$ it holds:

$$0 = \int_{\mathcal{B}} \left(-\mathbf{S}\cdot\nabla\tilde{\mathbf{u}} + [J - J_o]\cdot\tilde{p}\right)\,. \tag{4.3.59}$$

4.4 Eversion and flattening under swelling

The simplest way to realize a gel-based actuator is to create a non-homogeneous structure by stacking two homogeneous strips one on

the other. The estimation of the geometrical and mechanical characteristics which produce a specific shape of such actuator is challenging. In III the swelling-induced eversion and flattening of naturally curved bilayer gel beams is discussed through exact numerical models and approximate explicit formulas. The aim of the work is to investigate how geometrical and material parameters determine variations in curvature in a gel beam, initially dry, consisting of two layers of different thickness and elastic modulus, once immersed in a solvent bath with assigned chemical potential. Indeed, as the two layers have different elastic properties, they would like to swell differently if they where free from each other but, since they are glued together, the bilayer bends. The problem is set within the context of continuum mechanics, studying the swelling processes with the fully nonlinear three-dimensional stress-diffusion model presented in Section 4.1, and solved numerically with a finite element method as described in Section 4.3. A campaign of numerical experiments is carried out by varying some key parameters such as the geometrical parameters β and $\bar{\kappa}_d$, and the material parameter α, and the results are summarized in the morphological phase diagrams of emerging curvature patterns at steady-state in Figures III-2 and III-3. They represent the curvature as a function of α and β, and as a function of $\bar{\kappa}_d$ and β, respectively. They show how an appropriate combination of design parameters can generate a flattening (white regions) or eversion (red regions) of the beam at equilibrium, going from a dry state to wet state, and fixing the environmental conditions (chemical potential and temperature of the solvent bath).

International Journal of Mechanical Sciences 161–162 (2019) 105071

Contents lists available at ScienceDirect

International Journal of Mechanical Sciences

journal homepage: www.elsevier.com/locate/ijmecsci

Swelling-induced eversion and flattening in naturally curved gel beams

Daniele Battista, Michele Curatolo, Paola Nardinocchi*

Dipartimento di Ingegneria Strutturale e Geotecnica Sapienza Università di Roma, via Eudossiana 18 Roma I-00184, Italy

ARTICLE INFO

Keywords:
Stress-diffusion
Swelling
Bilayer beams
Change in curvature

ABSTRACT

This paper investigates swelling-induced eversion and flattening in curved bilayer gel beams. An explicit formula is produced to evaluate the change in curvature induced by large swelling deformations. The validity is tested against a fully coupled nonlinear three–dimensional stress-diffusion model. Limit situations for nearly-homogeneous and slightly curved beams are discussed.

1. Introduction

Designing changes in size and shape of soft materials is challenging. The effectiveness of soft actuators, where deformations and displacements are triggered through a wide range of external stimuli [1–8], depends on the ability to achieve prescribed changes in the system. Specifically, in gel–based actuators, shape control involves materials which are swellable due to the capability of these materials to absorb solvents [9].

It is largely recognized that a gel structure realized with chemically distinct regions can swell freely, giving rise to non–homogeneous deformation patterns which resemble well–known macroscopic structural deformations [10,11]. Two key issues are: the estimation of the geometrical and mechanical characteristics of the non–homogeneous gel systems which produce three–dimensional shapes, under free–swelling conditions; the capability to realize non–homogeneous gel systems with the estimated characteristics.

Ref. [10] is focused on non–homogeneous flat gel structures, and flat structures are the subject of numerous studies [12–16]. The same problems can also be investigated with reference to non–homogeneous and naturally curved structures. In this case, the range of deformation patterns is wide and extremely interesting, including eversion and flattening of the structure.

The investigation concentrates on bilayered naturally curved gel beams, which are non–homogeneous along the thickness and represent special cases of non–homogeneous gel systems with beam–like homogeneous components. These kind of structures have been largely studied when they are flat (see Refs. [17–20]). However, the behaviour of curved composites under swelling is still largely unexplored.

The problem is set within the context of continuum mechanics, where swelling–induced deformation processes can be studied through the fully nonlinear three–dimensional stress–diffusion model at our disposal [17,21–27] (see also [28–30]). The model is utilized to find free–swelling solutions in the stress–diffusion problem corresponding to non–homogeneous and naturally curved gel beams. Through the finite element solution of the problem, we show how different changes in beam curvature can be produced at zero force and torque, depending on the mismatch between the shear moduli of the two beam–like parts. We also show how swelling always induces a change in curvature, which can be interpreted following [31] as a pure stretching deformation for two beam–like parts that have the same shear modulus.

In addition, another important aspect considered concerns the approximate modeling of swelling–driven large deformations in non–homogeneous naturally curved thin structures, following [17]. It delivers explicit and complex formulae that estimate the change in beam curvature. The model is based on the assumption that within each homogeneous beam–like part of the system, bending deformation can be multiplicatively split into the uniform free–swelling stretch that would take place if the part was free from the rest of the beam and a further elastic component. The uniform free–swelling stretches of each homogeneous beam are determined by the mechano–chemical equilibrium equations which use the Flory–Rehner stress–diffusion model and depend on three material parameters: the shear modulus of the polymer, the chemical potential of the bath and the Flory parameter that measures the dis-affinity between the aforementioned polymer and solvent. The elastic deformations come out from the multiplicative decomposition, once assured the compatibility of the global bending deformation. Within the gel beam, elastic deformations deliver internal stresses corresponding to null forces and torques on each cross section of the beam, in the absence of external forces.

We show through appropriate morphological diagrams how geometrical and material parameters determine changes in the curvature of the structure which can deliver eversion of a naturally curved bilayer beam and flattening. Limit cases corresponding to nearly homogeneous

* Corresponding author.
E-mail addresses: daniele.battista@uniroma1.it (D. Battista), michele.curatolo@uniroma1.it (M. Curatolo), paola.nardinocchi@uniroma1.it (P. Nardinocchi).

https://doi.org/10.1016/j.ijmecsci.2019.105071
Received 6 May 2019; Received in revised form 11 July 2019; Accepted 6 August 2019
Available online 7 August 2019

gel beams and nearly flat beams are identified and discussed. The Timoshenko formula for bilayer thermal beams is also recovered within the limits of a slight curvature in the original dry beam and small deformations [32].

2. Background

We describe swelling–induced deformation processes in bilayered gel beams which are naturally curved, through a multiphysics continuum model based on the balance equations for forces and solvent, on the thermodynamics inequalities restricting the class of admissible constitutive prescriptions, and on the choice of a free energy density which accounts for both the elastic and mixing contributions. As we aim to set up a series of numerical experiments, we shortly review below the model, already presented and discussed in [17,21,22,33], focusing on the weak form of the above equations which have been implemented within the commercial software COMSOL Multiphysics.

2.1. State variables and thermodynamics

The reference configuration $\mathcal{B}_d$ of the gel body is identified with its dry state and is a beam-like three-dimensional region of the Euclidean space $\mathcal{E}$ with boundary $\partial\mathcal{B}_d$ of outward unit normal $\mathbf{n}$. We denote with $\mathcal{T}$ the time line and describe the chemo-mechanical state of the body by two state variables: the displacement field $\mathbf{u}_d : \mathcal{B}_d \times \mathcal{T} \to \mathrm{V}\mathcal{E}\,, (X_d, t) \mapsto \mathbf{u}_d(X_d, t)$ and the water concentration $c_d : \mathcal{B}_d \times \mathcal{T} \to \mathbb{R}\,, (X_d, t) \mapsto c_d(X_d, t)$. The displacement $\mathbf{u}_d$ gives the actual position x at time t of a point X_d as $x = X_d + \mathbf{u}_d(X_d, t)$, whereas the water concentration c_d gives the moles of water per unit dry volume at $X_d + \mathbf{u}_d(X_d, t)$.

The two variables are coupled by the volumetric constraint which forces the change in volume of the gel body to be only due to solvent uptake or release:

$$J_d = \hat{J}(c_d) = 1 + \Omega c_d \quad \text{with} \quad J_d = \det \mathbf{F}_d \quad \text{and} \quad \mathbf{F}_d = \mathbf{I} + \nabla \mathbf{u}_d\,, \tag{2.1}$$

with Ω as the molar volume of the solvent ($[\Omega] = \mathrm{m}^3/\mathrm{mol}$).

We take into account the constraint $(2.1)_1$ by considering a relaxed free–energy ψ_r based on the Flory–Rehner free-energy $\psi(\mathbf{F}_d, c_d)$ per unit dry volume, which includes the volumetric constraint through the Lagrangian multiplier p:

$$\psi_r(\mathbf{F}_d, c_d, p) = \psi(\mathbf{F}_d, c_d) - p(J_d - \hat{J}(c_d))\,, \quad \psi(\mathbf{F}_d, c_d) = \psi_e(\mathbf{F}_d) + \psi_m(c_d)\,, \tag{2.2}$$

with ψ additively decomposed into the elastic ψ_e and mixing ψ_m part. The constitutive equations for the stress $\mathbf{S}_d$ and the chemical potential μ come from dissipation issues and prescribe that

$$\mathbf{S}_d = \hat{\mathbf{S}}_d(\mathbf{F}_d) - p\mathbf{F}_d^{\star} \quad \text{and} \quad \mu = \hat{\mu}(c_d) + p\Omega\,, \tag{2.3}$$

with

$$\hat{\mathbf{S}}_d(\mathbf{F}_d) = \frac{\partial \psi_e}{\partial \mathbf{F}_d} \quad \text{and} \quad \hat{\mu}(c_d) = \frac{\partial \psi_m}{\partial c_d}\,, \tag{2.4}$$

being $\mathbf{F}_d^{\star} = J_d \mathbf{F}_d^{-T}$. Moreover, granted for the volumetric constraint $(2.1)_1$ and with a light abuse of notation, we also will write $\hat{\mu}(c_d) = \hat{\mu}(J_d)$ with $c_d = (J_d - 1)/\Omega$. The Flory-Rehner thermodynamics delivers the following consitutive prescriptions for $\hat{\mathbf{S}}_d(\mathbf{F}_d)$ and $\hat{\mu}(J_d)$:

$$\hat{\mathbf{S}}_d(\mathbf{F}_d) = G\,\mathbf{F}_d \quad \text{and} \quad \hat{\mu}(J_d) = \mathcal{R}\,T\left(\log\frac{J_d - 1}{J_d} + \frac{1}{J_d} + \frac{\chi}{J_d^2}\right). \tag{2.5}$$

Finally, the reference water flux $\mathbf{h}_d$ ($[\mathbf{h}_d]$ =mol/m^{2}s) is represented as $\mathbf{h}_d = \hat{\mathbf{h}}_d(\mathbf{F}_d, c_d, p) = -\mathbf{M}(\mathbf{F}_d, c_d)\nabla(\hat{\mu}(c_d) + p\Omega)$ in terms of the mobility tensor $\mathbf{M}$ which is positive definite in such a way to satisfy the dissipation inequality.

2.2. Balance equations and boundary conditions

We pose the balance equations of the problem in integral form as follows: find $\mathbf{u}_d$, c_d and p such that, for all test fields $\tilde{\mathbf{u}}_d$, $\tilde{c}_d$, and $\tilde{p}$, it holds

$$0 = \int_{\mathcal{B}_d} \left(-[\mathbf{S}_d(\mathbf{F}_d) - p\,\mathbf{F}_d^{\star}] \cdot \nabla\tilde{\mathbf{u}}_d - \dot{c}_d \cdot \tilde{c}_d + \mathbf{h}_d \cdot \nabla\tilde{c}_d + [J_d - \hat{J}(c_d)] \cdot \tilde{p}\right). \tag{2.6}$$

Boundary conditions are of mechanical and chemical nature. The firsts are easy to handle, as we assume zero tractions and assign a displacement $\bar{\mathbf{u}}_d$ on the boundary that eliminates any rigid motion without generating reaction forces. On the contrary, tackling the chemical boundary conditions is more tricky, as it is not possible to control the solvent source q_s at the surface, nor the surface concentration c_s. So, following [25–27], we assume to control the chemical potential μ on the surface and set it equal to the chemical potential $\bar{\mu}$ of the bath:

$$0 = \int_{\partial_c\mathcal{B}_d} [\,\hat{\mu}(c_s) + p\,\Omega - \bar{\mu}\,] \cdot \tilde{c}_s\,. \tag{2.7}$$

Moreover, as we control the state variable c_s, the surface flux source q_s must be considered as a reaction, which is unknown a priori, and whose evaluation a posteriori yields poor approximations. So, we also require that

$$0 = \int_{\partial_c\mathcal{B}_d} [\,(c_d - c_s)\,\tilde{q}_s + q_s\,(\tilde{c}_d - \tilde{c}_s)\,]\,. \tag{2.8}$$

All in all, the complete problem is reformulated as follows: find $\mathbf{u}_d$, c_d, p, c_s, and q_s such that, for any test functions $\tilde{\mathbf{u}}_d$, $\tilde{c}_d$, $\tilde{p}$, $\tilde{c}_s$, and $\tilde{q}_s$, Eqs. (2.6)–(2.8) hold; the three fields $\mathbf{u}_d$, c_d, p are defined in $\mathcal{B}_d \times \mathcal{T}$, while the two fields c_s and q_s are defined on $\partial_c\mathcal{B}_d \times \mathcal{T}$.

3. Numerical swelling tests on a curved beam

We fix an orthonormal basis $\{\mathbf{e}_1, \mathbf{e}_2, \mathbf{e}_3\}$ of the translation space $\mathcal{V}$ of $\mathcal{E}$, and consider a gel beam that at its dry state has got as axis a circular arc of curvature $\kappa_d = 1/R_m$ laying in the plane of unit normal $\mathbf{e}_3$. The arc has length $L = 2\bar{\Theta}R_m$, with $2\bar{\Theta}$ the angle amplitude. A cylindrical basis $\{\mathbf{e}_R, \mathbf{e}_\Theta, \mathbf{e}_3\}$ is introduced, with $\mathbf{e}_R = \sin\Theta\mathbf{e}_1 + \cos\Theta\mathbf{e}_2$ and $\mathbf{e}_\Theta = \cos\Theta\mathbf{e}_1 - \sin\Theta\mathbf{e}_2$; the corresponding coordinates are (R, Θ, Z). The cross-section of the beam is assumed in the form of a plane rectangular region of thickness $h = L/10$ and width w, with unit normal $\mathbf{e}_\Theta$ (see Fig. 1).

The beam is assumed to be composed of two stacked beam-like layers with thickness $h_i = \beta h$ the inner (intrados) layer and $h_e = (1 - \beta)h$ the outer (extrados) layer, being $\beta \in (0, 1)$; the corresponding shear moduli of the two layers are G_i and G_e and, in general, $\alpha = G_i/G_e \neq 1$.

When immersed in a solvent bath with assigned chemical potential $\bar{\mu}$, both the layers of the gel beam would swell isotropically, if they were free, with different homogeneous equilibrium free-swelling ratio: λ_{oi} is the free-swelling stretch corresponding to the intrados layer and λ_{oe} is the one corresponding to the extrados layer. Both of them are given by the following equation

$$\mathcal{R}\,T\left(\log\frac{\lambda_o^3 - 1}{\lambda_o^3} + \frac{1}{\lambda_o^3} + \frac{\chi}{\lambda_o^6}\right) + \frac{G}{\lambda_o}\Omega = \bar{\mu}\,, \tag{3.9}$$

with $\lambda_o = \lambda_{oi}$ and $G = G_i$ for the intrados layer, and $\lambda_o = \lambda_{oe}$ and $G = G_e$ for the extrados one. Eq. (3.9) yields the homogeneous isotropic solution of the stress-diffusion problem corresponding to a body which attains a swollen stress-free state once embedded into a pure water bath of known chemical potential $\bar{\mu} = 0$. As $\alpha \neq 1$, λ_{oi} is different from the equilibrium swelling ratio λ_{oe} of the extrados beam. As the two homogeneous beam-like layers realize an assembly and swell differently, a macroscopic bending is induced which may determine a further curving of the beam, which can yield an increase or a decrease of the beam curvature, other than an extension of the beam. Higher is the mismatch between the two moduli, and hence between the two free-swelling stretches λ_{oi}

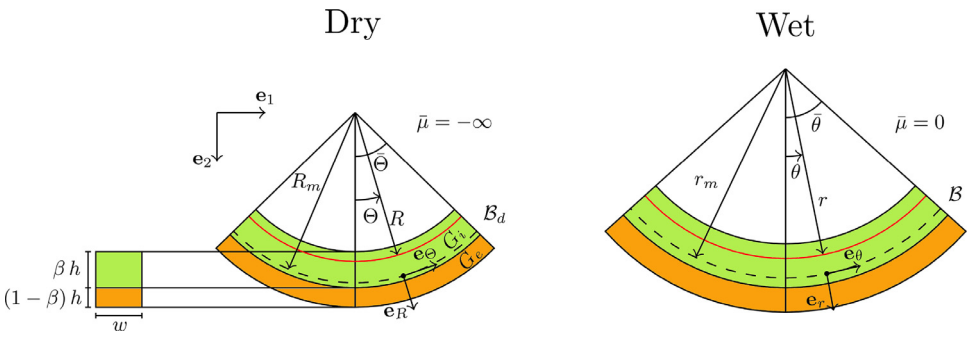

Fig. 1. Dry and wet configurations of the naturally curved bilayered beam; the plane of unit normal $\mathbf{e}_3$ is the flexure plane.

and λ_{oe}, higher is the change of curvature realized by the beam. With the aim to investigate the dependence of the change of curvature on the key geometrical and material parameters, we plan and implement a series of numerical experiments. We consider a naturally curved dry bilayer beam of curvature κ_d; moreover, we assume the ratio between the shear moduli $\alpha \neq 1$, and also assume that the ratio β take values in between 0 (homogeneous beam with $G = G_i$) and 1 (homogeneous beam with $G = G_e$). More specifically, the limit case $\alpha = 1$ and/or $\beta = 1$ corresponding to a homogeneous beam will also be considered. All along the experiments, we assume to control the chemical potential $\bar{\mu}$ of the external environment, and take it as a function of the relative humidity RH: $\bar{\mu} = RT \log RH$, with the temperature T as known.

We are in general interested in the equilibrium solution of the stress-diffusion problem; hence, we use the `Stationary Solutor` in the finite element software COMSOL Multiphysics to look for them, implementing the Eqs. (2.6)-(2.8) with $\dot{c}_d = 0$. The numerical solution delivers (right Cauchy-Green) strain $\mathbf{C} = \mathbf{F}_d^T \mathbf{F}_d$ and (Cauchy) stress $\mathbf{T} = (1/J_d)\mathbf{S}_d \mathbf{F}_d^T$ at any point of the beam. In particular, with reference to the reference system illustrated in Fig. 1, we evaluate the longitudinal axis stretch as

$$\Lambda_0(\Theta) = (\mathbf{C}(R_m, \Theta, 0)\mathbf{e}_\Theta(\Theta) \cdot \mathbf{e}_\Theta(\Theta))^{1/2}\,. \tag{3.10}$$

The new curvature κ realized by the beam axis is evaluated by considering the cylindrical surface whose directrix is the beam axis. Denoting with $\mathbf{a}$ and $\mathbf{b}$ the first and second fundamental forms of that surface, we get the mean curvature H of the surface as

$$H = \frac{1}{2}\mathrm{tr}(\mathbf{a}^{-1}\mathbf{b}) = \frac{\kappa_1 + \kappa_2}{2}\,, \tag{3.11}$$

and, being one of the two principal curvatures equal to zero, say $\kappa_2 = 0$, we also get the curvature $\kappa = \kappa_1$ of the beam.

3.1. Geometrical and material determinants of swelling-induced bending

The goal of the numerical experiments is to investigate how far we can go from the naturally curved state by changing some key parameters of the model such as the geometrical parameters β and $\bar{\kappa}_d = \kappa_d h$, and the material parameter α, when the beam goes from a dry state (we think the beam embedded into an environment with chemical potential $\mu = -\infty$) to a wet state (in this case, we think the beam embedded into an environment with chemical potential $\bar{\mu} = RT \log RH$). Our aim is to build a morphological phase diagram of emerging curvature patterns for different values of α, β and $\bar{\kappa}_d$. Hence, we start fixing the environmental conditions, that is, the chemical potential $\bar{\mu}$ and the temperature T of the bath. We also fix some geometric and material features such as the length L, thickness h, and width w of the beam, the shear modulus G_e of the extrados layer and the Flory parameter χ which is assumed to be the same in the two layers. Their values are shown in Table 1. So, numerical experiments involve beams with different dry curvature κ_d, thicknesses ratio β, and shear moduli ratio α, and the outcomes of the numerics are shown in the contour plots in Figs. 2 and 3.

The first diagram is the morphological diagram corresponding to a dry and naturally curved beam with $\kappa_d = 50\ \mathrm{m}^{-1}$. The diagram shows

Table 1
Numerical values of the parameters.

Parameter	Symbol and value
Length	$L = 40$ mm
Thickness	$h = 4$ mm
Width	$w = 1$ mm
Shear modulus of the outer layer	$G_e = 50$ kPa
Dis-affinity	$\chi = 0.4$
Molar volume	$\Omega = 6.023 \times 10^{-5}$ m^3/mol
External chemical potential	$\bar{\mu} = 0$ J/mol
Temperature	$T = 293$ K

the beam curvatures attained from κ_d for values of α ranging from 0.1 to 10 and β from 0 to 1, due to swelling. Dashed and solid lines are isolines of the curvature κ realized and, as it can be appreciated in the diagram, both positive and negative curvatures κ are realized. There are three highlighted isolines. One is the red dashed line corresponding to a flat beam, that is, to $\kappa = 0$: the diagram shows as there are different pairs of parameters (α, β) which realize a flat beam starting from one with curvature $\kappa_d = 50\ \mathrm{m}^{-1}$. Moreover, the dashed red line divides the diagram into a (blue) part corresponding to beams with positive curvatures and a (red) part corresponding to beams with negative curvatures. The second key isoline is the black dashed line, corresponding to $\alpha = 1$, that is, to a homogeneous beam. In this case, fixed $\bar{\mu} = 0$ we get $\kappa = 20\ \mathrm{m}^{-1}$, starting from $\kappa_d = 50\ \mathrm{m}^{-1}$ for any values of the parameter β which is no more meaningful. The third distinguished isoline is the solid red isolines corresponding to a curvature $\kappa = \kappa_d$, that is, to a curvature equal to the one characterizing the dry state of the beam. It means that, working with the pair (α, β) of parameters, we can also aim to keep unchanged beam's curvature under a change in the environment conditions. As expected, swelling gets to evert the dry curvature of the beam only when $\alpha < 1$; indeed, as the shear modulus and the free-swelling stretch of a single layer taken separately are in inverse relation through (3.9), $\alpha < 1$ ($G_i < G_e$) implies $\lambda_{oi} > \lambda_{oe}$. As a consequence, the beam-like located at the intrados swells more than the one placed on the extrados favouring the eversion. On the other hand, for $\alpha > 1$, beam curvature gets increasing for increasing values of α.

It is also interesting to view the curvature patterns from a different point of view through the diagram shown in Fig. 3 (left panel). Therein, the isolines of curvature corresponding to values of β between 0 and 1 and of κ_d between 1 and 50 m^{-1} are shown in the plane $\bar{\kappa}_d - \beta$, at $\alpha = 0.5$. This value of $\alpha < 1$ was chosen to evidence in the diagram also the eversion of the beam (as remarked above, only possible for $\alpha < 1$). In the contour plot, we identify a locus of points $(\bar{\kappa}_d, \beta)$, the red dashed isoline, where $\kappa = 0$; it divides the diagram into the red zone, always corresponding to negative curvatures from the blue zone corresponding to positive curvatures. The diagram shows as, at that values of α, there are some values of κ_d such that we can get beam eversion, that is, through swelling when the appropriate thicknesses ratio β is used. The right panel of the same figure shows the correspondence between the dimensionless curvature $\bar{\kappa}_d$ used in the left diagram and the curvature κ_d, when $h = 4$ mm, and the corresponding beam's cartoons.

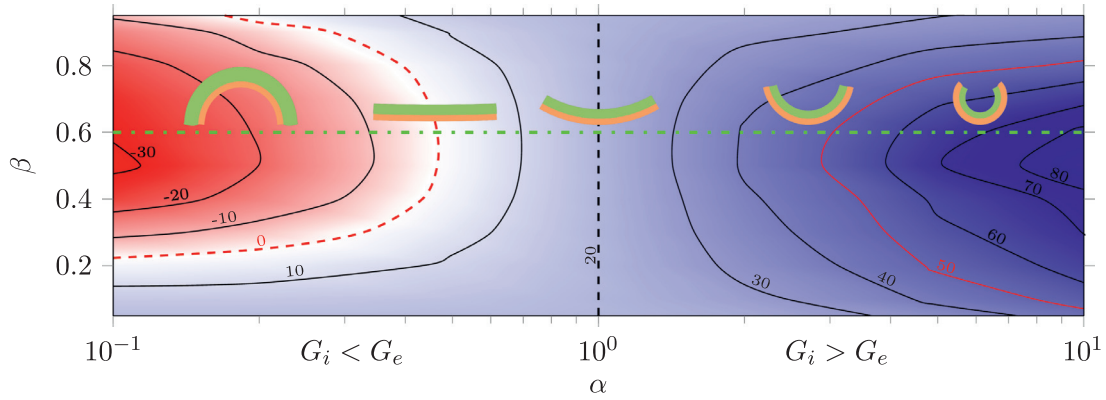

Fig. 2. Morphological phase diagram of emerging curved patterns from numerical simulations. Dashed and solid lines are isolines of the curvature κ realized by swelling a naturally curved beam with reference curvature $\kappa_d = 50\ \mathrm{m}^{-1}$. The black dashed isoline corresponds to $\alpha = 1$ ($G_i = G_e$). The red dashed isoline, belonging to the half-plane $\alpha < 1$, corresponds to the flat configuration $\kappa = 0$. The red solid isoline corresponds to $\kappa = \kappa_d$. The insets represent the deformed configuration of the beam, at different values of curvature. (For interpretation of the references to colour in this figure legend, the reader is referred to the web version of this article.)

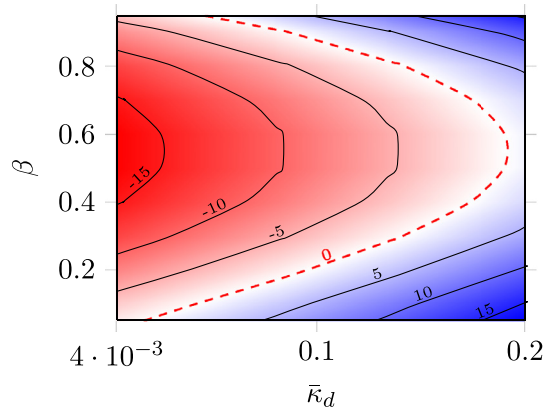

$\bar{\kappa}_d$	$\kappa_d\ [\mathrm{m}^{-1}]$	dry
$4 \cdot 10^{-3}$	1	
0.1	25	
0.2	50	

Fig. 3. Cartoon showing the beams corresponding to $\kappa_d = 1$ ($\bar{\kappa}_d = \kappa_d h = 4 \cdot 10^{-3}$), $\kappa_d = 25$ ($\bar{\kappa}_d = \kappa_d h = 0.1$), and $\kappa_d = 50$ ($\bar{\kappa}_d = \kappa_d h = 0.2$) (right). Isolines of curvature corresponding to different values of β and $\bar{\kappa}_d$ at $\alpha = 0.5$ (left).

3.2. The limit case of homogeneous beams

The homogeneous and naturally curved beam corresponds to both $\alpha = 1$ (two layers of the same material), and to $\beta = 0, 1$ (the beam coincides with the extrados or with the intrados layer, respectively). In this case, Eq. (3.9) delivers the uniform swelling ratio λ_o realized by the beam at the equilibrium and corresponding to $\bar{\mu} = 0$. So, the equilibrium state is identified by a swollen thickness $h_o = \lambda_o h$ and a swollen curvature $\kappa_o = \kappa_d/\lambda_o$. Hence, for a homogeneous beam, the swollen curvature κ_o depends linearly on the reference curvature κ_d; moreover, at $\kappa_d = 0$, swelling can't induce any curving in a homogeneous beam. The elastic energy stored along the swelling process is easily determined from (2.2) as

$$\Psi = \frac{3}{2} G h (\lambda_o^2 - 1) L w\,, \tag{3.12}$$

and, following [31], we would say that the swelling process induces a pure stretching deformation of the homogeneous beam.

When the free–swelling stretch $\lambda_o \gg 1$, the chemical equilibrium equation can be replaced by its asymptotic version. The swelling stretch is evaluated by estimating the leading order term in the asymptotic expansion up to $O(1/\lambda_o^8)$ (see [33]) as

$$\lambda_o \simeq \left(\frac{\mathcal{R}T}{\Omega} \frac{1/2 - \chi}{G} \right)^{1/5}. \tag{3.13}$$

It leads to an explicit formula for the curvature at the swollen equilibrium state in the form

$$\kappa_o \simeq \left(\frac{\Omega}{\mathcal{R}T\,(1/2 - \chi)} \right)^{1/5} G^{1/5} \kappa_d\,. \tag{3.14}$$

At different values of the reference curvature κ_d, varying from 0 to $100\mathrm{m}^{-1}$, Fig. 4 (left panel) shows the swollen curvatures κ_o corresponding to a shear modulus G varying from 1 to 150 kPa. Precisely, the triangle-based lines correspond to the exact solution of the equilibrium Eq. (3.9); the solid lines correspond to the approximate solution presented in the next section (precisely, Eq. (3.14)). Fig. 4 (right panel) shows the swollen curvatures κ_o corresponding to a reference curvature κ_d varying from 0 to 100 m^{-1} at different values of the shear modulus G (triangle-based lines and solid lines represent the same code used for the left panel). The three cartoons at the bottom of Fig. 4 correspond to beams whose curvatures are identified in the two panels by the number 1 ($\kappa_o = 0$), 2 ($\kappa_o \simeq 40\ \mathrm{m}^{-1}$), and 3 ($\kappa_o \simeq 80\ \mathrm{m}^{-1}$).

4. Explicit model for curved bilayer beams

Due to the numerical evidences of plane bending processes, we set the explicit model within a two-dimensional scenario: given the coordinate system (ζ, Θ, Z), we assume that the flexure plane $Z = 0$ is a symmetry plane (see Fig. 1). Bending deformations from the dry state to a swollen and steady state are then modeled assuming that cross-sections stay plane and curvature uniform. Under these hypotheses, each circular arc of radius $R = R_m + \zeta$, where $\zeta \in [-h/2, h/2]$, and angle amplitude $2\bar{\Theta}$ maps into another circular arc of radius r and angle amplitude $2\bar{\theta}$.

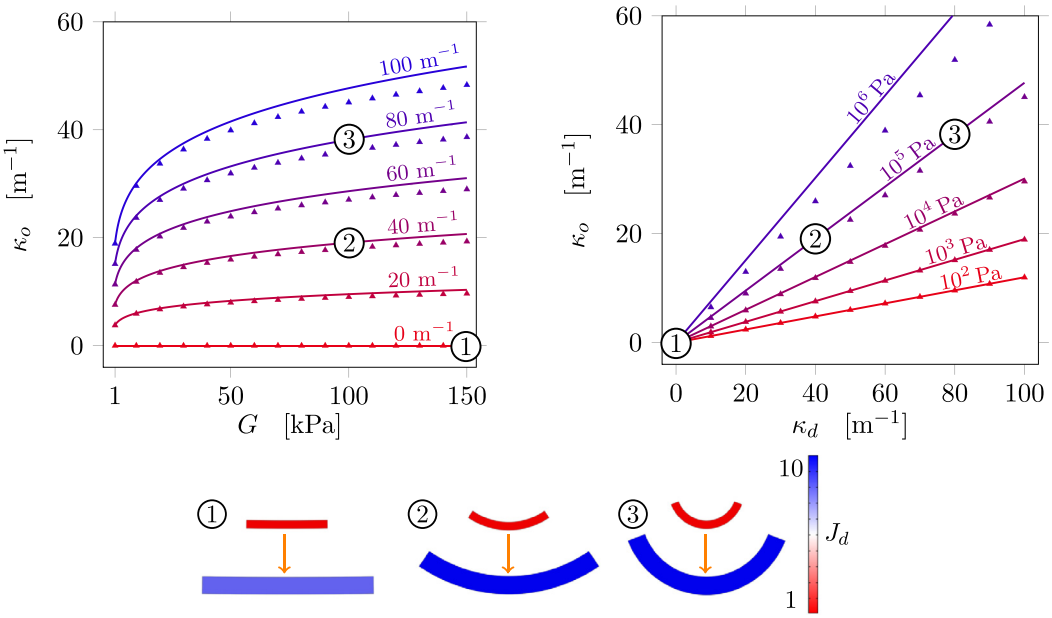

Fig. 4. Swollen curvature κ_o versus shear modulus G at different values of κ_d ranging from $\kappa_d = 0$ to $\kappa_d = 50$ m^{-1} (left) and versus dry curvature κ_d at different values of G ranging from $G = 10^2$ Pa to $G = 10^6$ Pa (right). Triangles represent the outcomes of the numerical experiments; solid lines correspond to the asymptotic approximation (3.14) (right). Cartoons of the beams whose curvatures correspond to circle 1 ($\kappa_o = 0$), 2 ($\kappa_o \simeq 40$ m^{-1}), and 3 ($\kappa_o \simeq 80$ m^{-1}) in the diagrams (bottom).

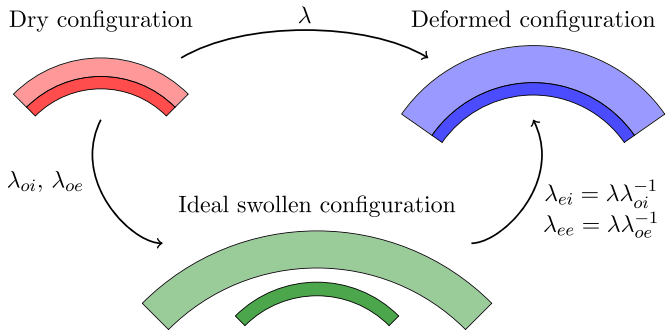

Fig. 5. Cartoon of the multiplicative decomposition of the bending deformation: if the two layers were free, one from each other, they would swell as represented in the ideal swollen configuration, which can't be realized; as they are bonded, starting from a dry configuration, swelling induces a bent deformed configuration.

With this, the measure $\lambda(\zeta)$ of the hoop deformation that takes place within the gel beam can be represented as

$$\lambda(\zeta) = (1 + \kappa_d \zeta)^{-1} (\Lambda_0 + \Lambda_1 \zeta), \quad \Lambda_1 = \kappa \Lambda_0^2, \tag{4.15}$$

where we assumed the existence of a swelling ratio Λ_0 in between λ_{oi} and λ_{oe} that determines an isotropic stretch of the beam such that: (i) $r = \Lambda_0 R$; (ii) $(\bar{\theta}/\kappa) = \Lambda_0(\bar{\Theta}/\kappa_d)$, that is, the length of the axis at the swollen state is Λ_0 times the length of the dry axis. Following the uncoupled approach proposed in [17], we assume that a multiplicative decomposition holds for the visible longitudinal (hoop) deformation λ and write it as the product of an elastic component λ_e and a distortion λ_{om} $(m = i, e)$ which is the free swelling-induced deformation that would take place in each single part if it was free from the rest of the beam (Fig. 5). With this, we write

$$\lambda = \lambda_{ei}\lambda_{oi} = \lambda_{ee}\lambda_{oe}\,, \tag{4.16}$$

with λ_{ei} and λ_{ee} the elastic deformation in the intrados and in the extrados layer, respectively, and with λ_{oi} and λ_{oe} the free-swelling deformation corresponding to each of the two layers through the chemical equilibrium Eq. (3.9) (see Fig. 5).

We assume zero out–of–plane stresses and evaluate the bending stresses σ_i and σ_e at the cross–sections of the extrados and intrados layers as

$$\sigma_i(\zeta) = 3G_i(\lambda(\zeta)\lambda_{oi}^{-1} - 1)\,, \quad -\frac{h}{2} < \zeta < -\frac{h}{2} + \beta h\,, \tag{4.17}$$

$$\sigma_e(\zeta) = 3G_e(\lambda(\zeta)\lambda_{oe}^{-1} - 1)\,, \quad -\frac{h}{2} + \beta h < \zeta < \frac{h}{2}\,, \tag{4.18}$$

where, due to the material incompressibility, $3G_i = E_i$ and $3G_e = E_e$. Under no external load and unconstrained conditions, the total force F and torque T of the longitudinal stresses have to be identically null:

$$F = w\lambda_{oi}^2 \int_{-\frac{h}{2}}^{-\frac{h}{2}+\beta h} \sigma_i(\zeta)d\zeta \; + \; w\lambda_{oe}^2 \int_{-\frac{h}{2}+\beta h}^{\frac{h}{2}} \sigma_e(\zeta)d\zeta = 0\,, \tag{4.19}$$

$$M = w\lambda_{oi}^3 \int_{-\frac{h}{2}}^{-\frac{h}{2}+\beta h} \zeta\sigma_i(\zeta)d\zeta \; + \; w\lambda_{oe}^3 \int_{-\frac{h}{2}+\beta h}^{\frac{h}{2}} \zeta\sigma_e(\zeta)d\zeta = 0\,. \tag{4.20}$$

Keeping Λ_0 and Λ_1 uniform, it yields a linear system whose solution $(\Lambda_0\,, \Lambda_1)$ can be found in the form

$$\Lambda_0 = \hat{\Lambda}_0(\alpha, \beta, \Gamma, \bar{\kappa}, \lambda_{oe}) \quad \text{and} \quad \Lambda_1 = \hat{\Lambda}_1(\alpha, \beta, \Gamma, \bar{\kappa}, h, \lambda_{oe})\,, \tag{4.21}$$

where the dimensionless parameter $\Gamma = \lambda_{oe}/\lambda_{oi}$ has been introduced. With this, the beam axis curvature can be evaluated as

$$\kappa = \frac{\Lambda_1}{\Lambda_0^2} = \hat{\kappa}(\alpha, \beta, \Gamma, \bar{\kappa}, h, \lambda_{oe})\,. \tag{4.22}$$

The representation of the functions $\hat{\Lambda}_0(\alpha, \beta, \Gamma, \bar{\kappa}, \lambda_{oe})$ and $\hat{\Lambda}_1(\alpha, \beta, \Gamma, \bar{\kappa}, h, \lambda_{oe})$ is heavy, and has been reported in Appendix A; nevertheless, they allow to deliver explicitly beam stretch and curvature.

Up to now, λ_{oi} and λ_{oe} in the Eq. (4.21) are just distortions, that is, generic inelastic deformations such as thermal distortions or growth-induced deformations, as the equations which assign to λ_{oi} and λ_{oe} the role of swelling elastic deformations, that is, the chemical equilibrium conditions, haven't been used, yet. It means that, Eq. (4.22) delivers the axis's curvature induced in a bilayered beam by any stimulus whose effect can be taken into account into λ_{oe} and λ_{oi}, as does Timoshenko's formula for curved bimetal strips [32]. The difference between the twos

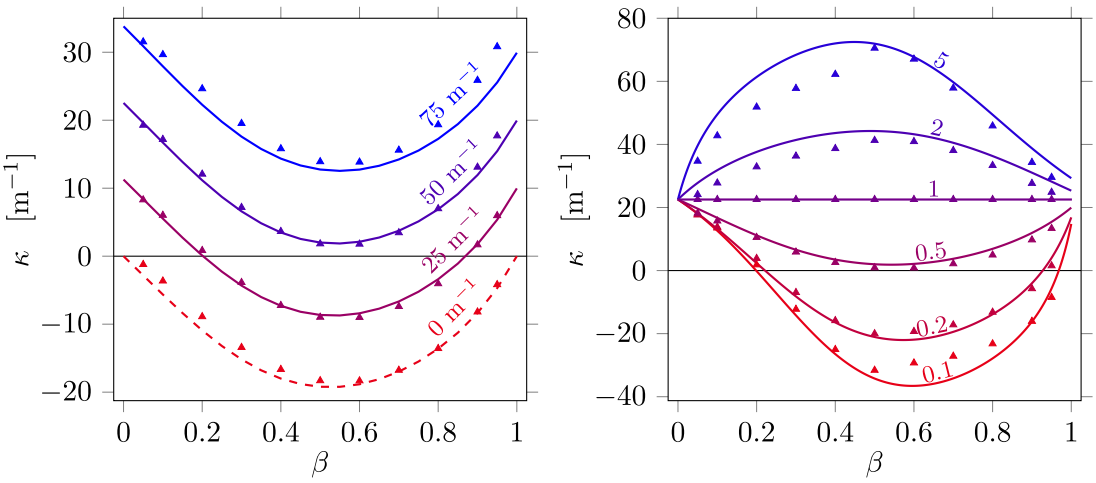

Fig. 6. Curvature κ versus thickness ratio β at $\alpha = 0.5$ and different values of $\kappa_d = 0, 25, 50, 75\text{m}^{-1}$ (left panel) and at $\kappa_d = 50$ m^{-1} and different values of $\alpha = 0.1, 0.2, 0.5, 1, 2, 5$ (right panel). Solid lines and triangles correspond to explicit and numerical results, respectively.

being the validity regime: small deformations and small reference curvature κ_d for Timoshenko's formula, finite deformations for Eq. (4.22), as we are discussing in the last section.

For gel beams under swelling, the chemical equilibrium conditions require that the pairs $(G_e,\ \lambda_{oe})$ and $(G_i,\ \lambda_{oi})$ have to satisfy the following equations, which identify the deformations λ_{oi} and λ_{oe} as the free swelling-induced deformations that would take place in each single part if it was free from the rest of the beam:

$$\frac{G_i\Omega}{\lambda_{oi}} + \mathcal{R}T\left(\log\frac{\lambda_{oi}^3-1}{\lambda_{oi}^3} - \frac{1}{\lambda_{oi}^3} + \frac{\chi}{\lambda_{oi}^6}\right) = \bar{\mu}\,, \tag{4.23}$$

$$\frac{G_e\Omega}{\lambda_{oe}} + \mathcal{R}T\left(\log\frac{\lambda_{oe}^3-1}{\lambda_{oe}^3} - \frac{1}{\lambda_{oe}^3} + \frac{\chi}{\lambda_{oe}^6}\right) = \bar{\mu}\,. \tag{4.24}$$

5. Results and discussion

Eqs. (4.21) and (4.22), together with Eqs. (A.2)–(A.4), allow to evaluate beam's curvature, once assigned the chemical potential $\bar{\mu}$ of the bath and the shear moduli of the two layers in terms of the thicknesses ratio β at any values of the ratio α between the shear moduli and of the curvature κ_d of the beam's axis at the dry state. Fig. 6 (left panel) shows the realized curvature κ at different values of κ_d, from 0 to 75 m^{-1}, at $\alpha = 0.5$. The same figure (right panel) shows the realized curvature κ at different values of α, from 0.1 to 5, at $\kappa_d = 50$ m^{-1}. Solid lines come from the approximate explicit formulas (4.21) and (4.22), whereas triangle-based lines are the corresponding outcomes from the fully three-dimensional nonlinear stress-diffusion model.

5.1. Curved monolayer beams

The values of the stretch Λ_o and the curvature κ for a monolayer curved beam are easily recovered by setting $\beta = 0$ or $\beta = 1$ as well as $\alpha = 1$. From Eqs. (4.21)$_1$ and (4.22), we get: for $\beta = 0$, that is, when the monolayer collapses on the extrados layer,

$$\kappa = \kappa_o = \frac{\kappa_d}{\lambda_{oe}} \quad \text{and} \quad \Lambda_0 = \lambda_{oe}\,; \tag{5.25}$$

on the other hand, for $\beta = 1$, that is, when the monolayer collapses on the intrados layer, we get

$$\kappa = \kappa_o = \frac{\kappa_d}{\lambda_{oi}} \quad \text{and} \quad \Lambda_0 = \lambda_{oi}\,. \tag{5.26}$$

As expected, the steady swollen state is a homothety of the dry configuration; the amount of dilation is controlled by $\bar{\mu}$ through Eqs. (4.23) and (4.24). The two panels of Fig. 4 showed the swollen curvature κ_o versus the shear modulus G at different values of the reference curvature κ_d, varying from 0 to 100 m^{-1}, as well as κ_o versus the dry curvature κ_d at different values of the shear modulus G, varying from 1 to 150 kPa. The agreement between the full and the approximated curvature, especially for low values of G and κ_d, is very good.

5.2. Flat bilayer beams

The limit case corresponding to flat bilayer beams can be recovered from Eqs. (4.21)$_1$ and (4.22) as limits for $\kappa_d \to 0$. We get:

$$\begin{aligned}\Lambda_0^{\text{flat}} &= \lim_{\bar{\kappa}\to 0}\hat{\Lambda}_0(\alpha,\beta,\Gamma,\bar{\kappa},\lambda_{oe}) = \hat{\Lambda}_0(\alpha,\beta,\Gamma,\lambda_{oe})\\ &= \frac{f(\alpha,\beta,\Gamma)}{g(\alpha,\beta,\Gamma)}\,\lambda_{oe}\,,\end{aligned} \tag{5.27}$$

$$\begin{aligned}\kappa^{\text{flat}} &= \lim_{\bar{\kappa}\to 0}\hat{\kappa}(\alpha,\beta,\Gamma,\bar{\kappa},h,\lambda_{oe}) = \hat{\kappa}(\alpha,\beta,\Gamma,h,\lambda_{oe})\\ &= -\frac{6\alpha\beta\Gamma(\beta-1)(\Gamma-1)(\beta(\Gamma-1)+1)\,g(\alpha,\beta,\Gamma)}{f(\alpha,\beta,\Gamma)^2}\,\frac{1}{h\lambda_{oe}}\,,\end{aligned} \tag{5.28}$$

with

$$\begin{aligned}f(\alpha,\beta,\Gamma) = {}& \alpha^2\beta^4 + \alpha(\beta-1)\beta\Gamma\big(\beta^2\big(3\Gamma^2-8\Gamma+3\big)\\ &+ \beta\big(-3\Gamma^2+8\Gamma-3\big) - 4\Gamma\big) + (\beta-1)^4\Gamma^4,\end{aligned} \tag{5.29}$$

$$\begin{aligned}g(\alpha,\beta,\Gamma) = {}& \Gamma\big(\alpha^2\beta^4 - \alpha\beta(\beta-1)\Gamma\big(\beta^2(\Gamma+1)+\beta(\Gamma-3)+\Gamma+3\big)\big)\\ &+ (\beta-1)^4\Gamma^4.\end{aligned} \tag{5.30}$$

The functions $\hat{\Lambda}_0(\alpha,\beta,\Gamma,\lambda_{oe})$ and $\hat{\kappa}(\alpha,\beta,\Gamma,h,\lambda_{oe})$ are the same as the ones derived and presented in [17], where the problem has been dealt for flat bilayer beams.

5.3. Nearly-homogeneous beams

We can also consider a nearly-homogeneous bilayer curved beam, that is, with shear moduli G_e and $G_i = G_e + \Delta$, with $\Delta/G_e -> 0$. In this case, the ratio between the shear moduli can be rewritten as

$$\alpha = 1 + \varepsilon\,, \quad \varepsilon = \frac{\Delta}{G_e}\,, \tag{5.31}$$

and the previous results can be approximated up to $o(\varepsilon)$. Using (3.13), the ratio between the free swelling deformations λ_{oe} and λ_{oi} can be approximated for $\varepsilon \to 0$ as

$$\Gamma = \frac{\lambda_{oe}}{\lambda_{oi}} = (1+\varepsilon)^{1/5} \simeq 1 + \frac{1}{5}\varepsilon\,. \tag{5.32}$$

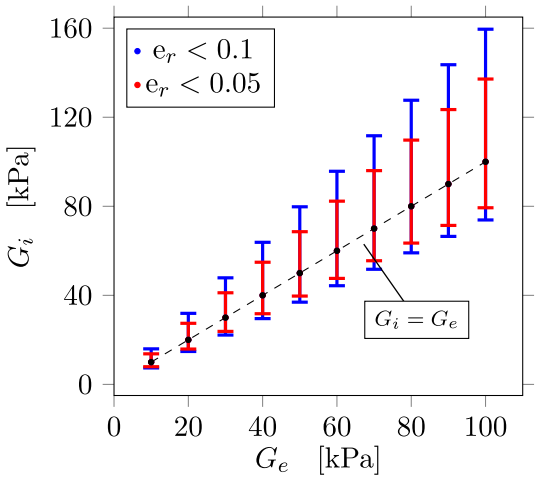

Fig. 7. Error bar diagram in the plane $G_i - G_e$. Error bars represent the range of G_i, corresponding to a certain value of G_e, within which the relative error e_r between the curvatures κ and κ_{n-h} is less than 10% (blue) or 5% (red). The black dashed line corresponds to $G_i = G_e$. (For interpretation of the references to colour in this figure legend, the reader is referred to the web version of this article.)

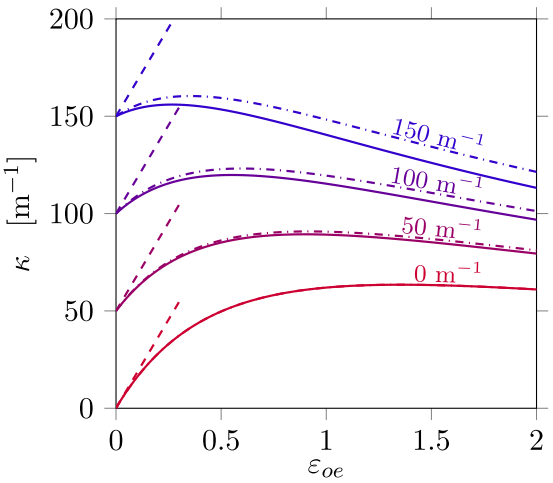

Fig. 8. Curvature κ versus ε_{oe} at $\alpha = 2$, $\beta = 0.5$, $\gamma = 2$, $h = 4$ mm and different values of κ_d. Solid lines correspond to the Eq. (4.22); dashed lines to Timoshenko's linear model (5.36); and the dash-dotted lines to the additive nonlinear Eq. (5.37). Different colours correspond to different dry beam's curvature.

From Eqs. (5.31) and (5.32), by expanding the Eq. (4.22) as a power series around $\varepsilon = 0$ at the first order in ε, we get the following additive formula for $\kappa = \kappa_{n-h}$:

$$\kappa_{n-h} = \frac{\kappa_d}{\lambda_{oe}} + \frac{\beta\bar{\kappa}_d\left(2\bar{\kappa}_d(\beta\bar{\kappa}_d - \bar{\kappa}_d + 1) + (\beta\bar{\kappa}_d - \bar{\kappa} + 2)\log\left(\frac{2-\bar{\kappa}_d}{2+\bar{\kappa}_d}\right)\right)}{10\ h\left(\bar{\kappa}_d + \log\left(\frac{2-\bar{\kappa}_d}{2+\bar{\kappa}_d}\right)\right)}\frac{1}{\lambda_{oe}}\varepsilon\,. \tag{5.33}$$

For $\varepsilon = 0$, that is, $\Delta = 0$, only the first addend survives and the curvature of a homogeneous beam (5.25) is recovered. The above additive formula is much simpler than the original one and we may ask which are the limits of its validity, that is, how much a bilayer beam can be far from being homogeneous to be considered nearly-homogeneous, in such a way that its swelling-induced increase/decrease in curvature can be dictated by the Eq. (5.33). In general, for $\varepsilon \neq 0$, the relative error between formulas (4.22) and (5.33) can be estimated as

$$e_r = \left|\frac{\kappa - \kappa_{n-h}}{\kappa}\right|. \tag{5.34}$$

Then, we can fix an acceptable value δ_e of the error limit and evaluate, for any values of G_e, the range of G_i such that $e_r < \delta_e$. Fig. 7 show the validity ranges corresponding to G_e from 0 to 100 kPa and $\delta_e = 0.1, 0.05$. Precisely, the error bars corresponding to $\delta_e = 0.1$ ($\delta_e = 0.05$) are shown as blue (red) bars. The black dashed lines corresponds to $G_i = G_e$ that is, to a perfectly homogeneous beam.

5.4. Additive decomposition of the curvature

Finally, we like to highlight the differences between our formulas, given by the Eqs. $(4.21)_1$ and (4.22), and other additive formulas proposed in the Literature.

Let us start with the noteworthy contribution presented in [32], where an additive formula for the curvature κ of naturally curved bilayer beams undergoing thermal strains is provided, under the hypotheses of small (thermal and elastic) strains and small initial curvature. Our curvature formula (4.22), holding for generic distortions λ_{oi} and λ_{oe}, can be evaluate in the case of slightly curved bilayer beams, that is, for $\bar{\kappa}_d \to 0$. Moreover, introduced the small distortions $\varepsilon_{oe} = \lambda_{oe} - 1$ and $\varepsilon_{oi} = \lambda_{oi} - 1$, and set $\gamma = \varepsilon_{oi}/\varepsilon_{oe}$ (see also [20]), we can write

$$\Gamma = (1 + \varepsilon_{oe})/(1 + \varepsilon_{oe}/\gamma)\,. \tag{5.35}$$

Introduced Timoshenko's notation, that is, setting $\alpha = n$ and $\beta = m/(1 + m)$, where $m = h_i/h_e$, and expanding the Eq. (4.22) as a power series around $\varepsilon_{oe} = 0$ and $\kappa_d = 0$, we get, at the first order in κ_d and ε_{oe},

$$\kappa = \kappa_d + \frac{6mn(m+1)^2}{h\left(m^4n^2 + 4m^3n + 6m^2n + 4mn + 1\right)}\left(\varepsilon_{oe} - \varepsilon_{oi}\right), \tag{5.36}$$

which is the Timoshenko's formula for slightly naturally curved bimetal beams. It delivers the curvature κ as an additive decomposition into the reference curvature κ_d and another term which correspond to the linear Timoshenko's formula for the curvature of bilayer straight beams. It corresponds to the straight dashed lines in Fig. 8, where κ is represented versus ε_{oe} at $\alpha = 2$, $\beta = 0.5$, $\gamma = 2$, and $h = 4$ mm, for different values of κ_d, corresponding to the different colours of the lines.

It is worth noting that a different additive formula for the curvature κ of naturally curved bilayer beams can be written from Eqs. (5.27) and (5.28) as

$$\kappa = \frac{\kappa_d}{\Lambda_0^{\text{flat}}} + \kappa^{\text{flat}}, \tag{5.37}$$

where Λ_0^{flat} and κ^{flat} are the axis stretching and curvature of a straight bilayer beam with the same geometrical and material structure of the naturally curved beam (see also [34]). In this case, we get the dash-dotted lines shown in Fig. 8, together with the solid lines representing the curvature as delivered by our Eq. (4.22). It is worth noting that, as well known, Timoshenko's equation is linear both in κ_d and ε_{oe} and tends to coincide with the tangent of our equation in $\varepsilon_{oe} = 0$ for low values of κ_d. On the other hand, he additive formula (5.37), that is linear in κ_d and nonlinear in ε_{oe}, is closer and closer to the formula (4.22) for small ε_{oe} and low values of κ_d. In particular, for $\kappa_d = 0$, (5.37) and (4.22) agree; whereas, for high values of κ_d it overestimates beam curvature with respect to the estimation given by Eq. (5.37), which on its turn, slightly overestimates the solution delivered from the numerical implementation of the fully coupled three-dimensional nonlinear model of stress-diffusion originally presented in [21].

6. Conclusions and future directions

The swelling-induced eversion and flattening of bilayer gel beams has been discussed through exact numerical models and approximate explicit formulas. A good agreement of the two approaches in terms of the expected final curvature has been found. Our results show that eversion and flattening of an initial curved beam can be realized for specific

ratios of thicknesses and elastic moduli of the two homogeneous layers. They are independent on the original curvature and include the Timoshenko formula for bilayer thermal beams within the limits of slightly curvature of the original dry beam and small deformations [32], and an additive-type formula like the one derived in [34]

The explicit formulas that predict the final shape of naturally curved bilayer gel beams provide a step forward into the understanding of the key design principles and modeling tools for swelling of curved gel beams. These structures can be employed in encapsulation and delivery of drugs, medical intervention, scaffolding materials for three–dimensional cell culture, soft robots, sensing and actuation, due to properties of hydrogels such as high-swelling, biocompatibility, biodegradability, and stimuli response. Hence, the availability of explicit formulas which deliver a correct value of the change in curvature under swelling is highly valuable and still missing.

In the next future, the same approach will be implemented to analyze the change in curvature due to de-swelling produced by different techniques, as shown in [14].

Acknowledgments

The work is supported by MIUR (the Italian Ministry of University and Research) through the Project PRIN2017 (N. 2017KL4EF3) Mathematics of active materials from mechanobiology to smart devices. The Authors also acknowledge the financial supports from Sapienza Università di Roma (Grant. N. RG11715C7CE2C1C4).

Appendix A. Explicit representation of beams's stretch and curvature

Solving the Eqs. (4.19) and (4.20), we get

$$\Lambda_0 = \hat{\Lambda}_0(\alpha,\beta,\Gamma,\bar{\kappa},\lambda_{oe}) \quad \text{and} \quad \Lambda_1 = \hat{\Lambda}_1(\alpha,\beta,\Gamma,\bar{\kappa},h,\lambda_{oe}), \tag{A.1}$$

with $\Gamma = \lambda_{oe}/\lambda_{oi}$. The explicit representation of the two quantities is:

$$\Lambda_0 = \frac{a\,\log(2-\bar{\kappa}_d) + b\,\log(\bar{\kappa}_d+2) + c\,\log(2\beta\bar{\kappa}_d - \bar{\kappa}_d + 2) + d + e}{a'\,\log(2-\bar{\kappa}_d) + b'\,\log(\bar{\kappa}_d+2) + c'\,\log(2\beta\bar{\kappa}_d - \bar{\kappa}_d + 2) + d'}\,\lambda_{oe}, \tag{A.2}$$

$$\Lambda_1 = \frac{a\,\log(2-\bar{\kappa}_d) + b\,\log(\bar{\kappa}_d+2) + c\,\log(2\beta\bar{\kappa}_d - \bar{\kappa}_d + 2) + d}{a'\,\log(2-\bar{\kappa}_d) + b'\,\log(\bar{\kappa}_d+2) + c'\,\log(2\beta\bar{\kappa}_d - \bar{\kappa}_d + 2) + d'}\,\frac{\bar{\kappa}_d}{h}\,\lambda_{oe}, \tag{A.3}$$

where

$$\begin{aligned}
a &= \hat{a}(\alpha,\beta,\Gamma,\bar{\kappa}_d) = \alpha\big(\alpha\beta((\beta-1)\bar{\kappa}_d+2) - (\beta-1)\Gamma^2(\beta\Gamma\bar{\kappa}_d+2)\big),\\
b &= \hat{b}(\alpha,\beta,\Gamma,\bar{\kappa}_d) = \Gamma\big(\alpha\beta(-\beta\bar{\kappa}_d - 2\Gamma + \bar{\kappa}_d) + (\beta-1)\Gamma^3(\beta\bar{\kappa}_d+2)\big),\\
c &= \hat{c}(\alpha,\beta,\Gamma,\bar{\kappa}_d) = (\beta-1)\beta\bar{\kappa}_d(\Gamma-\alpha)\big(\alpha-\Gamma^3\big) - 2\big(\alpha-\Gamma^2\big)\big(\alpha\beta-(\beta-1)\Gamma^2\big),\\
d &= \hat{d}(\alpha,\beta,\Gamma,\bar{\kappa}_d) = 2\bar{\kappa}_d\big(\alpha\beta-(\beta-1)\Gamma^2\big)^2,\\
e &= \hat{e}(\alpha,\beta,\Gamma,\bar{\kappa}_d) = -\alpha(\beta-1)\beta(\Gamma-1)\Gamma\bar{\kappa}_d^2(\beta(\Gamma-1)+1),\\
a' &= \hat{a}'(\alpha,\beta,\Gamma,\bar{\kappa}_d) = -\Gamma\alpha(\alpha\beta(-\beta\bar{\kappa}_d+\bar{\kappa}_d-2) + (\beta-1)\Gamma(\beta\Gamma\bar{\kappa}_d+2)),\\
b' &= \hat{b}'(\alpha,\beta,\Gamma,\bar{\kappa}_d) = -\Gamma^2\big(\alpha\beta((\beta-1)\bar{\kappa}_d+2\Gamma) - (\beta-1)\Gamma^2(\beta\bar{\kappa}_d+2)\big),\\
c' &= \hat{c}'(\alpha,\beta,\Gamma,\bar{\kappa}_d) = -\Gamma\big(\alpha-\Gamma^2\big)(\beta(\alpha-\Gamma)((\beta-1)\bar{\kappa}_d+2)+2\Gamma),\\
d' &= \hat{d}'(\alpha,\beta,\Gamma,\bar{\kappa}_d) = 2\Gamma\bar{\kappa}_d(\alpha\beta-\beta\Gamma+\Gamma)\big(\alpha\beta-(\beta-1)\Gamma^2\big).
\end{aligned} \tag{A.4}$$

Even if the two formulas look cumbersome, nevertheless they allow an explicit evaluation of the beam's stretch Λ_o and beam's curvature $\kappa = \Lambda_1/\Lambda_o$.

References

[1] Osada Y, Gong JP. Soft and wet materials: polymer gels. Adv Mater 1998;10(11):827–37. doi:10.1002/(SICI)1521-4095(199808)10:11<827::AID-ADMA827>3.0.CO;2-L.
[2] Lee Y-J, Braun P. pH Tunable inverse opal hydrogel ph sensors. Adv Mater 2003;15(7–8):563–6. doi:10.1002/adma.200304588.
[3] Warner M, Mahadevan L. Photoinduced deformations of beams, plates, and films. Phys Rev Lett 2004;92:134302. doi:10.1103/PhysRevLett.92.134302.
[4] Marcombe R, Cai S, Hong W, Zhao X, Lapusta Y, Suo Z. pHA theory of constrained swelling of a ph-sensitive hydrogel. Soft Matter 2010;6:784–93. doi:10.1039/B917211D.
[5] Wang E, Desai MS, Lee SW. Light-controlled graphene-elastin composite hydrogel actuators. Nano Lett 2013;13(6):2826–30. doi:10.1021/nl401088b. PMID: 23647361
[6] Ma C, Lu W, Yang X, He J, Le X, Wang L, Zhang J, Serpe MJ, Huang Y, Chen T. Bioinspired anisotropic hydrogel actuators with on-off switchable and color-tunable fluorescence behaviors. Adv Funct Mater 2018;28(7):1704568. doi:10.1002/adfm.201704568.
[7] Jiang H, Fan L, Yan S, Li F, Li H, Tang J. Tough and electro-responsive hydrogel actuators with bidirectional bending behavior. Nanoscale 2019;11:2231–7. doi:10.1039/C8NR07863G.
[8] Hu L, Zhang Q, Li X, Serpe MJ. Stimuli-responsive polymers for sensing and actuation. Mater Horiz 2019. doi:10.1039/C9MH00490D.
[9] Banerjee H, Suhail M, Ren H. Hydrogel actuators and sensors for biomedical soft robots: brief overview with impending challenges. Biomimetics 2018;3:15. doi:10.3390/biomimetics3030015.
[10] Kim J, Hanna JA, Byun M, Santangelo CD, Hayward RC. Designing responsive buckled surfaces by halftone gel lithography. Science 2012;335(6073):1201–5. doi:10.1126/science.1215309.
[11] Wu ZL, Moshe M, Greener J, Therien-Aubin H, Nie Z, Sharon E, Kumacheva E. Three-dimensional shape transformations of hydrogel sheets induced by small-scale modulation of internal stresses. Nat Commun 2013;4:1586. doi:10.1038/ncomms2549.
[12] Morimoto T, Ashida F. Temperature-responsive bending of a bilayer gel. Int J Solids Struct 2015;56–57:20–8. doi:10.1016/j.ijsolstr.2014.12.009.
[13] Pezzulla M, Smith GP, Nardinocchi P, Holmes DP. Geometry and mechanics of thin growing bilayers. Soft Matter 2016;12:4435–42. doi:10.1039/C6SM00246C.
[14] Egunov AI, Korvink JG, Luchnikov VA. Polydimethylsiloxane bilayer films with an embedded spontaneous curvature. Soft Matter 2016;12:45–52. doi:10.1039/C5SM01139F.
[15] Kim J, Kim C, Song Y, Jeong S-G, Kim T-S, Lee CS. Reversible self-bending soft hydrogel microstructures with mechanically optimized designs. Chem Eng J 2017;321:384–93. doi:10.1016/j.cej.2017.03.125.
[16] Nojoomi A, Arslan H, Lee K, Yum K. Bioinspired 3d structures with programmable morphologies and motions. In: Nature communications; 2018. p. 3705.
[17] Lucantonio A, Nardinocchi P, Pezzulla M. Swelling-induced and controlled curving in layered gel beams. Proc R Soc A 2014;470(2171). doi:10.1098/rspa.2014.0467.
[18] Nardinocchi P, Puntel E. Finite bending solutions for layered gel beams. Int J Solids Struct 2016;90:228–35. doi:10.1016/j.ijsolstr.2016.02.026.
[19] Nardinocchi P, Puntel E. Finite bending solutions for layered gel beams. Int J Solids Struct 2016;90:228–35. doi:10.1016/j.ijsolstr.2016.02.026.
[20] Nardinocchi P, Puntel E. Unexpected hardening effects in bilayered gel beams. Meccanica 2017;52(14):3471–80. doi:10.1007/s11012-017-0635-z.
[21] Lucantonio A, Nardinocchi P, Teresi L. Transient analysis of swelling-induced large deformations in polymer gels. J Mech Phys Solids 2013;61(1):205–18. doi:10.1016/j.jmps.2012.07.010.
[22] Lucantonio A, Roche M, Nardinocchi P, Stone HA. Buckling dynamics of a solvent-stimulated stretched elastomeric sheet. Soft Matter 2014;10:2800–4. doi:10.1039/C3SM52941J.
[23] Nardinocchi P, Pezzulla M, Teresi L. Anisotropic swelling of thin gel sheets. Soft Matter 2015;11:1492–9. doi:10.1039/C4SM02485K.
[24] Nardinocchi P, Pezzulla M, Teresi L. Steady and transient analysis of anisotropic swelling in fibered gels. J Appl Phys 2015;118(24). doi:10.1063/1.4938737.
[25] Curatolo M, Nardinocchi P, Puntel E, Teresi L. Transient instabilities in the swelling dynamics of a hydrogel sphere. J Appl Phys 2017;122(14):145109. doi:10.1063/1.5007229.
[26] Curatolo M, Nardinocchi P. Swelling-induced bending and pumping in homogeneous thin sheets. J Appl Phys 2018;124(8):085108. doi:10.1063/1.5043580.
[27] Curatolo M, Nardinocchi P, Teresi L. Driving water cavitation in a hydrogel cavity. Soft Matter 2018;14:2310–21. doi:10.1039/C8SM00100F.
[28] Hong W, Zhao X, Zhou J, Suo Z. A theory of coupled diffusion and large deformation in polymeric gels. J Mech Phys Solids 2008;56(5):1779–93. doi:10.1016/j.jmps.2007.11.010.
[29] Dai S, Ravi P, Tam KC. Thermo- and photo-responsive polymeric systems. Soft Matter 2009;5:2513–33. doi:10.1039/B820044K.
[30] Chester SA. A constitutive model for coupled fluid permeation and large viscoelastic deformation in polymeric gels. Soft Matter 2012;8:8223–33. doi:10.1039/C2SM25372K.
[31] Wood HG, Hanna JA. Contrasting bending energies from bulk elastic theories. Soft Matter 2019;15:2411–17. doi:10.1039/C8SM02297F.
[32] Timoshenko S. Analysis of bimetal thermostats. JOSA 1925;11:233–55.
[33] Lucantonio A, Nardinocchi P, Stone HA. Swelling dynamics of a thin elastomeric sheet under uniaxial pre-stretch. J Appl Phys 2014;115(8). doi:10.1063/1.4866576.
[34] Pezzulla M, Stoop N, Jiang X, Holmes DP. Curvature-driven morphing of non-euclidean shells. Proc R Soc A 2017;473(2201):20170087. doi:10.1098/rspa.2017.0087.

The switching from computational analysis to explicit formulas takes place through the introduction of appropriate approximations. As for flat bilayer beams, the linear model presented by Timoshenko in 1925 [87] is well known. Although he refers to the specific case of a bimetallic thermostat, the formula he derives for the curvature fits whatever the nature of the growth, as long as the deformations remain small. A reduced non-linear model of flat bilayer beam in plane bending has been proposed in [47]. Explicit formulas are provided for the curvature and the longitudinal axis stretch, both assumed uniform, of layered gel beams when they absorb solvent differentially in the layers. It is assumed plane bending, flat cross–sections and uniform curvatures. It is also assumed that the visible longitudinal deformation can be multiplicatively split into the uniform free-swelling stretch that would take place if each layer was free from the rest of the beam and a further elastic component. The uniform free–swelling components of each part are determined from the appropriate mechano–chemical equilibrium equations which can be written within the Flory–Rehner stress–diffusion model in terms of the shear modulus, the chemical potential of the bath, and the Flory parameter. The strong hypothesis here introduced is to imagine that the two layers absorb the solvent separately, and that they become impermeable once glued to each other. The reduced model works in the case of plane bending, as the comparison with the full 3D numerical model shows; however, the validity for different deformation modes, such as torsion, should be investigated.

In III the aim is to build a reduced model, based on the approximations described above, for a curved bilayer beam with uniform curvature κ_d. The visible hoop deformation is represented by (3.2.31). The elastic deformation λ_e comes out from a multiplicative decomposition such that $\lambda_e = \lambda\lambda_o^{-1}$, where λ_o is the inelastic stretch (see Figure III-5). Being such distortion discontinuous, it cannot be realized and the beam cannot be stress-free. In absence of external forces the elastic deformations deliver internal stresses within the gel beam corresponding to null forces and torques on each cross-section:

$$0 = F = w\lambda_{oe}^2 \int_{-\frac{h}{2}}^{-\frac{h}{2}+\beta h} \sigma_e(\zeta)d\zeta + w\lambda_{oi}^2 \int_{-\frac{h}{2}+\beta h}^{\frac{h}{2}} \sigma_i(\zeta)d\zeta\,, \tag{4.5.60}$$

$$0 = M = w\lambda_{oe}^2 \int_{-\frac{h}{2}}^{-\frac{h}{2}+\beta h} \zeta\sigma_e(\zeta)d\zeta + w\lambda_{oi}^2 \int_{-\frac{h}{2}+\beta h}^{\frac{h}{2}} \zeta\sigma_i(\zeta)d\zeta\,, \tag{4.5.61}$$

where σ_i and σ_e are the bending stresses at the cross-section, λ_{oi} and λ_{oe} are the free swelling deformation (the subscripts i and e indicate the intrados and extrados, respectively). The system of equations

(4.5.60) and (4.5.61) provide the curvature κ and the axis stretch Λ_0 once a constitutive equation for σ_i and σ_e is introduced.
The formulas obtained for κ and Λ_0 depend on geometrical parameters such as the beam thickness, the layer thicknesses and the initial curvature, as well as on the shear moduli of the two layers, and on the natural longitudinal deformations λ_{oi} and λ_{oe}. The latter are mere inelastic deformations, such as thermal distortions, unless the chemical equilibrium conditions are introduced, which make λ_{oi} and λ_{oe} assume the role of swelling elastic deformations. Even if the two formulas III-A.2 and III-A.3 look cumbersome, nevertheless they allow an explicit evaluation of the beam stretch and curvature even for large deformations. As shown in figure III-6 there is a good agreement between the full 3D stress-diffusion model and the approximate explicit formulas. Limit cases corresponding to nearly homogeneous gel beams and nearly flat beams are identified and discussed. The Timoshenko additive formula for slightly naturally curved bimetal beams [87] is also recovered within the limits of a slight curvature in the original dry beam and small deformations.
As shown in Section 3.2, the same system of equations (4.5.60) and (4.5.61) can be obtained from the Biot elastic energy (3.2.33) as $F = \partial\mathcal{U}^B/\partial\Lambda_0 = 0$ and $M = \partial\mathcal{U}^B/\partial\Lambda_1 = 0$; hence, the couple (Λ_0, Λ_1) is found as solution of the minimization of $\mathcal{U}^B$.

4.6 EVERSION AND FLATTENING UNDER SHRINKING

The good agreement between numerical and explicit results for swelling curved gel beams suggests testing the same reduced model for shrinking gel beams, that is, when the solvent comes out from the polymer. In III the bending of curved beams has always occurred, starting from a (compatible) dry configuration, through a differential increase in the volume of the two layers due to the absorption of solvent. Considering such wet configuration as the starting point, the morphing process can be inverted reversibly by favoring the escape of liquid from the polymer network, for example by acting on the chemical potential of the bath in which the body is immersed, and recovering the dry configuration. In the latter case the reference wet configuration is not stress-free, due to the incompatibility between the layers. However, to make the explicit formulas for axial curvature and stretching valid the reference configuration must be compatible. For this purpose, an experiment that allows to validate the reduced model of bilayer curved beams in case of shrinking is set up. The beams consist of one layer made of polydimethylsiloxane (PDMS) and one layer made of PDMS mixed with silicone oil. The aim of the experiment is inducing bending through extraction of the silicone oil, that is, through shrinking of just one of the two layers. Specifically, it is decided to place the oil in the outer layer in such a way as to investigate flattening and eversion

following its extraction. The manufacturing process, described in I and [21], ensures that the reference configuration, i.e. the beam before oil extraction, is stress-free. It is assumed that the natural deformations λ_{oi} and λ_{oe} are determined by the bulk contraction due to oil extraction from the bilayer PDMS beam. Since the oil is contained in only one layer, it is set $\lambda_{oi} = 1$ for the PDMS layer, considered as a passive layer. On the other hand, assuming all the oil is extracted from the external layer, it is set

$$\lambda_{oe} = (1 - f)^{1/3}, \tag{4.6.62}$$

being f the oil fraction defined as the ratio between the amount of oil and the total volume of the layer containing the oil. The samples are made for different oil fractions; the extraction of the latter from the external layer induces significant deformations in the beam, which produce beam flattening and eversion. The plot in Figure I-3 shows a good correspondence of the experimental results with the analytical model.
From equation (3.3.38) and (4.6.62), setting $\alpha = 1$, a formula for the fraction of oil $f^\star$ needed to flatten a PDMS beam of assigned $\bar{\kappa}_d$ can be derived:

$$f^\star = 1 - \left(\frac{3 - \bar{\kappa}_d}{3 + \bar{\kappa}_d}\right)^3, \tag{4.6.63}$$

which provides the value $f^\star = 0.33$ measured experimentally for $\bar{\kappa}_d = 0.2$.

Extreme Mechanics Letters 36 (2020) 100655

Contents lists available at ScienceDirect

Extreme Mechanics Letters

journal homepage: www.elsevier.com/locate/eml

Shape-shifting of polymer beams and shells due to oil extraction

Daniele Battista [a,*], Valeriy Luchnikov [b], Paola Nardinocchi [a]

[a] Dipartimento di Ingegneria Strutturale e Geotecnica Sapienza Università di Roma, I-00184 Roma, Italy
[b] Institut de Science des Matériaux de Mulhouse 15 rue Jean Starcky Mulhouse, FR 68057, France

ARTICLE INFO

Article history:
Received 29 November 2019
Received in revised form 19 February 2020
Accepted 23 February 2020
Available online 2 March 2020

Keywords:
Shape-morphing
Bilayer beams
Cylindrical shells
Oil extraction

ABSTRACT

We investigate the morphing of bilayer naturally curved beams and cylindrical shells due to oil extraction from the outer layers. We fabricate bilayer naturally curved beams and cylindrical shells made of PDMS/(PDMS + silicone oil), use the experimental results to validate an explicit formula delivering the change in curvature of the beams, based on the modeling of oil extraction as a bulk contraction. We show as the same model, set up within a 3D context, delivers the morphing of bilayer cylindrical shells and identify potentially interesting results for designing future experiments. In particular, we show as stable states corresponding to the original cylindrical shells can be got in the form of saddle-like shells and cylindrical shells with the axes of principal curvatures switched with respect to the original axes.

Contents

1. Introduction 1
2. Material and methods 2
3. Beam flattening and eversion induced by oil extraction 2
4. Shape-shifting of cylindrical shells due to oil extraction 3
5. Conclusions 4
Declaration of competing interest 4
Acknowledgments 4
References 4

1. Introduction

In the last decades, polydimethylsiloxane (PDMS) has become popular for the rapid prototyping of many devices widely used in manufacturing and biomedical industries [1]. This is due to the many advantageous characteristics of the material: transparency, biocompatibility, flexibility, high cost-effectiveness and good moldability. [2] PDMS is a rubber-like material. However, owing to its porous nature and compatibility with organic solvents [3], it shows a gel-like behavior swelling when a solvent diffuses into the polymer and, vice versa, shrinking when it comes out from it. This property, together with the PDMS hydrophobicity, allowed to realize several devices: sponges for water–oil separation [4–6], solvent-tunable microlens [7], wrinkled microelectrodes [8], and wireless passive radio frequency identification sensors (RFID) based on PDMS swelling caused by organic vapour solvents [9]. In functionalized or composite PDMS, deformation can also be induced in response to external stimuli as pH [10], UV irradiation [11] and magnetic field [12].

Some drawbacks may arise when the swelling(shrinking)-induced deformation of PDMS structures is undesired. For example, the modification of PDMS microchannel geometries due to swelling can affect the trajectories of droplets [13]. In some cases, such as after the extraction of silicone uncrosslinked chains [14] or after ion beam and electron beam irradiation [15] these undesired deformations are irreversible, too.

In the present paper, we investigate shape-morphing of PDMS-based thin bilayer structures, which is a quite common configuration employing PDMS as both passive [16] and active layer [17] (see also [18]). Mismatch strains due to expansion(shrinkage) of the active layer can induce a macroscopic bending or surface instabilities, depending on different material and geometrical parameters [19]. Slender bilayer self-bending soft structures can be used as sensors and actuators in soft robotics, as drug delivery system, or can represent the single element of an architectural

* Correspondence to: Dipartimento di Ingegneria Strutturale e Geotecnica, via Eudossiana 18, I-00184 Roma, Italy
E-mail addresses: daniele.battista@uniroma1.it (D. Battista), valeriy.luchnikov@uha.fr (V. Luchnikov), paola.nardinocchi@uniroma1.it (P. Nardinocchi).

https://doi.org/10.1016/j.eml.2020.100655
2352-4316/

material. All these situations require an accurate control of the deformation process and we wish to make some progress towards addressing this question.

We present the results of a campaign of experimental tests made on bilayer naturally curved PDMS beams, with the outer layer containing oil. The beams are made to flatten and evert through oil extraction from the outer layer. The final change in curvature of the beam can be explicitly determined starting from the spontaneous shrinking deformation of the outer layer due to oil extraction. The explicit model is borrowed from [20] and it is shown to be in good agreement with the experimental results. Shape-shifting due to oil extraction in bilayer PDMS cylindrical shells is also presented in terms of a model set within the context of finite elasticity with spontaneous deformations. The model is solved via finite element method and it allows to determine the amount of oil to put in the outer layer of a cylindrical shell of given axis and curvature to get after oil extraction a cylindrical shell with axis orthogonal to the original one, saddle-like shapes and double-curved shapes.

2. Material and methods

The goal of our experiments is inducing bending in bilayer naturally curved PDMS beams through shrinking of just one of the two layers. The naturally curved beams are obtained by cutting them from a cylindrical bilayer thin structure in the hoop direction just after the end of the curing process described in the following. The preparation of the bilayer cylinders is resumed in the cartoon in Fig. 1. The procedure followed to realize the two layers had already been used by one of the Authors and exhaustively described in [21]. Shortly, one layer is made up of polydimethylsiloxane (PDMS) (SYLGARD^{TM}184) at a 10 : 1 ratio of prepolymer/crosslinker (the passive layer). The second (active) layer is made up of PDMS mixed with silicone oil (Rhodorsil® Oil 47V20) at 10 : x : 1 ratio of prepolymer/oil/crosslinker, with $x = 2, 4, 6, 8, 10$; during the curing process, as the PDMS reticulates, the silicone oil remains trapped into the polymer matrix.

The external (active) layer of the cylindrical shell is formed by pouring the PDMS-oil-curing agent liquid mixture into the space between the hollow cylinder (B) of internal radius 22 mm and the full cylinder (C) of radius 20 mm. After degassing and curing at 100 °C for 1 h, the cylinder (C) is extracted and another one (D) of smaller radius 18 mm is inserted coaxially to (B). The inner (passive) layer is formed by pouring the PDMS-curing agent liquid mixture into the space between the outer layer just crosslinked and the cylinder (D). It follows a second degassing and heating, at 100 °C for a time sufficient to complete all chemical reactions (about 2 h). After the mold opening the two parts result glued each other and form a cylindrical bilayer shell with middle radius 20 mm and thickness 4 mm. Already at this stage, it is expected that the oil starts partially diffusing through the inner layer. However, we do not observe relevant effects on the curving of the sample since the curing time is much shorter than the diffusion time.

The samples are then immersed in a toluene bath. The complete extraction of the oil is produced in a few hours. The final configuration which the bilayer beam gets is bent with respect to the initial, stable and maintained.

3. Beam flattening and eversion induced by oil extraction

In the process described above, four main phases can be identified: (i) diffusion of oil from the outer (active) to the inner (passive) layer, which takes place even when the layers are still in the mold; (ii) swelling of the bilayer in toluene; (iii) diffusion of oil from the swollen bilayer into the toluene bath; (iv) evaporation of toluene. At the stationary state, corresponding to the complete oil extraction, the PDMS bilayer beam looks like bent, due to the loss of oil from one layer, and swollen, due to the toluene absorption by both layers. The final shape is attained when all the toluene is evaporated and the bilayer is shrinked. Fig. 2 shows the final shapes of a set of beams sharing the same initial beam curvature κ_c and thickness h but different one from another for the silicone oil content x: the ratio of prepolymer/oil/crosslinker is 10 : x : 1 and $x = 2, 4, 6, 8, 10$. It is shown that there are values of x which determine, after oil extraction, beam flattening ($x = 6$) and beam eversion ($x > 6$).

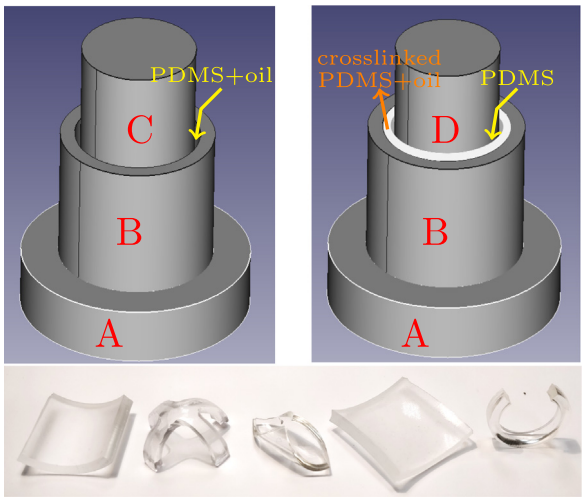

Fig. 1. Top: bilayer cylinder fabrication. The outer layer is formed by pouring the PDMS-oil-curing agent liquid mixture into the space between the hollow cylinder (B) and the full cylinder (C). After degassing and curing, the cylinder (C) is removed and (D) is inserted coaxially to (B). The inner layer is formed by pouring the PDMS-curing agent liquid mixture into the space between the outer layer just crosslinked and the cylinder (D). Bottom: some shapes made by the same bilayer structure fabricated by using the same kind of procedure.

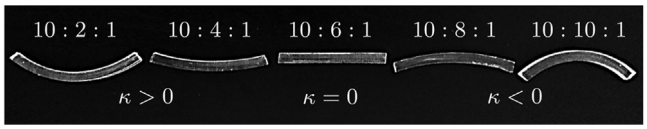

Fig. 2. Bilayer naturally curved beams after oil extraction for several values of the oil fraction. The initial configuration has a curvature $\kappa_c = 50$ m^{-1}, thickness $h = 4$ mm. The oil is in the outer layer.

As observed, oil extraction from the outer layer induces relevant deformations in the naturally curved beam, which produce beam flattening and eversion. In this situation, the well-known linear Timoshenko formula [22] fails in describing the change in curvature, as it fails when swelling-induced eversion and flattening in gel beams is studied [20], because it is valid for small deformations and slightly naturally curved beams. We adopt the explicit nonlinear formula presented in Ref. [20] to evaluate the curvature κ acquired by the beam at the end of the extraction process. It has been shown to depend on geometrical parameters such as the beam thickness h, the layer thicknesses h_i and h_e (i=inner layer, e=external layer), and the initial curvature κ_c as well as on the shear moduli G_i and G_e of the two layers, and on the natural longitudinal deformations λ_{oi} and λ_{oe}. These latter are defined as the deformations which would take place in the two layers if they were free one from another. The curvature formula

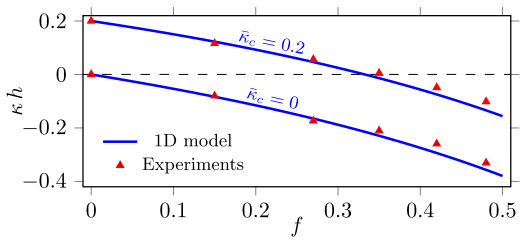

Fig. 3. Normalized curvature $\bar{\kappa} = \kappa h$ versus oil fraction f for a naturally straight beam and a naturally curved beam with silicone oil in the outer layer. The blue solid lines represent the 1D reduced model; the red triangles represent the experimental results.

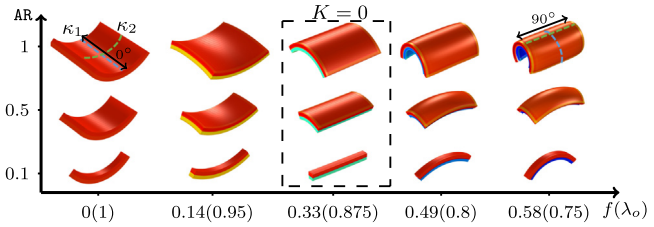

Fig. 4. Morphing of bilayer naturally curved beam (bottom) and cylindrical shells (center and top) due to a bulk contraction λ_o in the outer layer. The corresponding values of the oil fraction increase from left to right. The initial curvature $\kappa_2 = \kappa_c$ can be find by looking at the $f = 0$ column. At $\lambda_o = \lambda_o^\star = 0.875 (f = f^\star = 0.33)$ (third column) the Gaussian curvature K vanishes.

has the following form[1]

$$\kappa = \hat{\kappa}(\alpha, \beta, \Gamma, \bar{\kappa}_c, h, \lambda_{oe}), \tag{3.1}$$

with $\alpha = G_i/G_e$, $\beta = h_i/h$, $\Gamma = \lambda_{oe}/\lambda_{oi}$ and $\bar{\kappa}_c = \kappa_c h$.

We assume that λ_{oi} and λ_{oe} are determined by the bulk contraction due to oil extraction from the bilayer PDMS beam. Specifically, as oil is only present in the external layer, we set $\lambda_{oi} = 1$, that is, we consider the inner layer as a passive layer. On the other hand, we assume that oil is completely extracted from the external layer and set

$$\lambda_{oe} = (1-f)^{1/3} \quad \text{with} \quad f = V_o/(V_p + V_{c-l} + V_o), \tag{3.2}$$

with the oil fraction $f = x/(11+x)$ defined as the ratio between the amount of oil V_o and the total volume of the layer containing the oil, that is, the sum of the volume V_p of the prepolymer, the volume V_{c-l} of the cross-linker and V_o. It holds: $f < 1$ and $\lambda_{oe} < 1$.

In our experiments, $\alpha \simeq 1$, $\beta = 1/2$, $\Gamma = \lambda_{oe} = (1-f)^{1/3}$. Moreover, for small initial curvatures $\bar{\kappa}_c \to 0$ we get a simpler formula from Eq. (3.1) which is valid for almost flat beams:

$$\kappa^{\text{flat}} = \frac{12\lambda_{oe}(1-\lambda_{oe})(\lambda_{oe}+1)^2\left(\lambda_{oe}^2+6\lambda_{oe}+1\right)}{h\left(\lambda_{oe}^4+3\lambda_{oe}^3+8\lambda_{oe}^2+3\lambda_{oe}+1\right)^2}. \tag{3.3}$$

Eqs. (3.1) and (3.3) deliver the curvature of the beam axis for a naturally curved and flat beam, respectively. Fig. 3 shows that they are in excellent agreement with experimental data.

4. Shape-shifting of cylindrical shells due to oil extraction

The good agreement between experimental and explicit results for beams, suggested to study the deformations induced by oil extraction in bilayer PDMS cylindrical shells within the context of three-dimensional finite elasticity with distortions (natural deformations). These latter, as for the beams, are induced by oil extraction from the outer layer. The difference between curved beams and cylindrical shell is in the aspect ratio: small aspect ratios identify beams, large aspect ratios identify cylindrical shells.

Similarly to what we did for the beam curvature formulas (3.1) and (3.3), we assume that a bulk contraction corresponds to the complete extraction of oil from the external layer; it determines the stationary configuration of the cylindrical shell we aim to characterize.

The reference state $\mathcal{B}$ of the 3D continuum is a bilayer cylindrical shell with a principal curvature $\kappa_2 \neq 0$ equal to the curvature κ_c of the beam cutted from it in the hoop direction (and $\kappa_1 = 0$). Fig. 4 shows the reference states of cylindrical shells (left top and center cartoons) and beam (left bottom cartoon). Moreover, denoted with L the length of the beam, as well as the arc length of the cylindrical shells(beam), and with $\mathtt{AR}$ the ratio between the width w of the cylindrical shells(beam) and L, it holds $\mathtt{AR} = 0.1$, $\mathtt{AR} = 0.5$ and $\mathtt{AR} = 1$ for the beam and the cylindrical shells in the left cartoons in Fig. 4.

The dynamics of the process is beyond the scope of the paper and we focus on the equilibrium states of the polymer bodies. Introduced as state variable of the problem the displacement field $\mathbf{u}$ from $\mathcal{B}$, we denote with $x = X + \mathbf{u}(X)$ the position of a point $X \in \mathcal{B}$ at the steady state attained after oil extraction. We multiplicatively decompose the deformation gradient $\mathbf{F} = \mathbf{I} + \nabla\mathbf{u}$ in a pure inelastic deformation (bulk contraction) $\mathbf{F}_o$ and an elastic deformation $\mathbf{F}_e$. We also assume that $\mathbf{F}_o = \lambda_o\mathbf{I}$ with $\lambda_o = 1$ in the passive layer and $\lambda_o < 1$ in the active layer. On the other hand, the elastic deformation $\mathbf{F}_e$ is assumed to be isochoric, that is, such that $\det\mathbf{F}_e = 1$. Hence, volume changes are only due to the distortion λ_o which models the bulk contraction in the active layer due to oil extraction. It can be shown [23] that the following constitutive equations hold for the (reference) stress $\mathbf{S}$, corresponding to an elastically incompressible neo-Hookean material:

$$\mathbf{S} = G\lambda_o\mathbf{F} - p(\det\mathbf{F})\mathbf{F}^{-T}, \tag{4.4}$$

with p the reactive stress maintaining the volumetric constraint $\det\mathbf{F}_e = 1$.[2]

We implement within the finite element code COMSOL Multiphysics the mechanical equilibrium equation $\mathtt{div}\,\mathbf{S} = \mathbf{0}$, in a weak form, together with the boundary conditions of zero tractions. Eventually, we assume some boundary conditions on $\mathbf{u}$ that eliminate any rigid motions without generating reaction forces. We look for the solutions of the stationary problem corresponding to different values of the deformation λ_o, and for different $\mathtt{AR}$ (keeping fixed the arc length L). We set $L = 35$mm, $h = 4$mm, $\beta = 1/2$, $G_i = G_e = 1$ MPa and fixed the initial curvature $\kappa_2 = \kappa_c = 50\text{m}^{-1}$ of the cylindrical shell.

Fig. 4 shows the outcomes of the numerical simulations for $\mathtt{AR} = 0.1$ (bottom row of cartoons corresponding to a curved beam), $\mathtt{AR} = 0.5$ and $\mathtt{AR} = 1$ (center and top rows of cartoons, respectively, corresponding to a cylindrical shell). Bulk contraction of the external layer increases from left to right. It corresponds to a distortion λ_o decreasing from left to right in the top, center and bottom rows of cartoons and taking the values $\lambda_o = (1, 0.95, 0.875, 0.8, 0.75)$. The corresponding values of the oil fraction are $f = (0, 0.14, 0.33, 0.49, 0.58)$. So, left top, center and bottom cartoons correspond to the reference states of beam and cylindrical shells. As expected, to decreasing values of λ_o, the bilayer beam undergoes curvature reduction, flattening and

[1] See the appendix of Ref. [20] for the explicit formula

[2] It is worth noting that, due to the elastic incompressibility constraint, $\det\mathbf{F} = \lambda_o^3$.

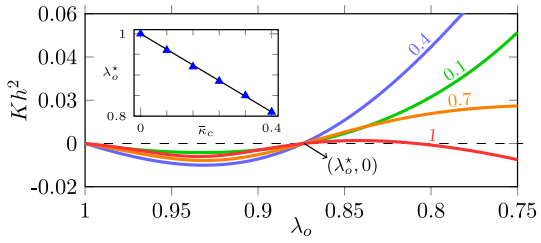

Fig. 5. Normalized Gaussian curvature $\bar{K} = Kh^2$ versus the bulk contraction λ_o varying from 1 to 0.75, for aspect ratios $\mathtt{AR} = 0.1, 0.4, 0.7, 1$ (green, blue, orange, red lines). The inset shows the dependence of the $\lambda_o^\star$ on the initial dimensionless curvature $\bar{\kappa}_c$ of the cylindrical shell; the pattern corresponds to $L = 35$ mm, $h = 4$ mm, $\beta = 1/2$, $G_i = G_e = 1$ MPa. (For interpretation of the references to color in this figure legend, the reader is referred to the web version of this article.)

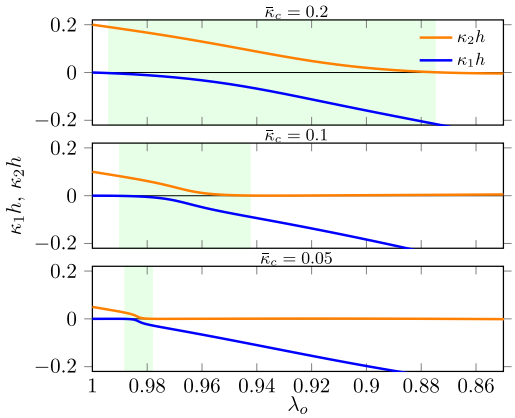

Fig. 6. Normalized principal curvatures $\kappa_1 h$ (blue lines) and $\kappa_2 h$ (orange lines) versus the bulk contraction λ_o varying from 1 to 0.85, for $\bar{\kappa}_c = 0.2$ (top plot), $\bar{\kappa}_c = 0.1$ (center plot), $\bar{\kappa}_c = 0.05$ (bottom plot), and keeping fixed $\mathtt{AR} = 1$. The green area identifies, for each value of $\bar{\kappa}_c$, the range of λ_o for which a saddle-like shape is attained. (For interpretation of the references to color in this figure legend, the reader is referred to the web version of this article.)

eversion. On the contrary, the morphing of the shells with $\mathtt{AR} = 0.5$ and $\mathtt{AR} = 1$ shown in Fig. 4 is noteworthy.

Firstly, at $\lambda_o = \lambda_o^\star = 0.875$, corresponding to $f = f^\star = 0.33$, we get cylindrical shells with the principal curvature axes switched with respect to the reference state: $\kappa_1 \neq 0$ and $\mathtt{sign}\kappa_1 = -\mathtt{sign}\kappa_2$ (see the cylindrical shells within the dashed frame in Fig. 4, third column).

The value $\lambda_o^\star$ which identifies the switched cylindrical shell is the same for any AR. Moreover, changing the initial curvature κ_c, the value $\lambda_o^\star$ changes even if it is still the same for any AR (see the inset in Fig. 5). Hence, given the initial curvature, we can evaluate the amount of oil to add to the polymer mixture to produce the shift of the two axes of the cylindrical shell. For $\lambda_o^\star < \lambda_o < 1$, the beam decreases its curvature and flattens, while the cylindrical shells morph into cylindrical shells with the axes of principal curvatures switched, passing through saddle-like shapes (Fig. 4, second and third columns from left). For $\lambda_o < \lambda_o^\star$, that is, $f > f^\star$, the beam everts, the shell with $\mathtt{AR} = 0.5$ attains a double-curved shape with $\kappa_1 < 0$ and $\kappa_2 < 0$, and the shell with $\mathtt{AR} = 1$ bends along the direction orthogonal to the initial one (Fig. 4, fourth and fifth column from left).

The morphing described above via the cartoons in Fig. 4 is also shown in Fig. 5 through the values taken by the normalized Gaussian curvature $\bar{K} = Kh^2$, with $K = \kappa_1\kappa_2$, evaluated at the center of the middle surface in the stationary configuration at different values of λ_o from 1 to 0.75, for several AR ranging between 0.1 and 1. For any AR, all the curves cross the zero line in two points: at $\lambda_o = 1$, which corresponds to the reference state, and at $\lambda_o = \lambda_o^\star$, corresponding to the cylindrical shells with the axes of principal curvature switched with respect to the reference axes. Interestingly, the value $\lambda_o = \lambda_o^*$ corresponds to the value which makes null the curvature of a naturally curved beam (see Eq. (3.1)).

Fig. 5 also shows as $\lambda_o^\star$ identifies the transition from saddle-like shapes and shapes with positive Gaussian curvature. Indeed, it can be observed that for $\lambda_o > \lambda_o^*$, we have $K < 0$ for all the aspect ratios (saddle-like shape); for $\lambda_o < \lambda_o^*$, we have $K > 0$ for $\mathtt{AR} = 0.1, 0.4, 0.7$, and $K \simeq 0$ for $\mathtt{AR} = 1$.

In Fig. 6, we show how the transition from a given cylindrical shell to the cylindrical shell with switched axes changes when the normalized initial curvature $\bar{\kappa}_c = \kappa_c h$ of the shell decreases. The normalized principal curvatures $\kappa_1 h$ (blue lines) and $\kappa_2 h$ (orange lines) are evaluated at the center of the middle surface in the stationary configuration at different values of λ_o from 1 to 0.85, for $\bar{\kappa}_c = 0.2, 0.1, 0.05$ and keeping fixed $\mathtt{AR} = 1$. It is observed that the range of λ_o values which allows to get a saddle-like shape is smaller and smaller as the cylindrical shell is thinner and thinner, and the green band in Fig. 6 is narrow and narrow. These observations allow us to make a precise design of the recipe used to realize the PDMS layer with oil inside, once fixed the thickness and the curvature of the cylindrical shell.

5. Conclusions

We investigated the shape-shifting of bilayer polymer beams and cylindrical shells due to oil extraction. Polymer beams are made to evert through oil extraction from the outer layer. The morphing mechanism is also studied through an explicit model which accurately describes the observed morphing. The good agreement between experiments and modeling in beams inspired the computational study of cylindrical shells under the same working conditions, which will be supported in the next future by the appropriate experimental tests and also reviewed in view of the recent study presented in Ref. [24].

Declaration of competing interest

The authors declare that they have no known competing financial interests or personal relationships that could have appeared to influence the work reported in this paper.

Acknowledgments

DB and PN would like to thank *PRIN 2017*, Italy, *Mathematics of active materials: From mechanobiology to smart devices* (Italian Minister for Education, Research, and University (MIUR), grant n. 2017KL4EF3) for financial support. DB also acknowledges the National Group of Mathematical Physics (GNFM-INdam) for financial support (*Young Research Project*, grant n. U-UFMBAZ-2018-000356).

References

[1] A.L. Thangawng, R.S. Ruoff, M.A. Swartz, M.R. Glucksberg, An ultra-thin PDMS membrane as a bio/micro–nano interface: fabrication and characterization, Biomed. Microdevices 9 (4) (2007) 587–595, http://dx.doi.org/10.1007/s10544-007-9070-6.

[2] R. Mukhopadhyay, When PDMS isn't the best, Anal. Chem. 79 (9) (2007) 3248–3253, http://dx.doi.org/10.1021/ac071903e, arXiv:https://doi.org/10.1021/ac071903e, PMID: 17523228.

[3] J.N. Lee, C. Park, G.M. Whitesides, Solvent compatibility of poly(dimethylsiloxane)-based microfluidic devices, Anal. Chem. 75 (23) (2003) 6544–6554, http://dx.doi.org/10.1021/ac0346712, arXiv:https://doi.org/10.1021/ac0346712, PMID: 14640726.

[4] X. Zhao, L. Li, B. Li, J. Zhang, A. Wang, Durable superhydrophobic/superoleophilic pdms sponges and their applications in selective oil absorption and in plugging oil leakages, J. Mater. Chem. A 2 (2014) 18281–18287, http://dx.doi.org/10.1039/C4TA04406A.

[5] D. Zhu, S. Handschuh-Wang, X. Zhou, Recent progress in fabrication and application of polydimethylsiloxane sponges, J. Mater. Chem. A 5 (2017) 16467–16497, http://dx.doi.org/10.1039/C7TA04577H.
[6] A. Turco, E. Primiceri, M. Frigione, G. Maruccio, C. Malitesta, An innovative, fast and facile soft-template approach for the fabrication of porous PDMS for oil–water separation, J. Mater. Chem. A 5 (2017) 23785–23793, http://dx.doi.org/10.1039/C7TA06840A.
[7] D.-X. Lu, Y.-L. Zhang, D.-D. Han, H. Wang, H. Xia, Q.-D. Chen, H. Ding, H.-B. Sun, Solvent-tunable PDMS microlens fabricated by femtosecond laser direct writing, J. Mater. Chem. C 3 (2014) http://dx.doi.org/10.1039/C4TC02737J.
[8] B. Ji, M. Wang, Z. Guo, W. Hong, L. Wang, X. Wang, B. Yang, W. Wang, J. Liu, Wrinkled microelectrode interface based on oil-pretreated hyperelastic substrate, in: 2019 IEEE 32nd International Conference on Micro Electro Mechanical Systems, MEMS, 2019, pp. 561–564, http://dx.doi.org/10.1109/MEMSYS.2019.8870820.
[9] C.V. Rumens, M.A. Ziai, K.E. Belsey, J.C. Batchelor, S.J. Holder, Swelling of PDMS networks in solvent vapours; applications for passive RFID wireless sensors, J. Mater. Chem. C 3 (2015) 10091–10098, http://dx.doi.org/10.1039/C5TC01927C.
[10] Y. Liu, H. Zhang, J. Zhang, Y. Zheng, Constitutive modeling for polymer hydrogels: a new perspective and applications to anisotropic hydrogels in free swelling, Eur. J. Mech. A Solids 54 (2015) 171–186, http://dx.doi.org/10.1016/j.euromechsol.2015.07.001, http://www.sciencedirect.com/science/article/pii/S0997753815000753.
[11] D.H. Kim, M.C. Jung, S.-H. Cho, S.H. Kim, H.-Y. Kim, H.J. Lee, K.H. Oh, M.-W. Moon, UV-Responsive nano-sponge for oil absorption and desorption, Sci. Rep. 5 (12908) (2015) http://dx.doi.org/10.1038/srep12908.
[12] D.C. Stanier, J. Ciambella, S.S. Rahatekar, Fabrication and characterisation of short fibre reinforced elastomer composites for bending and twisting magnetic actuation, Composites A 91 (2016) 168–176, http://dx.doi.org/10.1016/j.compositesa.2016.10.001, http://www.sciencedirect.com/science/article/pii/S1359835X16303281.
[13] R. Dangla, F. Gallaire, C.N. Baroud, Microchannel deformations due to solvent-induced PDMS swelling, Lab Chip 10 (2010) 2972–2978, http://dx.doi.org/10.1039/C003504A.
[14] A. Hourlier-Fargette, J. Dervaux, A. Antkowiak, S. Neukirch, Extraction of silicone uncrosslinked chains at air–water–polydimethylsiloxane triple lines, Langmuir 34 (41) (2018) 12244–12250, http://dx.doi.org/10.1021/acs.langmuir.8b02128, arXiv:https://doi.org/10.1021/acs.langmuir.8b02128, PMID: 30199255.
[15] B. Liu, J. Fu, Modulating surface stiffness of polydimethylsiloxane (PDMS) with kiloelectronvolt ion patterning, J. Micromech. Microeng. 25 (2015) http://dx.doi.org/10.1088/0960-1317/25/6/065006.
[16] J. Xie, X. Han, H. Ji, J. Wang, J. Zhao, C. Lu, Self-supported crack-free conducting polymer films with stabilized wrinkling patterns and their applications, Sci. Rep. 6 (36686) (2016) http://dx.doi.org/10.1038/srep36686.
[17] J. Jackson, A. Chen, H. Zhang, H. Burt, M. Chiao, Design and near-infrared actuation of a gold nanorod–polymer microelectromechanical device for on-demand drug delivery, Micromachines 9 (1) (2018) http://dx.doi.org/10.3390/mi9010028, https://www.mdpi.com/2072-666X/9/1/28.
[18] L. Chia, P. Bollgruen, A. Egunov, D. Mager, F. Malloggi, J. Korvink, V. Luchnikov, Vapour processed self-rolled poly(dimethylsiloxane) microcapillaries form microfluidic devices with engineered inner surface, Lab Chip 13 (2013) http://dx.doi.org/10.1039/c3lc50542a.
[19] T. Sigaeva, R. Mangan, L. Vergori, M. Destrade, L. Sudak, Wrinkles and creases in the bending, unbending and eversion of soft sectors, Proc. R. Soc. A 474 (2212) (2018) 20170827, http://dx.doi.org/10.1098/rspa.2017.0827, https://royalsocietypublishing.org/doi/abs/10.1098/rspa.2017.0827, arXiv:https://royalsocietypublishing.org/doi/pdf/10.1098/rspa.2017.0827.
[20] D. Battista, M. Curatolo, P. Nardinocchi, Swelling-induced eversion and flattening in naturally curved gel beams, Int. J. Mech. Sci. 161–162 (2019) 105071, http://dx.doi.org/10.1016/j.ijmecsci.2019.105071, http://www.sciencedirect.com/science/article/pii/S0020740319315954.
[21] A.I. Egunov, J.G. Korvink, V.A. Luchnikov, Polydimethylsiloxane bilayer films with an embedded spontaneous curvature, Soft Matter 12 (2016) 45–52, http://dx.doi.org/10.1039/C5SM01139F.
[22] S. Timoshenko, Analysis of bimetal thermostats, J. Opt. Soc. Am. B 11 (1925) 233–255.
[23] M. Curatolo, S. Gabriele, L. Teresi, Swelling and growth: a constitutive framework for active solids, Meccanica 52 (14) (2017) 3443–3456, http://dx.doi.org/10.1007/s11012-017-0629-x.
[24] D. Battista, M. Curatolo, P. Nardinocchi, Enforcing shaping of thin gel sheets by anisotropic swelling, Mech. Mater. 139 (2019) 103199, http://dx.doi.org/10.1016/j.mechmat.2019.103199, http://www.sciencedirect.com/science/article/pii/S016766361930599X.

5

DYNAMICS OF POLYMER BEAMS DRIVEN BY SOLVENT DIFFUSION

During the experimental campaign described in I it is observed that, once the PDMS/(PDMS + silicone oil) bilayer is prepared, if the silicone oil extraction step is skipped, the latter begins to diffuse into the pure PDMS layer. This diffusion process manifests itself macroscopically with a progressive bending of the beam due to a swelling of the layer into which the oil penetrates and a shrinking of the layer from which the oil emigrates, until the diffusion stops and a condition of stationary equilibrium is reached. The six images in Figure 20 are some shots of the evolution of a naturally flat bilayer beam with the silicon oil located in the top layer, and correspond to instants of time $t = 1, 24, 48, 72, 96, 120$ h. The numerical values of the parameters are shown in Table 1. The dis-affinity χ is computed from the free-swelling equation [48]

$$\frac{G\Omega}{\lambda_o} + \mathcal{R}T\left(\log\frac{\lambda_o^3 - 1}{\lambda_o^3} + \frac{1}{\lambda_o^3} + \frac{\chi}{\lambda_o^6}\right) = 0\,, \tag{5.0.64}$$

with the universal gas constant $\mathcal{R} = 8.314$ J/(K mol), the room temperature $T = 293$ K, the shear modulus $G = 0.4$ MPa and the equilibrium stretch $\lambda_o \simeq 1.13$ measured in a free-swelling test.

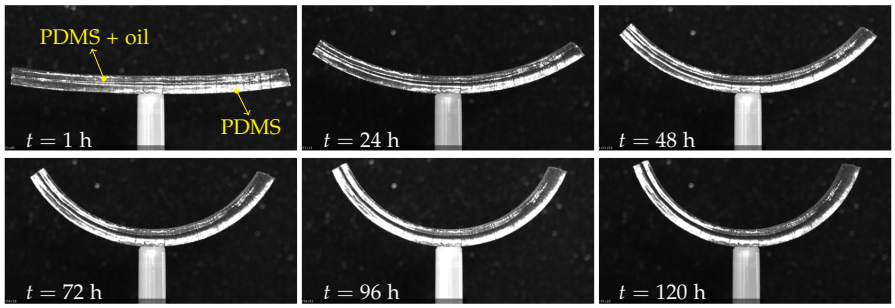

Figure 20: Bending of a bilayer PDMS/PDMS+oil beam due to oil diffusion from the top to the bottom layer. The six images represent the configurations assumed by the beam over 120 hours, with intervals of 24 hours, starting from the straight configuration. The ratio of prepolymer/oil/crosslinker is 10:6:1.

Parameter	Symbol and value
Length	$l = 60$ mm
Thickness	$h = 4$ mm
Thickness ratio	$\beta = 0.5$
Width	$w = 5$ mm
Fraction of oil	$f = 0.35$
Young's modulus of the top layer	$E_t = 0.8$ MPa (from [21])
Young's modulus of the bottom layer	$E_b = 1.2$ MPa (from [21])
Molar volume of the silicone oil	$\Omega = 3 \cdot 10^{-3}$ m^{3}mol^{-1}
Dis-affinity	$\chi \simeq 0$

Table 1: Numerical values of the parameters.

5.1 INTERNAL DIFFUSION

In I the dynamics of the oil extraction process goes beyond the scope of the paper. For this reason a three-dimensional finite elasticity model with distortions is considered suitable to describe the equilibrium state of the polymer bodies. However, to model the deformation of the body induced by the diffusion of the oil through the polymeric lattice, it is appropriate to consider the stress-diffusion continuum model described in Section 4.1, introducing some modifications. The reference configuration $\mathcal{B}$ is identified by a non-dry stress-free state. For this reason the subscript "d", which indicates in Section 4.1 that the quantities refer to the dry configuration, is eliminated here. The consequence of this choice is that the volumetric constraint (4.1.40) changes as follows

$$J = \det \mathbf{F} = \hat{J}(c) = 1 + \Omega(c - c_o)\,, \tag{5.1.65}$$

where c_o is the concentration of solvent at time $t = 0$, and $c_o = c_{ot}$ for the top layer and $c_o = c_{ob}$ for the bottom layer. With this modification, at time $t = 0$, when $c = c_o$, $J = 1$. The constitutive prescriptions (4.1.42)-(4.1.46) and the balance equations (4.1.47) remain unchanged. They must be complemented with boundary and initial conditions. It is assigned zero traction so that the beam is free to bend, and a displacement on the boundary that eliminates any rigid motion without generating reaction forces. Regarding the chemical boundary condition, zero solvent flow is assigned over the entire boundary, assuming the oil can't evaporate. Finally, $\mathbf{u} = 0$ and $c = c_o$ on $\mathcal{B}$ at $t = 0$ are set as initial conditions. The problem is then reformulated in weak form as described in Section 4.3, and solved numerically through the finite element software COMSOL Multiphysics.
In Figure 21 the squares represent the dimensionless curvature κh as a function of the dimensionless time $\tau = t/\bar{t}$ computed numerically

using the data in Table 1. The initial concentrations are set $c_{ob} = 0.01$ mol/m^3[1] and $c_{ot} = f/\Omega = 117.65$ mol/m ^{3}, which correspond to initial chemical potentials $\mu_{ob} = -21733$ J/mol and $\mu_{ot} = -750$ J/mol, respectively. The diffusivity of the solvent D is used as a calibration parameter to fit the time-scale of curvature. A parametric analysis is then carried out by varying D, and it is found that a value of $D \simeq 1.8 \cdot 10^{-11}$ m^2/s (orange squares) lead to the best fit to the experimental data. Green and red squares correspond to $D = 10^{-10}$ m^2/s and $D = 10^{-12}$ m^2/s, respectively. The blue triangles represent the experimental results; the curvature is measured with time intervals of acquisitions of 6 h, over a time window $\bar{t} = 180$ h.

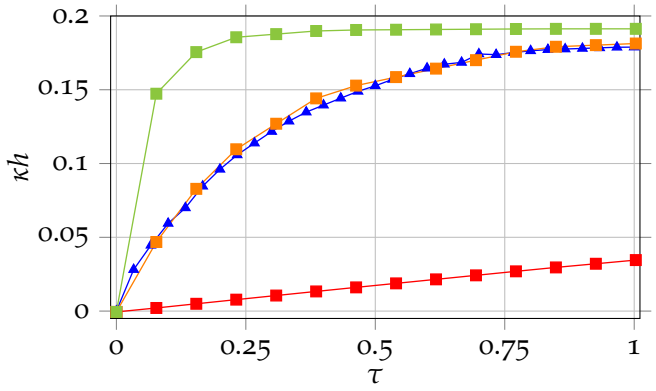

Figure 21: Dimensionless curvature κh versus dimensionless time $\tau = t/\bar{t}$, ranging between 0 and 1, over a time window $\bar{t} = 180$ h. The blue triangles represent the experimental data, acquired in 6-hours intervals; the squares represent the numerical results obtained using the parameters shown in Table 1, setting $c_{ob} = 0.01$ mol/m^3, $c_{ot} = f/\Omega = 117.65$ mol/m^3. Green, orange and red squares correspond to diffusivities $D = 10^{-10}$ m^2/s, $D = 1.8 \cdot 10^{-11}$ m^2/s and $D = 10^{-12}$ m^2/s, respectively. Orange squares are the best fit to the experimental data.

Taking the diffusivity value $D = 1.8 \cdot 10^{-11}$ m^2/s, Figure 22 shows the trend of the dimensionless concentration $c\,\Omega$ (left panel) and the dimensionless chemical potential $\mu/(\mathcal{R}T)$ (right panel) on the thickness mid-line parameterized by the coordinate $\zeta = 2z/h$, $\zeta \in (-1, 1)$, where $\zeta = -1$ and $\zeta = 1$ correspond to the bottom and top surface, respectively. The solid lines go from blue to red as time increases; following the direction of the arrows, they correspond to $\tau = 0.01, 0.03, 0.15, 0.3, 0.6, 1$. The red solid line, corresponding to $\tau = 1$, is the steady-state. It can be seen that the concentration is not uniform at equilibrium and does not correspond to the average $(c_{ob} + c_{ot})\Omega/2$ (red dashed line), as one would expect from a pure diffusion problem (see [95]); this depends on the coupling between

1 The concentration cannot be 0 because the chemical potential is not defined on the dry volume (it tends to $-\infty$). For this, a value for the concentration close to zero has been chosen.

the chemical and the mechanical problem, hence the distribution of the solvent depends on how the stresses are distributed. On the other hand, the chemical potential at equilibrium must be uniform on the section for the conservation of solvent mass equation $(4.1.47)_2$ to be satisfied.

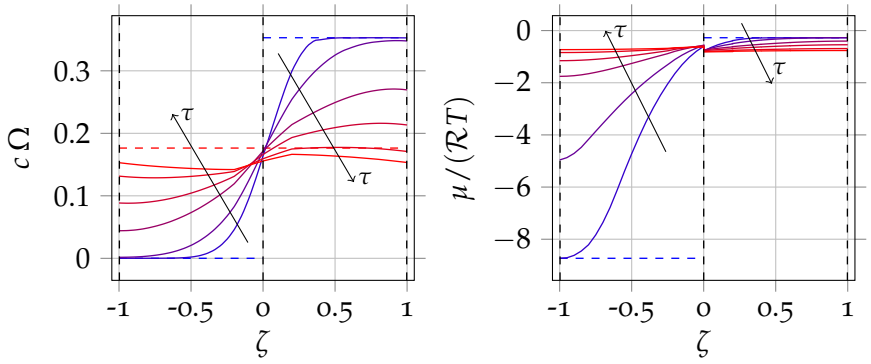

Figure 22: Dimensionless concentration $c\,\Omega$ (left panel) and chemical potential $\mu/(\mathcal{R}T)$ (right panel) versus $\zeta = 2z/h$, ranging between -1 ($z = -h/2$) and 1 ($z = h/2$), for $\tau = 0.01, 0.03, 0.15, 0.3, 0.6, 1$, increasing according to the arrows indicated in the plot. The red dashed line correspond to the average $(c_{ob} + c_{ot})\Omega/2$.

5.2 EXPLICIT PREDICTION OF THE STEADY-STATE

The aim is to make an estimate of the curvature reached by the beam in steady-state. Again the explicit formula for the curvature of a flat bilayer beam III-5.28 is used. Here, the parameters α, β, and h are assigned, and the problem consists in identifying the natural deformations $\bar{\lambda}_{ob}$ and $\bar{\lambda}_{ot}$, reached at equilibrium, knowing the initial concentrations of solvent c_{ob} and c_{ot} (see Figure 23).

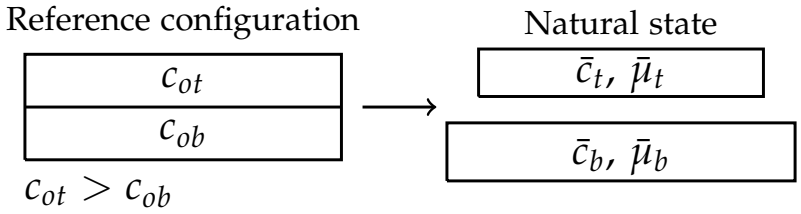

Figure 23: Reference configuration and ideal natural state at equilibrium, when diffusion stops.

Fixing $c_{ot} > c_{ob}$, the top and bottom layers would like to shrink ($\lambda_{ot} < 1$) and swell ($\lambda_{ob} > 1$), respectively, as molecules of oil are flowing from the former to the latter, without coming out of the beam, until a steady equilibrium condition is reached. Supposing that in the natural state at equilibrium the unknown concentrations $\bar{c}_b$ of the

bottom layer and $\bar{c}_t$ of the top layer are uniform, the following solvent mass conservation equation must hold:

$$\bar{c}_b h_b + \bar{c}_t h_t = c_{ot} h_t + c_{ob} h_b \,, \tag{5.2.66}$$

being h_b and h_t the thicknesses of the bottom and top layer. In conditions of chemical equilibrium, the chemical potential must be uniform over the whole beam. Hence, defining

$$\begin{aligned} \bar{\mu}_b &= \hat{\mu}(\bar{c}_b) + \bar{p}_b \Omega \,, \\ \bar{\mu}_t &= \hat{\mu}(\bar{c}_t) + \bar{p}_t \Omega \,, \end{aligned} \tag{5.2.67}$$

the steady-state chemical potential of the bottom and top layer, respectively, with the pressures $\bar{p}_b = G_b / \bar{\lambda}_{ob}$ and $\bar{p}_t = G_t / \bar{\lambda}_{ot}$, it must hold

$$\bar{\mu}_b = \bar{\mu}_t \,. \tag{5.2.68}$$

Finally, the volumetric constraint for the natural state reads

$$\begin{aligned} \bar{\lambda}_{ob}^3 &= 1 + \Omega(\bar{c}_b - c_{ob}) \,, \\ \bar{\lambda}_{ot}^3 &= 1 + \Omega(\bar{c}_t - c_{ot}) \,. \end{aligned} \tag{5.2.69}$$

The system constituted by equations (5.2.66), (5.2.68) and (5.2.69) can be solved, providing the unknowns ($\bar{c}_b$, $\bar{c}_t$, $\bar{\lambda}_{ob}$, $\bar{\lambda}_{ot}$), and the steady-state curvature can thus be calculated. Figure 24 displays the dimensionless curvature at steady-state κh as the dimensionless initial concentration of the top layer $c_{ot}\Omega$ varies, keeping the concentration of the bottom layer locked. The theoretical model is represented by the blue solid line and matches the numerical results (orange squares) well. The data shown in Table 1 are used for the calculations.

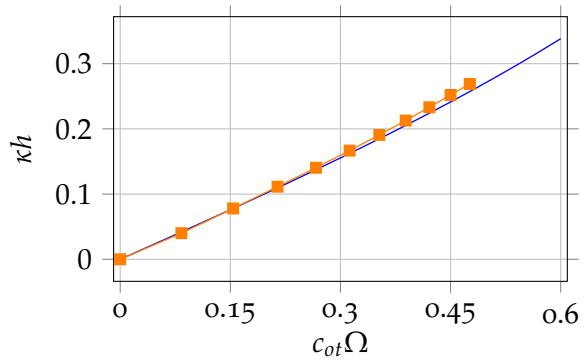

Figure 24: Dimensionless curvature at steady-state κh versus dimensionless initial concentration of the top layer $c_{ot}\Omega$. The blue solid line represents the theoretical prediction; the orange squares represent the numerical results. The data shown in Table 1 are used for the calculations.

6

NATURALLY FLAT SHEETS: PLATES AND CYLINDERS

In the previous chapters it has dealt with 1D geometries. Now, the elastic and inelastic processes described in Chapter 4 are studied for non-narrow sheets whose mid-surfaces have initial zero Gaussian curvature, namely plates and cylinders. Specifically, anisotropic swelling is here introduced for the analysis of the shaping of anisotropic bilayer gel plates, while, inelastic bulk contraction is used to model the oil extraction from a bilayer cylindrical shell, inducing its eversion.

6.1 ANISOTROPIC SWELLING

Under free conditions homogeneous gels only involve change in size once immersed in a solvent bath. In fact, swelling process is intrinsically isotropic as is the structure of the Flory-Rehner free-energy $\psi(\mathbf{F}_d, c_d) = \psi_e(\mathbf{F}_d) + \psi_m(c_d)$, with $\psi_e(\mathbf{F}_d)$ and $\psi_m(c_d)$ given by equations (4.1.44), presented in Section 4.1.
Now consider a gel in which reinforcing fibers are inserted to form a composite material with a swellable matrix. The fibers give the gel anisotropic elastic properties as experimentally investigated in [22]. The so-called *anisotropic swelling* is here described through an extension of the elastic component of the free-energy, by adding energetic contributions based on some invariants of deformations, as introduced in [77] to describe the mechanical behavior of anisotropic materials, while the polymer-water mixing component always maintains an isotropic structure. As proposed in [59, 60, 63], the Flory-Rehner free-energy is revised in order to account the hampering of the swelling-induced deformations along the stiff fibers direction:

$$\psi^{ani}(\mathbf{F}_d, c_d) = \psi(\mathbf{F}_d, c_d) + \frac{1}{2} G\gamma \left(\mathbf{F}_d\mathbf{e} \cdot \mathbf{F}_d\mathbf{e} - 1\right)^2 , \tag{6.1.70}$$

with the unit vector field $\mathbf{e}$ as the fiber direction and γ a stiffening parameter, whose mechanical meaning has been largely analyzed in [54] through deformation tests. While the constitutive equation for the chemical potential remains unchanged ((4.1.42)$_2$) for isotropic/anisotropic swelling, the constitutive equation delivering the stress prescribes that

$$\mathbf{S} = G\mathbf{F}_d + 2G\gamma(\mathbf{F}_d\mathbf{e} \cdot \mathbf{F}_d\mathbf{e} - 1)\mathbf{F}_d\mathbf{e} \otimes \mathbf{e} - p\mathbf{F}_d^{\star} . \tag{6.1.71}$$

Consider an isotropic bilayer plate subject to a differential growth, elastic or inelastic, of the two layers and imagine to gradually increase the mismatch strain in the absence of external mechanical actions. Since both the material and the growth are isotropic, the plate initially deforms into a spherical cap for relatively small values of the mismatch strain. By further increasing the latter, deforming into a spherical cap becomes too energetically costly above a certain threshold, and the symmetry of the plate is broken by bifurcating into a developable surface (cylindrical surface). This type of problem has been extensively studied in the Literature (see for example [28]), and it is well known that the threshold of bifurcation and the bending direction of the cylindrical surface is strongly affected by the size and the shape of the plate [21, 37, 66]).
The stimuli-induced curling of bilayer film has a technological implication as an original manufacturing method for micro- and nanotubes from 2D films [50]. Some applications include nanoreactors [17], optical microtube resonators [82], and components for on-chip capture and detection of individual micro/nano-organisms [75].
In II the swelling-driven shaping of bilayer gel rectangular plates is investigated numerically with the three-dimensional stress-diffusion model presented in 4.1, focusing on the steady shapes attained, starting from a dry flat sheet.
Firstly, a parametric analysis campaign is carried out on plates subjected to isotropic swelling varying the ratio between the stiffness of the two layers, the slenderness ratio, and the aspect ratio of the rectangular plate, fixing the length of one side. In particular, the aspect ratio would appear to be a determinant of the final shape attained by the plate (see Figure II-3). The aim is to identify the bifurcation threshold between the spherical shape and the nearly developable shape, represented in terms of the natural curvature κ_o of the plate. The latter is measurable by cutting a beam out of the plate and identifying the natural curvature κ_o with the curvature realized by that beam through the explicit formula proposed in [47], here revised in energy key in Section 3.1. The measured value of $\bar{\kappa}_o = \kappa_o h$ is then compared with a theoretical threshold $\bar{\kappa}_{ob}$ (formula II-3.12), presented in [66] and slightly revised in [67] to account the isotropic growth (see formula II-3.13). However, it is seen that the theoretical threshold is far from predicting that measured numerically and it requires further investigation.
Secondly, reinforcing fibers are introduced inside the gel matrix in order to explore the possibility to enforce the cylindrical shaping. Actually, the presence of the fibers is fictitious and is simulated by the anisotropic swelling described in Section 6.1. The fibers are parallel to one side of the plate and homogeneously distributed in both the

layers or only in one of them. It is observed that the latter architecture provides a better enforcing cylinder-like shapes, as Figure II-4 shows. Moreover, a larger suppression of the anticlastic curvature is observed by inserting fibers in both the layers.

Mechanics of Materials 139 (2019) 103199

Contents lists available at ScienceDirect

Mechanics of Materials

journal homepage: www.elsevier.com/locate/mechmat

Research paper

Enforcing shaping of thin gel sheets by anisotropic swelling

Daniele Battista[a], Michele Curatolo[a], Paola Nardinocchi[*,a]

Dipartimento di Ingegneria Strutturale e Geotecnica Sapienza Università di Roma, Roma I-00184, Italy

ARTICLE INFO

Keywords:
Thin sheets
Anisotropic swelling
Shaping problems

ABSTRACT

This paper investigates swelling-induced shaping in bilayer thin plates. Sphere-like and nearly developable shapes are realized and the ability to control a specific shaping, shifting from one shape to another, under anisotropic swelling is investigated. It is shown that reinforcing fibers can be crucial in controlling shaping under swelling and dramatically affect the characteristics of the final shapes.

1. Introduction

Swelling and shrinking of polymer gels have been widely used as driving forces to change the shape of materials. In response to different stimuli, such as variations in temperature or pH, the solvent uptake inside the cross–linked network can change resulting in reversible volumetric expansion or shrinkage. Most gels have a long response time, and the corresponding changes in shape are typically slow, generally due to local volume changes in the material corresponding to solvent uptake and release. Inhomogeneous swelling (shrinking) can determine dramatic changes in shape, especially in thin structures which can also quickly shift from one shape to another (Kim et al., 2012; Huang et al., 2016; Morales et al., 2016; Kim et al., 2017; Cangialosi et al., 2017; Battista et al., 2019). This has already been observed in different structures under different stimuli, such as in electro-responsive hydrogels (Jiang et al., 2019), in elastomers under oil extraction (Egunov et al., 2016), in liquid crystalline elastomers (Mostajeran et al., 2016; Kowalski et al., 2018), in shells under thermal expansion (Vu-Bac et al., 2018; 2019), and in biological structures (Aharoni et al., 2012; Oliver et al., 2016). In thin shells, in-plane and through-the-thickness inhomogeneous swelling, corresponding to in-plane or through-the-thickness inhomogeneous material, drive these changes in shape and produce domes and other surfaces from plates (Pezzulla et al., 2016; Stoychev et al., 2016; Pezzulla et al., 2017; van Manen et al. 2018).

Swelling in gel bodies can be viewed as an elastic growth, as it is the growth of a body due to the elastic stretching induced by solvent uptake of the polymeric network. A gel body stores elastic energy even if it freely swells from a dry state under no constraints and no loads. On the contrary, (inelastic) growth processes can determine changes in body shape without any storage of elastic energy, if growth deformations are compatible and realizable. So, in terms of energy, swelling and growth are quite different phenomena, especially when they come together (i.e. in active gels Bernheim-Groswasser et al., 2018; Bacca et al., 2019). There is a clear distinction between them and a full modeling of their interactions is crucial to accurately describe the combined processes (Curatolo et al., 2017a). Nevertheless, reduced models of growing plates and shells have often been used to study swelling in thin structures (Kim et al., 2012; Dias et al., 2011; Liu et al., 2016). The reason is that, for thin structures, the growth approach to the elastic problem, based on the multiplicative decomposition of the deformation gradient, yields simplified models which allow for semi-analytical solutions. However, the three-dimensional nature of the swelling processes, which are locally isotropic processes, as well as the differential capability to store energy with respect to growth processes, can deliver important differences in the realized steady and swollen configurations.

The topic of this paper is the swelling-driven bending of thin plates. The strategy used to achieve plate bending under swelling is based on bonding, one above the other, two layers with different elastic properties to realize a through-the-thickness inhomogeneous swelling. The amount of bending depends on the swelling mismatch between the layers; on the other side, the final shaping depends on different geometrical and mechanical factors. The goal is to discuss the shaping of bilayer plates using a three-dimensional fully coupled stress-diffusion nonlinear model presented in Lucantonio et al. (2013) and tested and discussed in Lucantonio et al. (2014), Nardinocchi et al. (2015), Nardinocchi et al. (2015), Curatolo et al. (2017b), Curatolo (2018), Curatolo and Nardinocchi (2018) and Curatolo et al. (2018).

We have largely investigated that issue with reference to bilayer naturally straight (Nardinocchi and Puntel, 2016; 2017a; 2017b) and naturally curved beams (Battista et al., 2019). We have also shown in Lucantonio et al. (2014) how our explicit analysis failed when the bilayer structure has aspect ratios that resemble plates more than beams. In this paper, we implement a set of numerical experiments by considering a large range of swelling mismatches between two isotropic/

* Corresponding author.
E-mail addresses: daniele.battista@uniroma1.it (D. Battista), michele.curatolo@uniroma3.it (M. Curatolo), paola.nardinocchi@uniroma1.it (P. Nardinocchi).

https://doi.org/10.1016/j.mechmat.2019.103199
Received 12 July 2019; Received in revised form 27 September 2019; Accepted 3 October 2019
Available online 07 October 2019
0167-6636/

anisotropic plates with different slenderness, aspect ratio and stiffness. Specifically, we test the capability of the structure to maintain the spherical shape or to bifurcate from it.

The results are also reviewed within the context of the non-euclidean plate theory (Pezzulla et al., 2017) and discussed with reference to a revised version of the bifurcation formula produced in Pezzulla et al. (2015).

Lastly, how shaping strategy can be controlled by generating bilayer plates which include anisotropic layers is shown. In this case, reinforcing fibers can be crucial in controlling shaping under swelling and dramatically affect the characteristics of the final shapes.

2. Steady states of swelling processes

Swelling is studied using the multiphysics model presented and discussed in Ref. Lucantonio et al. (2013) and successively refined in Refs. Lucantonio et al. (2014), Curatolo et al. (2017b), Curatolo and Nardinocchi (2018) and Curatolo et al. (2018). The key elements of the model are briefly reviewed.

Water–polymer mixture is modeled as a homogenized continuum body, allowing for a mass flux of the solvent (see also Refs. Hong et al., 2008; Hong et al., 2009; Zhang et al., 2009; Chester and Anand, 2010). The dry-reference state $\mathcal{G}_d$ of the gel is a plate, identified with the region of the Euclidean space $\mathcal{E}$ it occupies. The state variables of the model are the displacement field $\mathbf{u}_d$ from $\mathcal{G}_d$ and the molar water-concentration c_d per unit dry volume. The two state variables satisfy the following volumetric constraint

$$J_d = \det \mathbf{F}_d = \hat{J}_d(c_d) = 1 + \Omega c_d \,, \tag{2.1}$$

implying that any changes in volume of the gel is accompanied by an equivalent uptake or release of water content. Therein, $\mathbf{F}_d = \mathbf{I} + \nabla \mathbf{u}_d$ is the deformation gradient and Ω is the molar volume of the water.

As prescribed by the Flory–Rehner thermodynamic model (Flory and Rehner, 1943a; 1943b), the free energy ψ per unit dry-volume depends on $\mathbf{F}_d$ through an elastic component ψ_e, and on c_d through a polymer–water mixing energy ψ_m: $\psi = \psi_e + \psi_m$. We introduce a relaxed free–energy ψ_r, which includes the volumetric constraint, as $\psi_r(\mathbf{F}_d, c_d, p) = \psi_e(\mathbf{F}_d) + \psi_m(c_d) - p(J_d - \hat{J}_d(c_d))$ with the pressure p as the reaction to the volumetric constraint, which maintains the volume change J_d due to the displacement equal to the one due to solvent absorption or release $\hat{J}_d(c_d)$. The constitutive equation for the dry-reference stress $\mathbf{S}_d$ and for the chemical potential μ are consistently derived as

$$\mathbf{S}_d = \frac{\partial \psi_e}{\partial \mathbf{F}_d} - p\,\mathbf{F}_d^{\star} \quad \text{and} \quad \mu = \frac{\partial \psi_m}{\partial c_d} + p\,\Omega \,, \tag{2.2}$$

being $\mathbf{F}_d^{\star} = J_d\,\mathbf{F}_d^{-T}$. For isotropic gels, the elastic component ψ_e of the free energy takes a neo-Hookean form, whereas for anisotropic gels a further component has been added which accounts for the reinforcing effect of the fibres (Nardinocchi et al., 2015). The polymer–water mixing energy ψ_m always maintains the Flory–Huggins isotropic form. So, by introducing the unit vector field $\mathbf{e}$ which identifies the fiber direction field in transversely isotropic gels, we have:

$$\psi_e(\mathbf{F}_d) = \frac{G}{2}(\mathbf{F}_d{\cdot}\mathbf{F}_d - 3) \quad \text{or} \quad \psi_e(\mathbf{F}_d) = \frac{G}{2}(\mathbf{F}_d{\cdot}\mathbf{F}_d - 3) + \frac{G\gamma}{2}(\mathbf{F}_d\mathbf{e}{\cdot}\mathbf{F}_d\mathbf{e} - 1)^2 \,, \tag{2.3}$$

and

$$\psi_m(c_d) = \frac{\mathcal{R}T}{\Omega} h(c_d) \quad \text{with} \quad h(c_d) = \Omega\, c_d \log\frac{\Omega\, c_d}{1 + \Omega\, c_d} + \chi \frac{\Omega\, c_d}{1 + \Omega\, c_d} \,; \tag{2.4}$$

where G represents the shear modulus of the dry polymer, $\mathcal{R}$ represents the universal gas constant, T represents the temperature and χ represents the Flory parameter. However, the constitutive equation for the chemical potential does not change for isotropic/anisotropic gels, and is

$$\mu = \hat{\mu}(c_d) = \hat{\mu}(J_d) = \mathcal{R}\,T\left(\log\frac{J_d - 1}{J_d} + \frac{1}{J_d} + \frac{\chi}{J_d^2}\right), \tag{2.5}$$

the constitutive equations for the stress in the isotropic and anisotropic case are

$$\mathbf{S}_d = G\,\mathbf{F}_d - p\,\mathbf{F}_d^{\star} \quad \text{or} \quad \mathbf{S}_d = G\,\mathbf{F}_d + 2\,G\,\gamma\,(\mathbf{F}_d\mathbf{e}{\cdot}\mathbf{F}_d\mathbf{e} - 1)\mathbf{F}_d\mathbf{e} \otimes \mathbf{e} - p\,\mathbf{F}_d^{\star} \,. \tag{2.6}$$

Typically, thermodynamical issues drive the constitutive representation of the solvent flux $\mathbf{h}_d$ in terms of the gradient $\nabla\mu$ of the chemical potential as $\mathbf{h}_d = -\mathbf{M}(\mathbf{F}_d, c_d)\nabla(\hat{\mu}(c_d) + p\,\Omega)$ with the mobility tensor $\mathbf{M}(\mathbf{F}_d, c_d) = D/\mathcal{R}T\, c_d \mathbf{C}_d^{-1}$ and $\mathbf{C}_d = \mathbf{F}_d^T\mathbf{F}_d$ as a positive definite tensor depending on the diffusivity D of the polymer. Here, we only aim to characterize the stationary swollen states of thin bilayer structures, delivered by the equilibrium equations of the model in the form:

$$0 = \operatorname{div} \mathbf{S}_d \quad \text{and} \quad 0 = -\operatorname{div} \mathbf{h}_d \qquad \text{in} \quad \mathcal{G}_d \,. \tag{2.7}$$

In this study, they are supplemented by the boundary mechanical $\mathbf{S}_d\,\mathbf{m} = \mathbf{t}$ and chemical $\hat{\mu}(c_s) + p\,\Omega = \mu_e$ conditions on $\partial\mathcal{G}_d$, with the latter corresponding to an implicit condition on the concentration field c_s on $\partial\mathcal{G}_d$ controlled by assigning the external chemical potential μ_e.

It is worth noting that the mechanical problem, governed by the balance equation $(2.7)_1$ of forces, and the diffusion problem, governed by the balance equation $(2.7)_2$ of solvent mass, are coupled by the local volumetric constraint (2.1) between the two state variables of the full problem. A direct consequence of that constraint is the presence, in the equations (2.2), of the pressure term p which is the reaction to the volumetric constraint and represents a further coupling between mechanics and diffusion.

2.1. Swelling mismatch in bilayer structures

Bilayer plates bend under swelling due to the mismatch between the shear moduli and/or the Flory parameters of the two plate-like parts. The issue has already been largely discussed elsewhere (Armon et al., 2011; Erb et al., 2013; Lucantonio et al., 2014; Pezzulla et al., 2016; 2017), and can be described starting from the free-swelling solution of the stress-diffusion problem corresponding to a body which is embedded into a bath of assigned chemical potential μ_e. A homogeneous body attains a swollen stress-free state with $\mathbf{S}_d = \mathbf{0}$ and $\mathbf{h}_d = 0$, identified by the deformation gradient $\mathbf{F}_d = \lambda_o\mathbf{I}$ with the free-swelling stretch λ_o the solution of the equilibrium equation:

$$\mathcal{R}\,T\left(\log\frac{\lambda_o^3 - 1}{\lambda_o^3} + \frac{1}{\lambda_o^3} + \frac{\chi}{\lambda_o^6}\right) + \frac{G\Omega}{\lambda_o} = \mu_e \,. \tag{2.8}$$

Eq. (2.8) shows that the uniform swelling ratio λ_o is completely determined by the shear modulus G once the external chemical potential μ_e and the Flory parameter χ have been fixed.

When two bonded layers of different shear modulus swell into a homogeneous bath of assigned chemical potential, the mismatch between the uniform swelling ratios which would correspond to the two layers if each of them were free from the other, is one of the determinants of the bending intensity. It has been shown that, for $1/\lambda_o^3 \to 0$, the mismatch δ between the uniform swelling ratios λ_{ot} and λ_{ob} of the top and bottom layers, respectively, can be written as

$$\delta = \frac{\lambda_{ot}}{\lambda_{ob}} = \left(\frac{G_b}{G_t}\right)^{1/5} = \alpha^{-1/5} \quad \text{with} \quad \alpha = \frac{G_t}{G_b} \,. \tag{2.9}$$

When one of the two layers is unidirectionally fiber reinforced, the swelling mismatch between the two layers may be different along the fiber direction and in the transverse direction. Indeed, a homogeneous anisotropic body with fibers attains a swollen stress-free state with $\mathbf{S}_d = \mathbf{0}$ and $\mathbf{h}_d = 0$, identified by the deformation gradient

$\mathbf{F}_d = \lambda_{o\parallel}\,\mathbf{e}\otimes\mathbf{e} + \lambda_{o\perp}\check{\mathbf{I}}$ being $\lambda_{o\parallel}$ and $\lambda_{o\perp}$ the linear swelling ratios along the fiber direction $\mathbf{e}\otimes\mathbf{e}$ and in the orthogonal plane, respectively, and with $\check{\mathbf{I}} = \mathbf{I} - \mathbf{e}\otimes\mathbf{e}$. Moreover, the free-swelling stretches $\lambda_{o\parallel}$ and $\lambda_{o\perp}$ are solutions of the equilibrium equations:

$$\lambda_{o\perp}^2 = (1 + 2\gamma(\lambda_{o\parallel}^2 - 1))\lambda_{o\parallel}^2 \quad \text{and} \quad \frac{G\,\Omega}{\lambda_{o\parallel}} = \mu_e - \hat{\mu}(J_d)\,, \quad J_d = \lambda_{o\parallel}\lambda_{o\perp}^2\,. \tag{2.10}$$

Eq. (2.10)$_1$ delivers a representation of $\lambda_{o\perp}^2$ in terms of $\lambda_{o\parallel}^2$; by using it in (2.10)$_2$, we get the relation between $\lambda_{o\parallel}$ and the external chemical potential μ_e. It is worth noting that the isotropic free-swelling ratio λ_o always stays between $\lambda_{o\parallel}$ and $\lambda_{o\perp}$ for the same values of the other parameters:

$$\lambda_{o\parallel} < \lambda_o < \lambda_{o\perp}\,. \tag{2.11}$$

Hence, we can define differential swelling mismatches depending on fiber direction and on fiber position (within the top or bottom layer). As shown in Section 4, when anisotropic layers are included in the assembled structure, the shaping problems induced by the differential swelling mismatches raise some interesting questions.

3. Isotropic swelling of bilayer thin sheets

Realizing thin multilayered plates by bonding at least two layers with different elastic moduli, and with at least one of the two as a stimuli-responsive layer is a strategy to obtain plate bending in absence of mechanical actions. Under the stimulus, the mismatched response of the two layers delivers a strain gradient along the thickness which permits bending in the absence of mechanical actions.

We consider bilayer isotropic plates of thickness h and sides L_1 and L_2, with $h/L_\eta << 1$ ($\eta = 1, 2$). We assume the ratio β between the thickness h_t of the top layer and the thickness h of the plate fixed. Once embedded into a solvent bath, each layer swells to the extent its shear modulus and the bond with the other layer allows. The plate increases its thickness and, due to the swelling mismatch δ between the two layers, bends.

The problem is set within the stress-diffusion model illustrated in the Section 2 and the isotropic elastic energy is chosen in the form (2.4)$_1$. We are interested in the equilibrium solution of the problem and solve it by using `Stationary Solutor` in the finite element software COMSOL Multiphysics. A mesh composed of parallelepiped cells with at least six elements for each direction ius used as well as the stationary solver with the Newton nonlinear method to solve all the equations of the problem in a weak form. High order shape functions are also used. More specifically, we use quintic order Lagrange shape functions for the balance of forces and the balance of solvent mass. A quartic discontinuous Lagrange shape function is used for the Lagrangian multiplier of the volumetric constraint equation. Finally, the convergence is verified by testing different mesh sizes of mesh and by increasing the order of the shape functions. More details regarding the numerical implementation and validation of the model are given in the Appendix.

3.1. From flat to double-curved shapes

Analyses were performed by implementing a wide range of swelling tests keeping the aspect ratio AR = 1 of the plate fixed, that is, assuming $L_1 = L_2 = L$ (and L = 1cm), and changing both the slenderness h/L, in the interval (0.07, 0.2), and the ratio α in the interval (0.3,1). We also fixed $\beta = 0.6$.[1] A swelling mismatch $\delta = \lambda_{ot}/\lambda_{ob}$ corresponds to each α, it corresponds, due to the equation (2.9). In our tests, δ varies in the interval (1.3,1), determining a maximum differential strain $\varepsilon_{ot} - \varepsilon_{ob} \simeq 0.3$. The same swelling mismatch holds when the bottom layer (and, as a consequence assuming α as fixed, the top layer) is softer and softer. Finally, we also remark that both the layers in the following analyses are isotropic, that is, there are no fibers present.

For $G_b = 10^5$Pa and $G_b = 10^7$Pa, Fig. 1 shows the increase in bending of a plate of slenderness $h/L = 0.07$, corresponding to the decrease in α: for $\alpha = 1$, the plate is homogeneous and the swelling realizes a homothety with the plate maintaining its flat shape. For $\alpha \neq 1$ a sphere-like shape is realized, with equal principal curvatures and the Gaussian curvature $K^\star$, evaluated at the center of the middle surface, increasing for α decreasing, corresponding to an increase in the swelling mismatch. We can see that, at $\alpha = 0.3$, we get a swelling mismatch $\delta = 1.3$ for both the plates, even if, it corresponds to free-swelling stretches λ_{ob} and λ_{ot} equal to 2.75 and 3.5, for $G_b = 10^5$Pa, and to free-swelling stretches λ_{ob} and λ_{ot} equal to 1.32 and 1.68, for $G_b = 10^7$Pa. Fig. 1 also shows the plate configurations at the three points 1-2-3 corresponding to $\alpha = 1$, 0.6, 0.3, respectively, highlighted in the plot of Fig. 1, corresponding to a bottom layer with $G_b = 10^5$Pa.

The sphere-like shape still holds when the slenderness h/L changes in the interval (0.07,0.2). Fig. 2 shows the final configurations of the plates corresponding to $\alpha = 0.7$, that is to a swelling mismatch $\delta \simeq 1$, and to a shear modulus of the bottom layer equal to $G_b = 10^5$. We still get a double-curved surface even if the volumetric change J_d and the swelling stretches of the two layers are very high.

3.2. From spherical to nearly developable shapes

Within the wide range of swelling tests we investigated, the aspect ratio of the bilayer plate would appear to be a determinant of the final shape realized by the plate. Indeed, under the same conditions previously presented regarding the materials of the two layers, and for a slenderness ratio within the interval explored above, we found a completely different deformation regime. $L_2 = L$ remains fixed and L_1 changes so as to cover a range of aspect ratios AR between 1 and 0.1. We ran several simulations with different meshes, for every AR $\neq$ 1, fixing $G_b = 10^7$Pa, $\alpha = 0.7$, and $h/L = 0.07$.

The shape of the bilayer plate bifurcates from the spherical shape at AR = 1, as it is shown in Fig. 3 where the values of the principal curvatures κ_1 (solid line) and κ_2 (dashed line), evaluated at the center of the middle surface, are represented versus `AR`. The two lines start diverging when AR $\neq$ 1; they remain close up to a critical AR value (about AR = 0.2 in the figure). Fig. 3 also shows that a cylindrical shape, with zero Gaussian curvature $K^* = \kappa_1\kappa_2$, is attained when AR is very small; otherwise, dome-like shapes with positive Gaussian curvatures are realized.

3.3. Bifurcation thresholds

The shaping discussed above can be reviewed within the modeling presented in Pezzulla et al. (2016). The non euclidean plate theory was used to derive the threshold between the deformative regimes of bilayer plates delivering double-curved and nearly developable shapes, when one of the two layers in-plane grows with respect to the other (in-plane growth mismatch). In that case, the threshold is represented in terms of the natural curvature κ_o of the plate. Having defined the dimensionless natural curvature corresponding to the bifurcation as $\bar{\kappa}_{ob}$, it is shown that[2]

$$\bar{\kappa}_{ob} = \left(\frac{20 + 14\sqrt{2}}{27}\right)^{1/2}\epsilon^2\,, \quad \epsilon = \frac{h}{\mathcal{S}}\,, \tag{3.12}$$

with the shape factor $\mathcal{S} = (2/9\int r^4 dA/A)^{1/4}$ and $\bar{\kappa}_{ob} = \kappa_{ob}h$. At that value of natural curvature, the energy of a spherical cap coincides with the energy of an isometric state, and bifurcation occurs. Taking into

[1] It has been shown in Lucantonio et al. (2014) how for the same values of all the other parameters, $\beta = 0.6$ determines the maximum value of curvature in bilayer beams.

[2] See equation (9) in Pezzulla et al. (2016).

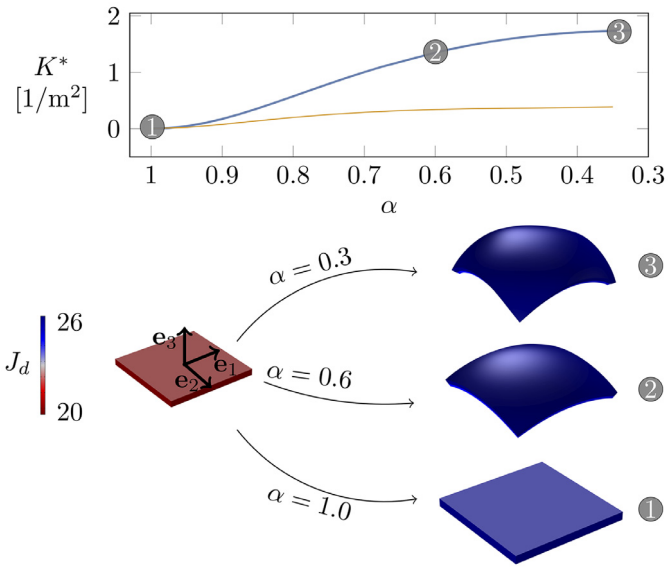

Fig. 1. Top: Gaussian curvature $K^\star$ versus shear moduli ratio α for a square plate with slenderness $h/L = 0.07$ and shear modulus of the bottom layer $G_b = 10^5$Pa (blue line) and $G_b = 10^7$Pa (yellow line). Bottom: Gel configurations at the three points 1-2-3 corresponding to $\alpha = 1, 0.6, 0.3$, respectively, highlighted in the top plot. Colour code corresponds to the volumetric change J_d, which is related to the amount of solvent uptake. (For interpretation of the references to colour in this figure legend, the reader is referred to the web version of this article.)

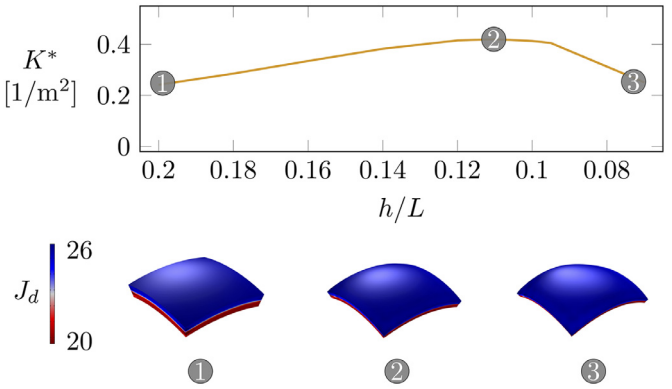

Fig. 2. Top: Gaussian curvature $K^\star$ versus slenderness h/L for a square plate with ratio $\alpha = 0.7$ and shear modulus of the bottom layer $G_b = 10^5$Pa. Bottom: Gel configurations at the three points 1-2-3 corresponding to $h/L = 0.2, 0.11, 0.07$, respectively, highlighted in the top plot. Colour code corresponds to the volumetric change J_d, which is related to the amount of solvent uptake.

account the observations made in Pezzulla et al. (2017), where the non euclidean plate theory has been slightly revised to comprehend bilayer plate with isotropically growing layers, a revised version of the above formula can be produced, with ϵ^2 changed in

$$\tilde{\epsilon}^2 = \lambda_{ob} f(\alpha, \beta)\epsilon^2, \quad f(\alpha, \beta) = 1 - \beta + \beta\alpha^{-1/5}. \tag{3.13}$$

We can easily evaluate $\tilde{\epsilon}$ and, hence, κ_{ob} for our plates. We can also evaluate κ_o by cutting a bilayer beam out of the bilayer plate and by identifying the natural curvature κ_o with the curvature realized by that beam through the explicit formula produced in Lucantonio et al. (2014). Focus is now given to the plates whose steady curved shapes are represented in Fig. 3. Fixed G_b, α, h/L and L, the natural curvature κ_o does not depend on the aspect ratio and, using the equations (4.14)-(4.16) in Lucantonio et al. (2014), its value is 69.5m^{-1}. On the contrary, the bifurcation natural curvature κ_{ob} depends

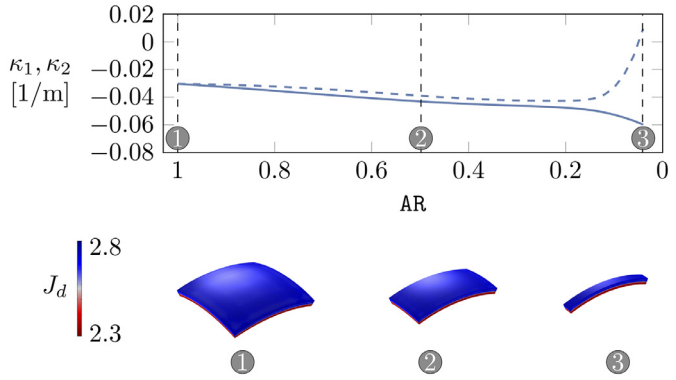

Fig. 3. Top: Principal curvatures κ_1 (solid line) and κ_2 (dashed line) versus the aspect ratio AR for a bilayer plate with slenderness $h/L = 0.07$, shear modulus of the bottom layer $G_b = 10^7$Pa, and $\alpha = 0.7$. Bottom: Gel configurations at the three points 1-2-3 corresponding to AR = 1, 0.5, 0.1, respectively, highlighted in the top plot. Colour code corresponds to the volumetric change J_d, which is related to the amount of solvent uptake.

on the aspect ratio by means of the shape factor $\mathcal{S}$ and decreases from 55.71m^{-1} to 22.85m^{-1} going from AR = 0.1 AR = 1, as the area of the plate descreases. This means that $\kappa_o > \kappa_{ob}$ when AR $\neq 1$ and, as Fig. 3 shows, bifurcation from a sphere has already occurred. However, $\kappa_o > \kappa_{ob}$ also for squared plates which assume spherical shapes in the range of swelling tests we investigated.

As is stressed in the Conclusions, the poor matching of the two approaches requires further investigation, starting from both sides: numerical tests via a fully three-dimensional stress-diffusion model and an analytical approach via energetic issues which take into account the characteristics of the swelling deformation processes.

4. Enforcing cylindrical shaping by anisotropic swelling

A controlled assembly of isotropic and anisotropic gel layers which admits differential swelling mismatches in different directions considerably changes the shaping scenario. Moreover, the architecture of the assembly determines the shaping of the structure. Well-known examples exist in the plant world. Typically, plant cell walls are composites of stiff cellulose fibrils embedded in a compliant and highly swellable matrix consisting of hemicelluloses. Different alignments of cellulose fibrils in different layers of the composite produce different architectures, and plants can control the swelling(shrinking)–driven deformation of cells through an elaborated adjustment of cell wall architecture (Burgert and Fratzl, 2009; Ruggeberg and Burgert, 2015).

In this section, our investigation is continued, moving towards more complex architectures. First, we consider the assembly of two gel layers, with a softer top than the bottom ($\alpha < 1$), and the reinforcing fibers in the $\mathbf{e}_2$ direction which are homogeneously distributed in the softer top layer (architecture T), in the harder bottom layer (architecture B), and in both (architecture TB). The three architectures are identified with three different marks in the following figures.

We consider bilayer plates with $G_b = 10^5$Pa, $\alpha = 0.7$, $\beta = 0.6$ and $h/L = 0.007$ and different aspect ratios; the three described architectures are characterized by different swelling problems.

For squared plates, Fig. 4 (left column) shows that embedding fibers in just one layer favours cylindrical shaping. When the softer top layer is reinforced (top left), stretching in the fiber direction is too expensive and the plate contracts at the top layer thus generating a positive κ_2 curvature, as shown in Fig. 5 (see the dashed blue line), with the other curvature κ_1 almost null. On the contrary, when the harder bottom layer is reinforced (middle left), the plate contracts at the bottom layer thus producing a negative κ_2 curvature as shown in Fig. 5 (see the dashed yellow line). As before, the other curvature κ_1 is almost null. In this case, the steady shape resembles a cylindrical tube as the lower shear

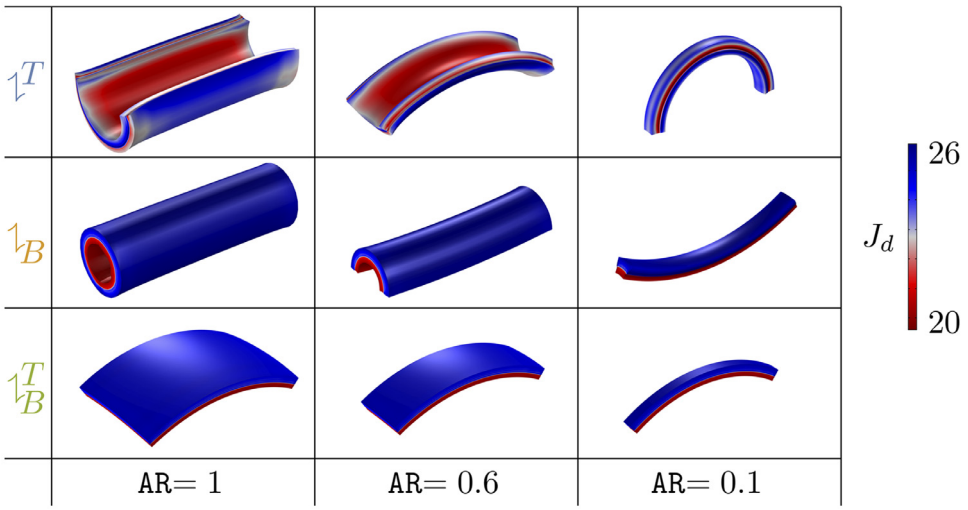

Fig. 4. Morphological phase diagrams of emerging surface patterns from numerical simulations corresponding to architectures T, B, TB (top, middle, bottom rows) and to aspect ratios AR = 1, 0.6, 0.1 (left, middle, right columns). Colour code represents the volume change J_d.

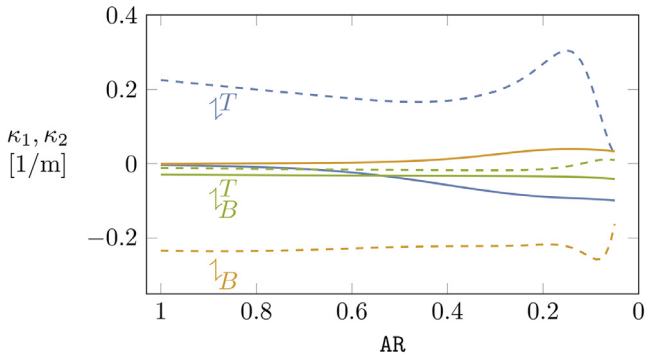

Fig. 5. Principal curvatures κ_1 (solid lines) and κ_2 (dashed lines) of bilayer plates assemblied in the architectures T, B, TB (blue, yellow and green lines) versus the aspect ratio AR. (For interpretation of the references to colour in this figure legend, the reader is referred to the web version of this article.)

modulus of the top layer allows there large stretches in the circumferential (fiber) direction. Two anisotropic layers sharing the fiber direction almost fail to bend in the fiber direction, as shown in Fig. 4 (bottom left). Moreover, the anticlastic effect, that is, the difference between the absolute values of the principal curvatures, is reduced with respect to that observed when only one layer is fiber reinforced. This effect can be seen in Fig. 5 for both AR = 1 and AR = 0.6.

When the aspect ratio is small, the plates almost resemble beams. In this case, putting fibers in the softer top or in the harder bottom layer produces shapes with the two principal curvatures of the opposite sign, that is, an anticlastic curvature different from zero. Moreover, going from the beam-like plate with the reinforced top layer, Fig. 4 (top right), to the other, Fig. 4 (middle right), the signs of both the principal curvatures change. Hence, even in beam-like plates, fibers can greatly affect the steady shape realized under swelling by the structure.

5. Conclusions

The behaviour of bilayer thin gel sheets under swelling has been investigated using a three-dimensional model which accounts for large deformations and for the contribution of the mixing energy to the total potential energy. Specifically, attention was focused on the steady shapes realized under swelling and on how these shapes can be mastered. The plate aspect ratio has a key role in determining the shape, as already noted for different stimuli-responsive plates in other studies. However, the difference between the elastic properties of the two layers to achieve different shapes is less important. We showed as reinforcing fibers can be crucial to change this last statement. A better enforcing of cylinder-like shapes is observed when fibers are inserted in only one rather than two layers. Finally, a larger suppression of the anticlastic curvature was observed by inserting fibers in both layers.

The results of the large number of swelling tests presented here propose a few challenging issues to be considered in the near future, possibly through a semi–analytic approach. This would enhance our understanding of the role of the different quantities used in this study, such as the anisotropic swelling mismatch and the anticlastic effect.

In our opinion, the effectiveness of the reduced models of growing plates in predicting final steady shapes, when three-dimensional elastic growth (swelling) is involved, needs to be addressed. We noted how, also accounting for the observations made in recent papers, some results borrowed from the non euclidean plate theory can not be applied in the present context. As noted in Hanna (2019) and Wood and Hanna (2019), the choice of elastic energies for thin plates and shells is an unsettled issue and the difference between stretching and bending modes may have important consequences for more recent modeling of soft matter, especially when large deformations are expected.

Declarations of Competing Interest

None.

Acknowledgments

The work is supported by MIUR (the Italian Ministry of University and Research) through the Project PRIN2017 (N. 2017KL4EF3) Mathematics of active materials from mechanobiology to smart devices. D.B. and M.C. acknowledge the Italian National Group of Mathematical Physics (GNFMNdAM) for support.

Appendix A. Numerical implementation

Our finite element model solves the balance equations (2.7) together with the volumetric constraint $J_d = \hat{J}_d(c_d)$ in integral form (weak form). Therein, the problem is formulated as follows: find $\mathbf{u}_d$, c_d and p such that, for all test fields $\tilde{\mathbf{u}}_d$, $\tilde{c}_d$, and $\tilde{p}$, it holds

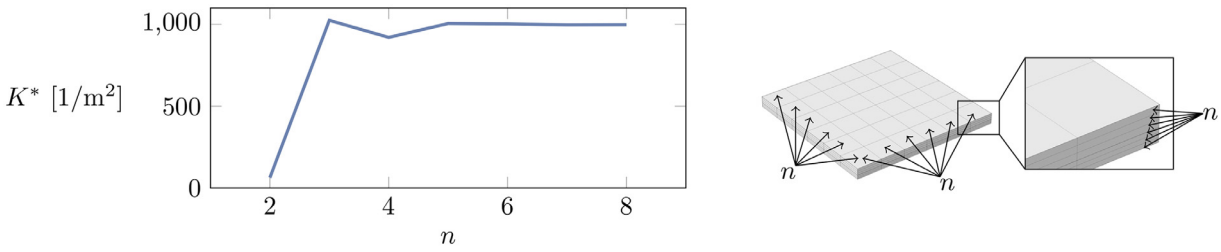

Fig. 6. Validation test of the numerical implementation. Gaussian curvature K^* at the center of the plate versus the number n of parallelepiped elements (left). Cartoon showing the discretization of the three-dimensional plate by parallelepiped elements (right).

$$0 = \int_{\mathcal{G}_d} (-\mathbf{S}_d \cdot \nabla \tilde{\mathbf{u}}_d + \mathbf{h}_d \cdot \nabla \tilde{c}_d + (J_d - \hat{J}_d(c_d)) \cdot \tilde{p}) \, , \tag{5.14}$$

where the representation forms introduced in Section 2 for the stress $\mathbf{S}_d$ and the flux $\mathbf{h}_d$ hold. As far as boundary conditions are concerned, we assume zero tractions and assign a displacement $\bar{\mathbf{u}}_d$ on the boundary that eliminates any rigid motion without generating reaction forces. On the other hand, we control the concentration c_s of the solvent on the boundary in an implicit way assuming that the chemical potential field μ there must be equal at all times to the chemical potential μ_e of the bath; the corresponding nonlinear implict equation is set in a weak form as

$$0 = \int_{\partial \mathcal{G}_d} [\hat{\mu}(c_s) + p\,\Omega - \mu_e] \cdot \tilde{c}_s \, . \tag{5.15}$$

Then, the full problem can be reformulated as follows: find $\mathbf{u}_d$, c_d, p and c_s such that, for any test functions $\tilde{\mathbf{u}}_d$, $\tilde{c}_d$, $\tilde{p}$ and $\tilde{c}_s$ Eqs. (5.14)–(5.15) hold.

The robustness and the accuracy of the numerical model are tested for a different number n of parallelepiped elements along the three sides of a bilayer plate characterized by the following parameters: $\alpha = 0.7$, $h/L = 0.07$, $\beta = 0.6$ and $G_b = 10^7$ Pa (see Fig. 6). The Gaussian curvature K^* at the center of the plate is evaluated; it reaches a stable value for $n \geq 5$. The degrees of freedom go from 7000 for $n = 2$ to 350000 for $n = 8$. In all the simulations presented in this paper, $n = 6$ parallelepiped elements are used. Due to the geometry of the bilayer bodies here investigated, which do not have any curved parts, parallelepiped elements are always preferred to tetrahedral elements to discretized the three-dimensional body. The convergence of the model is always assured with quintic order Lagrange shape functions for the balance of forces and solvent mass and with a quartic discontinuous Lagrange shape function for the Lagrangian multiplier of the volumetric constraint equation. It is worth noting that high orders of shape functions are also mandatory to obtain a good accuracy as both the dependent variables $\mathbf{u}_d$ and c_d in the balance laws have second spatial derivatives. On the other hand, lower orders of shape functions, especially when huge deformation are involved, do not assure the convergence of the problem.

References

Aharoni, H., Abraham, Y., Elbaum, R., Sharon, E., Kupferman, R., 2012. Emergence of spontaneous twist and curvature in non-euclidean rods: application to Erodium plant cells. Phys. Rev. Lett. 108, 238106.

Armon, S., Efrati, E., Kupferman, R., Sharon, E., 2011. Geometry and mechanics in the opening of chiral seed pods. Science 333 (6050), 1726–1730. https://doi.org/10.1126/science.1203874. http://www.sciencemag.org/content/333/6050/1726.abstract

Bacca, M., Saleh, O.A., McMeeking, R.M., 2019. Contraction of polymer gels created by the activity of molecular motors. Soft Matter 15, 4467–4475. https://doi.org/10.1039/C8SM02598C. https://doi.org/10.1039/C8SM02598C

Battista, D., Curatolo, M., Nardinocchi, P., 2019. Swelling-induced eversion and flattening in naturally curved gel beams. Int. J. Mech. Sci. 161–162, 105071.

Bernheim-Groswasser, A., Gov, N.S., Safran, S.A., Tzlil, S., 2018. Living matter: mesoscopic active materials. Adv. Mater. 30 (41), 1707028. https://doi.org/10.1002/adma.201707028. https://onlinelibrary.wiley.com/doi/abs/10.1002/adma.201707028

Burgert, I., Fratzl, P., 2009. Actuation systems in plants as prototypes for bioinspired devices. Philos. Trans. R. Soc. A 367 (1893), 1541–1557. https://doi.org/10.1098/rsta.2009.0003. https://royalsocietypublishing.org/doi/abs/10.1098/rsta.2009.0003

Cangialosi, A., Yoon, C., Liu, J., Huang, Q., Guo, J., Nguyen, T.D., Gracias, D.H., Schulman, R., 2017. Dna sequence–directed shape change of photopatterned hydrogels via high-degree swelling. Science 357 (6356), 1126–1130. https://doi.org/10.1126/science.aan3925. https://science.sciencemag.org/content/357/6356/1126

Chester, S.A., Anand, L., 2010. A coupled theory of fluid permeation and large deformations for elastomeric materials. J. Mech. Phys. Solids 58 (11), 1879–1906. https://doi.org/10.1016/j.jmps.2010.07.020. http://www.sciencedirect.com/science/article/pii/S0022509610001493

Curatolo, M., 2018. Effective negative swelling of hydrogel-solid composites. Extreme Mech. Lett. 25, 46–52.

Curatolo, M., Gabriele, S., Teresi, L., 2017. Swelling and growth: a constitutive framework for active solids. Meccanica 52 (14), 3443–3456. https://doi.org/10.1007/s11012-017-0629-x. https://doi.org/10.1007/s11012-017-0629-x

Curatolo, M., Nardinocchi, P., 2018. Swelling-induced bending and pumping in homogeneous thin sheets. J. Appl. Phys. 124 (8), 085108. https://doi.org/10.1063/1.5043580.

Curatolo, M., Nardinocchi, P., Puntel, E., Teresi, L., 2017. Transient instabilities in the swelling dynamics of a hydrogel sphere. J. Appl. Phys. 122 (14), 145109. https://doi.org/10.1063/1.5007229.

Curatolo, M., Nardinocchi, P., Teresi, L., 2018. Driving water cavitation in a hydrogel cavity. Soft Matter 14, 2310–2321. https://doi.org/10.1039/C8SM00100F.

Dias, M., Hanna, J.A., Santangelo, C., 2011. Programmed buckling by controlled lateral swelling in a thin elastic sheet. Phys. Rev. E Stat. Nonlinear Soft Matter Phys. 84, 036603. https://doi.org/10.1103/PhysRevE.84.036603.

Egunov, A.I., Korvink, J.G., Luchnikov, V.A., 2016. Polydimethylsiloxane bilayer films with an embedded spontaneous curvature. Soft Matter 12, 45–52. https://doi.org/10.1039/C5SM01139F.

Erb, R.M., Sander, J.S., Grisch, R., Studart, A., 2013. Self-shaping composites with programmable bioinspired microstructures. Nat. Commun. 4 (10), 1712. https://doi.org/10.1038/ncomms2666.

Flory, P.J., Rehner, J., 1943a. Statistical mechanics of cross-linked polymer networks I. Rubberlike elasticity. J. Chem. Phys. 11 (11), 512–520. https://doi.org/10.1063/1.1723791.

Flory, P.J., Rehner, J., 1943b. Statistical mechanics of cross-linked polymer networks II. Swelling. J. Chem. Phys. 11 (11), 521–526. https://doi.org/10.1063/1.1723792.

Hanna, J.A., 2019. Some observations on variational elasticity and its application to plates and membranes. Zeitschrift für angewandte Mathematik und Physik 70 (3), 76. https://doi.org/10.1007/s00033-019-1122-2.

Hong, W., Liu, Z., Suo, Z., 2009. Inhomogeneous swelling of a gel in equilibrium with a solvent and mechanical load. Int. J. Solids Struct. 46 (17), 3282–3289. https://doi.org/10.1016/j.ijsolstr.2009.04.022. http://www.sciencedirect.com/science/article/pii/S0020768309001899

Hong, W., Zhao, X., Zhou, J., Suo, Z., 2008. A theory of coupled diffusion and large deformation in polymeric gels. J. Mech. Phys. Solids 56 (5), 1779–1793. https://doi.org/10.1016/j.jmps.2007.11.010. http://www.sciencedirect.com/science/article/pii/S0022509607002244

Huang, H., Petruska, A.J., Sakar, M.S., Skoura, M., Ullrich, F., Zhang, Q., Pan, S., Nelson, B.J., 2016. Self-folding hydrogel bilayer for enhanced drug loading, encapsulation, and transport. 2016 38th Annual International Conference of the IEEE Engineering in Medicine and Biology Society (EMBC). pp. 2103–2106. https://doi.org/10.1109/EMBC.2016.7591143.

Jiang, H., Fan, L., Yan, S., Li, F., Li, H., Tang, J., 2019. Tough and electro-responsive hydrogel actuators with bidirectional bending behavior. Nanoscale 11, 2231–2237. https://doi.org/10.1039/C8NR07863G.

Kim, J., Hanna, J.A., Byun, M., Santangelo, C.D., Hayward, R.C., 2012. Designing responsive buckled surfaces by halftone gel lithography. Science 335 (6073), 1201–1205. https://doi.org/10.1126/science.1215309.

Kim, J., Kim, C., Song, Y., Jeong, S.-G., Kim, T.-S., Lee, C.S., 2017. Reversible self-bending soft hydrogel microstructures with mechanically optimized designs. Chem. Eng. J.

321, 384–393. https://doi.org/10.1016/j.cej.2017.03.125. http://www.sciencedirect.com/science/article/pii/S1385894717304928
Kowalski, B.A., Mostajeran, C., Godman, N.P., Warner, M., White, T.J., 2018. Curvature by design and on demand in liquid crystal elastomers. Phys. Rev. E 97, 012504.
Liu, Y., Genzer, J., Dickey, M.D., 2016. 2d or not 2d: shape-programming polymer sheets. Prog. Polym. Sci. 52, 79–106. https://doi.org/10.1016/j.progpolymsci.2015.09.001. http://www.sciencedirect.com/science/article/pii/S0079670015001021
Lucantonio, A., Nardinocchi, P., Pezzulla, M., 2014. Swelling-induced and controlled curving in layered gel beams. Proc. R. Soc. A 470 (2171). https://doi.org/10.1098/rspa.2014.0467.
Lucantonio, A., Nardinocchi, P., Teresi, L., 2013. Transient analysis of swelling-induced large deformations in polymer gels. J. Mech. Phys. Solids 61 (1), 205–218. https://doi.org/10.1016/j.jmps.2012.07.010.
Lucantonio, A., Roche, M., Nardinocchi, P., Stone, H.A., 2014. Buckling dynamics of a solvent-stimulated stretched elastomeric sheet. Soft Matter 10, 2800–2804. https://doi.org/10.1039/C3SM52941J.
van Manen, T., Janbaz, S., Zadpoor, A.A., 2018. Programming the shape-shifting of flat soft matter. Mater. Today 21 (2), 144–163. https://doi.org/10.1016/j.mattod.2017.08.026. http://www.sciencedirect.com/science/article/pii/S1369702117302237
Morales, D., Bharti, B., Dickey, M.D., Velev, O.D., 2016. Bending of responsive hydrogel sheets guided by field-assembled microparticle endoskeleton structures. Small 12 (17), 2283–2290. https://doi.org/10.1002/smll.201600037. https://onlinelibrary.wiley.com/doi/abs/10.1002/smll.201600037
Mostajeran, C., Warner, M., Ware, T.H., White, T.J., 2016. Encoding gaussian curvature in glassy and elastomeric liquid crystal solids. Proc. Roy. Soc. A472, 20160112.
Nardinocchi, P., Pezzulla, M., Teresi, L., 2015. Steady and transient analysis of anisotropic swelling in fibered gels. J. Appl. Phys. 118 (24). https://doi.org/10.1063/1.4938737. http://scitation.aip.org/content/aip/journal/jap/118/24/10.1063/1.4938737
Nardinocchi, P., Pezzulla, M., Teresi, L., 2015. Anisotropic swelling of thin gel sheets. Soft Matter 11, 1492–1499. https://doi.org/10.1039/C4SM02485K.
Nardinocchi, P., Puntel, E., 2016. Finite bending solutions for layered gel beams. Int. J. Solids Struct. 90, 228–235. https://doi.org/10.1016/j.ijsolstr.2016.02.026.
Nardinocchi, P., Puntel, E., 2017a. Swelling-induced wrinkling in layered gel beams. Proc. R. Soc. A 473 (2207), 20170454. https://doi.org/10.1098/rspa.2017.0454. https://royalsocietypublishing.org/doi/abs/10.1098/rspa.2017.0454
Nardinocchi, P., Puntel, E., 2017b. Unexpected hardening effects in bilayer gel beams. Meccanica 52 (14), 3471–3480. https://doi.org/10.1007/s11012-017-0635-z. https://doi.org/10.1007/s11012-017-0635-z
Oliver, K., Seddon, A., Trask, R.S., 2016. Morphing in nature and beyond: a review of natural and synthetic shape-changing materials and mechanisms. J. Mater. Sci. 51 (24), 10663–10689. https://doi.org/10.1007/s10853-016-0295-8.
Pezzulla, M., Shillig, S.A., Nardinocchi, P., Holmes, D.P., 2015. Morphing of geometric composites via residual swelling. Soft Matter 11, 5812–5820. https://doi.org/10.1039/C5SM00863H.
Pezzulla, M., Smith, G.P., Nardinocchi, P., Holmes, D.P., 2016. Geometry and mechanics of thin growing bilayers. Soft Matter 12, 4435–4442. https://doi.org/10.1039/C6SM00246C.
Pezzulla, M., Stoop, N., Jiang, X., Holmes, D.P., 2017. Curvature-driven morphing of non-euclidean shells. Proc. R. Soc. A 473 (2201), 20170087. https://doi.org/10.1098/rspa.2017.0087. https://royalsocietypublishing.org/doi/abs/10.1098/rspa.2017.0087
Ruggeberg, M., Burgert, I., 2015. Bio-inspired wooden actuators for large scale applications. PLoS ONE 10, e0120718.
Stoychev, G., Guiducci, L., Turcaud, S., Dunlop, J.W.C., Ionov, L., 2016. Hole-programmed superfast multistep folding of hydrogel bilayers. Adv. Funct. Mater. 26 (42), 7733–7739. https://doi.org/10.1002/adfm.201602394. https://onlinelibrary.wiley.com/doi/abs/10.1002/adfm.201602394
Vu-Bac, N., Duong, T.X., Lahmer, T., Areias, P., Sauer, R.A., Park, H.S., Rabczuk, T., 2019. A NURBS-based inverse analysis of thermal expansion induced morphing of thin shells. Comput. Methods Appl. Mech. Eng. 350, 480–510.
Vu-Bac, N., Duong, T.X., Lahmer, T., Zhuang, X., A. Sauer, R., S. Park, H., Rabczuk, T., 2018. A NURBS-based inverse analysis for reconstruction of nonlinear deformations of thin shell structures. Comput. Methods Appl. Mech. Eng. 331, 427–455.
Wood, H.G., Hanna, J.A., 2019. Contrasting bending energies from bulk elastic theories. Soft Matter 15, 2411–2417. https://doi.org/10.1039/C8SM02297F.
Zhang, J., Zhao, X., Suo, Z., Jiang, H., 2009. A finite element method for transient analysis of concurrent large deformation and mass transport in gels. J. Appl. Phys. 105 (9), 093522. https://doi.org/10.1063/1.3106628.

Let us consider the experiment proposed in Section 4.6 on shrinking naturally curved polymer beams due to oil extraction. The same experiment can be carried out by increasing the aspect ratio of the beams, thus obtaining open cylindrical bilayer surfaces consisting of a layer of PDMS and a layer of PDMS mixed with silicone oil. If the oil is placed in the inner layer of the cylinder, the shell will simply increase its curvature as the oil is extracted. On the contrary, more interesting is the case in which the oil is in the outer layer; here the cylinder will unroll and, eventually, evert and bend along a direction orthogonal to the initial one.

In I, the shape-shifting of cylindrical shells due to oil extraction is studied numerically within the context of three-dimensional finite elasticity with distortion for an elastically incompressible neo-Hookean material (see Section 4.2). The study is focused on the equilibrium states attained by the cylinders after the complete extraction of oil, the latter modeled as a spherical bulk contraction $\mathbf{F}_o = \lambda_o \mathbf{I}$, with $\lambda_o = (1 - f)^{1/3} < 1$ as a function of the fraction of oil f. A campaign of numerical experiments is conducted by parametrically varying the aspect ratio ($\mathtt{AR} = 0.1, 0.5, 1$) and the bulk contraction, as if simulating different initial oil fractions in the mixing between PDMS and oil. The results are resumed in the morphological diagram of Figure I-4 (Figure 25), where the bulk contraction(oil fraction) decreases(increases) from left to right, starting from the initial configuration (first column) corresponding to $\lambda_o = 1 (f = 0)$. It is shown that, as expected, to decreasing values of λ_o the bilayer beam, corresponding to $\mathtt{AR} = 0.1$, undergoes curvature reduction, flattening at $\lambda_o = \lambda_o^\star (f = f^\star)$ and eversion. When the aspect ratio increases ($\mathtt{AR} = 0.5, 1$), the same value $\lambda_o^\star$ (third column), corresponding to the flattened beam, identifies everted cylindrical shells with the principal curvature axes switched with respect to the reference state. This result is also shown in Figure I-5, where the normalized Gaussian curvature K, evaluated at the center of the middle surface, vanishes at $\lambda_o = 1$ and $\lambda_o = \lambda_o^\star$ for any $\mathtt{AR}$. When $\lambda_o^\star < \lambda_o < 1$, that is $0 < f < f^\star$, the beam decreases its curvature and flattens, while the cylindrical shells morph into cylindrical shells with the axes of principal curvatures switched, passing through saddle-like shapes (second column). By further increasing the fraction of extracted oil above $f^\star$, the beam everts, the shell with $\mathtt{AR} = 1$ continues to bend along the direction orthogonal to the initial one, and the shell with $\mathtt{AR} = 0.5$ attains a dome-like shape (fourth and fifth columns).

Finally, a parametric analysis reducing the thickness of a cylindrical shell with $\mathtt{AR} = 1$ is carried out and shows that the range of λ_o which allows to get saddle-like shapes decreases as the cylindrical shell decreases its thickness (see Figure I-6).

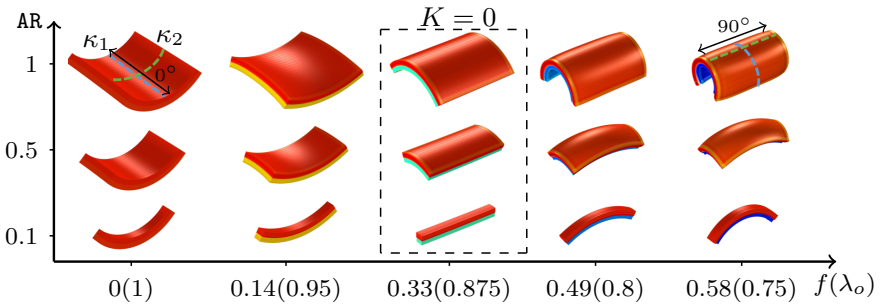

Figure 25: Morphological diagram of a naturally curved beam (bottom) and cylindrical shells with different aspect ratios (top and centers) due to a bulk contraction λ_o of the outer layer, corresponding to a complete extraction of an initial fraction of oil f. From I.

7

CONCLUSION AND FUTURE STUDIES

Soft active materials are a valid resource for many fields of application, in particular the biomedical one, where it is often necessary to induce deformation of a device without the application of loads. Programming the control of such structures is challenging. The study of theoretical models which describe the shape-morphing is important, at least in the preliminary design phase. This allows not only to experiment virtually the deformation process, but also to access simplified and applicable explicit formulas.
This work aimed to provide some original tools, both analytical and numerical, useful for designing the shape change of soft active sheets. Firstly, as regards growing bilayer beams, through an energetic approach explicit formulas for the curvature and the middle axis stretch have been computed, using both the Biot and Green deformation measures. The main differences between the formulas deriving from the two measures have been highlighted.
Then, we focused on the study of bilayer gel structures, in which the fluid induces bending through local variations in volume. Three distinct bending processes have been explored:

1. the bending induced by differential swelling between two layers with different elastic moduli;

2. the bending induced by the extraction of the solvent contained in a layer stacked on a passive layer;

3. the bending induced by a through-the-thickness diffusion of the solvent.

The first and third has been studied with a continuous stress-diffusion model, while the second within a context of finite elasticity with distortions.
The first bending process has been applied to the study of initially dry naturally curved gel beams and rectangular gel plates. About the beams, the swelling-induced eversion and flattening has been discussed through exact numerical models and appropriate explicit formulas. A good agreement of the two approaches in terms of the expected final curvature has been found. The results show that eversion and flattening of an initial curved beam can be realized for specific ratios between the thicknesses and the elastic moduli of the layers. The explicit formulas include the formula of an initially flat bilayer gel beam derived in [47], the Timoshenko formula for bimetals within the limits of slightly curvature of the original dry beam and small

deformations [87], an additive-type formula like the one derived in [67], and a simplified formula for nearly-homogeneous beams.
As for the plates, the swelling-induced shaping from sphere-like to nearly developable shapes has been investigated. Specifically, attention was focused on the steady shapes and on how they can ben mastered. In the latter, the final shape depends on several geometrical and mechanical factors. Reinforcing fibers can be crucial in controlling shaping under swelling and greatly influence the characteristics of the final shapes. The plate aspect ratio has a key role in determining the shape, as already noted for different stimuli-responsive plates in other studies. However, the difference between the elastic properties of the two layers to achieve different shapes is less important. It was shown as reinforcing fibers can be crucial to change this last statement. A better enforcing of cylinder-like shapes was observed when fibers are inserted in only one rather than two layers, and a larger suppression of the anticlastic curvature was observed by inserting fibers in both layers. The presence of fibers has been modeled with an extension of the Flory-Rehner free energy which accounts the hampering of swelling-induced deformations along the fibers direction.
The second bending process has been inspired by an experiment shown in [21], consisting in inducing the change of shape in bilayer sheets made of PDMS/(PDMS + silicone oil) through the total extraction of oil. It has been proposed here to describe, both experimentally and numerically, the bending of shrinking naturally curved beams and flat beams, and then, only numerically, the shape-morphing of cylindrical shells. The experimental results allowed to validate the explicit formula for the curvature of swelling beams also for shrinking beams, modeling the oil extraction as a bulk contraction.
The parametric computational study of cylindrical shells, where the oil extraction is modeled as a bulk contraction, has shown the possibility of quantifying the fraction of oil to put in the outer layer to get, after oil extraction, saddle-like shapes, everted cylindrical shells with axis orthogonal to the original one and doubly curved shapes.
The third bending process has been explored starting from the experiment described above, letting the oil initially contained in a single layer diffuse into the layer made of only PDMS, without extracting it, generating a progressive bending. The transient bending of a flat beam has been studied numerically and the results in terms of curvature have been compared with some experimental evidences. In addition, a simplified method to calculate the steady-state curvature has been proposed.

There are uncountable ideas that may be carried out in future to extend this study. For instance, some aspects that need attention are: the lack of a more suitable model to describe oil extraction, not simply considering it as an inelastic distortion; the lack of formulas that

identify the transition from sphere to cylinder in anisotropic gel plates; the expansion of the experiments to cylindrical shells and plates, also evaluating the possibility of introducing material anisotropies. Furthermore, as regards diffusion-induced bending, the effect of both internal diffusion, between layers, and external diffusion, outside the beam, may be considered, taking into account the different diffusion times, and the phenomenon can also be studied on more complex structures such as plates and shells.

LIST OF PAPERS

I **D. Battista**, V. Luchnikov, P. Nardinocchi. Shape-shifting of polymer beams and shells due to oil extraction. *Extreme Mechanics Letters* 36, 100655, 2020.
doi: 10.1016/j.eml.2020.100655

II **D. Battista**, M. Curatolo, P. Nardinocchi. Enforcing shaping of thin gel sheets by anisotropic swelling. *Mechanics of Materials Journal* 139, 103199, 2019.
doi: 10.1016/j.mechmat.2019.103199

III **D. Battista**, M. Curatolo, P. Nardinocchi. Swelling induced eversion and flattening in naturally curved gel beams. *International Journal of Mechanical Sciences* 161-162, 105071, 2019.
doi: 10.1016/j.ijmecsci.2019.105071

BIBLIOGRAPHY

[1] S. Armon, H. Aharoni, M. Moshe, and E. Sharon. "Shape selection in chiral ribbons: from seed pods to supramolecular assemblies." In: *Soft Matter* 10 (2014), pp. 2733–2740. DOI: 10.1039/C3SM52313F.

[2] S. Armon, E. Efrati, R. Kupferman, and E. Sharon. "Geometry and mechanics in the opening of chiral seed pods." In: *Science* 333.6050 (2011), pp. 1726–1730. DOI: 10.1126/science.1203874.

[3] A. Azam, K. E. Laflin, M. Jamal, R. Fernandes, and D. H. Gracias. "Self-folding micropatterned polymeric containers." In: *Biomedical Microdevices* 13 (2011), pp. 51–58. DOI: 10.1007/s10544-010-9470-x.

[4] H. Banerjee, M. Suhail, and H. Ren. "Hydrogel actuators and sensors for biomedical soft robots: brief overview with impending challenges." In: *Biomimetics* 3 (2018), p. 15. DOI: 10.3390/biomimetics3030015.

[5] N. Bassik, B. T. Abebe, K. E. Laflin, and D. H. Gracias. "Photolithographically patterned smart hydrogel based bilayer actuators." In: *Polymer* 51.26 (2010), pp. 6093–6098. DOI: 10.1016/j.polymer.2010.10.035.

[6] K. Bhattacharya and R. D. James. "The material is the machine." In: *Science* 307.5706 (2005), pp. 53–54. DOI: 10.1126/science.1100892.

[7] J. W. Boley, W. M. van Rees, C. Lissandrello, M. N. Horenstein, R. L. Truby, A. Kotikian, J. A. Lewis, and L. Mahadevan. "Shape-shifting structured lattices via multimaterial 4D printing." In: *Proceedings of the National Academy of Sciences* 116.42 (2019), pp. 20856–20862. DOI: 10.1073/pnas.1908806116.

[8] M. Byun, C. D. Santangelo, and R. C. Hayward. "Swelling-driven rolling and anisotropic expansion of striped gel sheets." In: *Soft Matter* 9 (2013), pp. 8264–8273. DOI: 10.1039/C3SM50627D.

[9] A. Di Carlo and S. Quiligotti. "Growth and balance." In: *Mechanics Research Communications* 29.6 (2002), pp. 449–456. DOI: 10.1016/S0093-6413(02)00297-5.

[10] T. Chen, H. Bakhshi, L. Liu, J. Ji, and S. Agarwal. "Combining 3D printing with electrospinning for rapid response and enhanced designability of hydrogel actuators." In: *Advanced Functional Materials* 28.19 (2018), p. 1800514. DOI: 10.1002/adfm.201800514.

[11] Y. Cheng, K. Ren, D. Yang, and J. Wei. "Bilayer-type fluorescence hydrogels with intelligent response serve as temperature/pH driven soft actuators." In: *Sensors and Actuators B: Chemical* 255 (2018), pp. 3117–3126. DOI: 10.1016/j.snb.2017.09.137.

[12] S. A. Chester and L. Anand. "A coupled theory of fluid permeation and large deformations for elastomeric materials." In: *Journal of the Mechanics and Physics of Solids* 58.11 (2010), pp. 1879 –1906. DOI: 10.1016/j.jmps.2010.07.020.

[13] B. D. Coleman and W. Noll. "The thermodynamics of elastic materials with heat conduction and viscosity." In: *Archive for Rational Mechanics and Analysis* 13 (1963), pp. 167–178. DOI: 10.1007/BF01262690.

[14] M. Curatolo, S. Gabriele, and L. Teresi. "Swelling and growth: a constitutive framework for active solids." In: *Meccanica* 52.14 (2017), pp. 3443–3456. DOI: 10.1007/s11012-017-0629-x.

[15] M. Curatolo and P. Nardinocchi. "Swelling-induced bending and pumping in homogeneous thin sheets." In: *Journal of Applied Physics* 124.8 (2018), p. 085108. DOI: 10.1063/1.5043580.

[16] M. Curatolo, P. Nardinocchi, E. Puntel, and L. Teresi. "Transient instabilities in the swelling dynamics of a hydrogel sphere." In: *Journal of Applied Physics* 122.14 (2017), p. 145109. DOI: 10.1063/1.5007229.

[17] Ch. Deneke, N.-Y. Jin-Phillipp, I. Loa, and O. G. Schmidt. "Radial superlattices and single nanoreactors." In: *Applied Physics Letters* 84.22 (2004), pp. 4475–4477. DOI: 10.1063/1.1755835.

[18] E. H. Dill. *Continuum Mechanics: Elasticity, Plasticity, Viscoelasticity*. CRC Press, 2007.

[19] M. Doi. "Gel Dynamics." In: *Journal of the Physical Society of Japan* 78.5 (2009), p. 052001. DOI: 10.1143/JPSJ.78.052001.

[20] E. Efrati, E. Sharon, and R. Kupferman. "Elastic theory of unconstrained non-Euclidean plates." In: *Journal of the Mechanics and Physics of Solids* 57.4 (2009), pp. 762 –775. DOI: 10.1016/j.jmps.2008.12.004.

[21] A. I. Egunov, J. G. Korvink, and V. A. Luchnikov. "Polydimethylsiloxane bilayer films with an embedded spontaneous curvature." In: *Soft Matter* 12 (2016), pp. 45–52. DOI: 10.1039/C5SM01139F.

[22] R. M. Erb, J. S. Sander, R. Grisch, and A. R. Studart. "Self-shaping composites with programmable bioinspired microstructures." In: *Nature Communications* 4.10 (2013), p. 1712. DOI: 10.1038/ncomms2666.

[23] D. Evangelista, S. Hotton, and J. Dumais. "The mechanics of explosive dispersal and self-burial in the seeds of the filaree, Erodium cicutarium (Geraniaceae)." In: *Journal of Experimental Biology* 214 (2011), pp. 521–529. DOI: 10.1242/jeb.050567.

[24] R. Fernandes and D. H. Gracias. "Self-folding polymeric containers for encapsulation and delivery of drugs." In: *Advanced Drug Delivery Reviews* 64.14 (2012), pp. 1579–1589. DOI: 10.1016/j.addr.2012.02.012.

[25] P J. Flory and J. Rehner. "Statistical mechanics of cross-linked polymer networks I. Rubberlike elasticity." In: *The Journal of Chemical Physics* 11.11 (1943), pp. 512–520. DOI: 10.1063/1.1723791.

[26] P J. Flory and J. Rehner. "Statistical mechanics of cross-linked polymer networks II. Swelling." In: *The Journal of Chemical Physics* 11.11 (1943), pp. 521–526. DOI: 10.1063/1.1723792.

[27] Y. Forterre, J. M. Skotheim, J. Dumais, and L. Mahadevan. "How the Venus flytrap snaps." In: *Nature* 433 (2005), pp. 421–425. DOI: 10.1038/nature03185.

[28] L. B. Freund. "Substrate curvature due to thin film mismatch strain in the nonlinear deformation range." In: *Journal of the Mechanics and Physics of Solids* 48.6 (2000), pp. 1159–1174. DOI: 10.1016/S0022-5096(99)00070-8.

[29] A. Goriely and M. Tabor. "Spontaneous helix hand reversal and tendril perversion in climbing plants." In: *Physical Review Letters* 80 (1998), pp. 1564–1567. DOI: 10.1103/PhysRevLett.80.1564.

[30] F. Guilak, D. M. Cohen, B. T. Estes, J. M. Gimble, W. Liedtke, and C. S. Chen. "Control of stem cell fate by physical interactions with the extracellular matrix." In: *Cell Stem Cell* 5.1 (2009), pp. 17–26. DOI: 10.1016/j.stem.2009.06.016.

[31] D. P. Holmes, M. Roché, T. Sinha, and H. A. Stone. "Bending and twisting of soft materials by non-homogenous swelling." In: *Soft Matter* 7 (2011), pp. 5188–5193. DOI: 10.1039/C0SM01492C.

[32] W. Hong, Z. Liu, and Z. Suo. "Inhomogeneous swelling of a gel in equilibrium with a solvent and mechanical load." In: *International Journal of Solids and Structures* 46.17 (2009), pp. 3282–3289. ISSN: 0020-7683. DOI: 10.1016/j.ijsolstr.2009.04.022.

[33] W. Hong, X. Zhao, J. Zhou, and Z. Suo. "A theory of coupled diffusion and large deformation in polymeric gels." In: *Journal of the Mechanics and Physics of Solids* 56.5 (2008), pp. 1779 –1793. DOI: 10.1016/j.jmps.2007.11.010.

[34] L. Ionov. "Biomimetic hydrogel-based actuating systems." In: *Advanced Functional Materials* 23.36 (2013), pp. 4555–4570. DOI: 10.1002/adfm.201203692.

[35] M. Jamal, S. S. Kadam, R. Xiao, F. Jivan, T.-M. Onn, R. Fernandes, T. D. Nguyen, and D. H. Gracias. "Bio-origami hydrogel scaffolds composed of photocrosslinked PEG bilayers." In: *Advanced Healthcare Materials* 2.8 (2013), pp. 1142–1150. DOI: 10.1002/adhm.201200458.

[36] S.-J. Jeon and R. C. Hayward. "Reconfigurable microscale frameworks from concatenated helices with controlled chirality." In: *Advanced Materials* 29.17 (2017), p. 1606111. DOI: 10.1002/adma.201606111.

[37] J. Kim, C. Kim, Y.S. Song, S.-G. Jeong, T.-S. Kim, and C.-S. Lee. "Reversible self-bending soft hydrogel microstructures with mechanically optimized designs." In: *Chemical Engineering Journal* 321 (2017), pp. 384–393. DOI: 10.1016/j.cej.2017.03.125.

[38] Y. Kim, J. van den Berg, and A. J. Crosby. "Autonomous snapping and jumping polymer gels." In: *Nature Materials* 20 (2021), pp. 1695–1701. DOI: 10.1038/s41563-020-00909-w.

[39] G. Kofod, H. Stoyanov, and R. Gerhard. "Multilayer coaxial fiber dielectric elastomers for actuation and sensing." In: *Applied Physics A* 102 (2011), pp. 577–581. DOI: 10.1007/s00339-010-6066-5.

[40] H. Lee, C. Xia, and N. X. Fang. "First jump of microgel; actuation speed enhancement by elastic instability." In: *Soft Matter* 6 (2010), pp. 4342–4345. DOI: 10.1039/C0SM00092B.

[41] T. G. Leong, C. L. Randall, B. R. Benson, N. Bassik, G. M. Stern, and D. H. Gracias. "Tetherless thermobiochemically actuated microgrippers." In: *Proceedings of the National Academy of Sciences* 106.3 (2009), pp. 703–708. DOI: 10.1073/pnas.0807698106.

[42] S. Li and K. W. Wang. "Plant-inspired adaptive structures and materials for morphing and actuation: a review." In: *Bioinspiration & Biomimetics* 12.1 (2016), p. 011001. DOI: 10.1088/1748-3190/12/1/011001.

[43] X. Li, X. Cai, Y. Gao, and M. J. Serpe. "Reversible bidirectional bending of hydrogel-based bilayer actuators." In: *Journal of Materials Chemistry B* 5 (2017), pp. 2804–2812. DOI: 10.1039/C7TB00426E.

[44] Y. Liu, H. Du, L. Liu, and J. Leng. "Shape memory polymers and their composites in aerospace applications: a review." In: *Smart Materials and Structures* 23.2 (2014), p. 023001. DOI: 10.1088/0964-1726/23/2/023001.

[45] Z. Liu, A. Cui, J. Li, and C. Gu. "Folding 2D structures into 3D configurations at the micro/nanoscale: principles, techniques, and applications." In: *Advanced Materials* 31.4 (2019), p. 1802211. DOI: 10.1002/adma.201802211.

[46] C. Llorens, M. Argentina, N. Rojas, J. Westbrook, J. Dumais, and X. Noblin. "The fern cavitation catapult: mechanism and design principles." In: *Journal of The Royal Society Interface* 13.114 (2016), p. 20150930. DOI: 10.1098/rsif.2015.0930.

[47] A. Lucantonio, P. Nardinocchi, and M. Pezzulla. "Swelling-induced and controlled curving in layered gel beams." In: *Proceedings of the Royal Society A: Mathematical, Physical and Engineering Science* 470.2171 (2014). DOI: 10.1098/rspa.2014.0467.

[48] A. Lucantonio, P. Nardinocchi, and L. Teresi. "Transient analysis of swelling-induced large deformations in polymer gels." In: *Journal of the Mechanics and Physics of Solids* 61.1 (2013), pp. 205–218. DOI: 10.1016/j.jmps.2012.07.010.

[49] A. Lucantonio, M. Roche, P. Nardinocchi, and H. A. Stone. "Buckling dynamics of a solvent-stimulated stretched elastomeric sheet." In: *Soft Matter* 10 (2014), pp. 2800–2804. DOI: 10.1039/C3SM52941J.

[50] V. Luchnikov, O. Sydorenko, and M. Stamm. "Self-rolled polymer and composite polymer/metal micro- and nanotubes with patterned inner walls." In: *Advanced Materials* 17.9 (2005), pp. 1177–1182. DOI: 10.1002/adma.200401836.

[51] T. van Manen, S. Janbaz, and A. A. Zadpoor. "Programming the shape-shifting of flat soft matter." In: *Materials Today* 21.2 (2018), pp. 144–163. DOI: 10.1016/j.mattod.2017.08.026.

[52] P. Marmottant, A. Ponomarenko, and D. Bienaimé. "The walk and jump of Equisetum spores." In: *Proceedings of the Royal Society B: Biological Sciences* 280.1770 (2013), p. 20131465. DOI: 10.1098/rspb.2013.1465.

[53] P. H. Masson, M. Tasaka, M. T. Morita, C. Guan, R. Chen, and K. Boonsirichai. "Arabidopsis thaliana: a model for the study of root and shoot gravitropism." In: *The Arabidopsis Book* 2002.1 (2002). DOI: 10.1199/tab.0043.

[54] J. Merodio and R. W. Ogden. "Mechanical response of fiber-reinforced incompressible non-linearly elastic solids." In: *International Journal of Non-Linear Mechanics* 40.2-3 (2005), pp. 213–227. DOI: 10.1016/j.ijnonlinmec.2004.05.003.

[55] S. Miyashita, L. Meeker, M. T Tolley, R. J Wood, and D. Rus. "Self-folding miniature elastic electric devices." In: *Smart Materials and Structures* 23.9 (2014), p. 094005. DOI: 10.1088/0964-1726/23/9/094005.

[56] C. D. Modes and M. Warner. "Negative Gaussian curvature from induced metric changes." In: *Physical Review E* 92 (2015), p. 010401. DOI: 10.1103/PhysRevE.92.010401.

[57] C. Mostajeran, M. Warner, T. H. Ware, and T. J. White. "Encoding Gaussian curvature in glassy and elastomeric liquid crystal solids." In: *Proceedings of the Royal Society A: Mathematical, Physical and Engineering Sciences* 472.2189 (2016), p. 20160112. DOI: 10.1098/rspa.2016.0112.

[58] J. L. Mullen, E. Turk, K. Johnson, C. Wolverton, H. Ishikawa, C. Simmons, D. Söll, and M. L. Evans. "Root-growth behavior of the Arabidopsis Mutantrgr1." In: *Plant Physiology* 118.4 (1998), pp. 1139–1145. DOI: 10.1104/pp.118.4.1139.

[59] P. Nardinocchi, M. Pezzulla, and L. Teresi. "Anisotropic swelling of thin gel sheets." In: *Soft Matter* 11 (2015), pp. 1492–1499. DOI: 10.1039/C4SM02485K.

[60] P. Nardinocchi, M. Pezzulla, and L. Teresi. "Steady and transient analysis of anisotropic swelling in fibered gels." In: *Journal of Applied Physics* 118.24 (2015), p. 244904. DOI: 10.1063/1.4938737.

[61] P. Nardinocchi and E. Puntel. "Finite bending solutions for layered gel beams." In: *International Journal of Solids and Structures* 90 (2016), pp. 228–235. DOI: 10.1016/j.ijsolstr.2016.02.026.

[62] P. Nardinocchi and E. Puntel. "Unexpected hardening effects in bilayered gel beams." In: *Meccanica* 52.14 (2017), pp. 3471–3480. DOI: 10.1007/s11012-017-0635-z.

[63] P. Nardinocchi and L. Teresi. "Actuation performances of anisotropic gels." In: *Journal of Applied Physics* 120.21 (2016), p. 215107. DOI: 10.1063/1.4969046.

[64] M. S. Oh, Y. S. Song, C. Kim, J. Kim, J. B. You, T.-S. Kim, C.-S. Lee, and S. G. Im. "Control of reversible self-bending behavior in responsive Janus microstrips." In: *ACS Applied Materials & Interfaces* 8.13 (2016), pp. 8782–8788. DOI: 10.1021/acsami.5b12704.

[65] K. Oliver, A. Seddon, and R. S. Trask. "Morphing in nature and beyond: a review of natural and synthetic shape-changing materials and mechanisms." In: *Journal of Materials Science* 51.24 (2016), pp. 10663–10689. DOI: 10.1007/s10853-016-0295-8.

[66] M. Pezzulla, G. P. Smith, P. Nardinocchi, and D. P. Holmes. "Geometry and mechanics of thin growing bilayers." In: *Soft Matter* 12 (2016), pp. 4435–4442. DOI: 10.1039/C6SM00246C.

[67] M. Pezzulla, N. Stoop, X. Jiang, and D. P. Holmes. "Curvature-driven morphing of non-Euclidean shells." In: *Proceedings of the Royal Society A: Mathematical, Physical and Engineering Sciences* 473.2201 (2017), p. 20170087. DOI: 10.1098/rspa.2017.0087.

[68] S. Poppinga, C. Zollfrank, O. Prucker, J. Rühe, A. Menges, T. Cheng, and T. Speck. "Toward a new generation of smart biomimetic actuators for architecture." In: *Advanced Materials* 30.19 (2018), p. 1703653. DOI: 10.1002/adma.201703653.

[69] C. L. Randall, E. Gultepe, and D. H. Gracias. "Self-folding devices and materials for biomedical applications." In: *Trends in Biotechnology* 30.3 (2012), pp. 138–146. DOI: 10.1016/j.tibtech.2011.06.013.

[70] Y. Sawa, F. Ye, K. Urayama, T. Takigawa, V. Gimenez-Pinto, R. L. B. Selinger, and J. V. Selinger. "Shape selection of twist-nematic-elastomer ribbons." In: *Proceedings of the National Academy of Sciences* 108.16 (2011), pp. 6364–6368. DOI: 10.1073/pnas.1017658108.

[71] M. Schenk and S. D. Guest. "Geometry of Miura-folded metamaterials." In: *Proceedings of the National Academy of Sciences* 110.9 (2013), pp. 3276–3281. DOI: 10.1073/pnas.1217998110.

[72] E. Sharon, M. Marder, and H. Swinney. "Leaves, flowers and garbage bags: making waves." In: *American Scientist* 92 (2004), pp. 254–261. DOI: 10.1511/2004.47.932.

[73] Y. Shen, Y. Pang, J. Wang, H. Ma, Z. Pei, and S. Qu. "Origami-inspired metamaterial absorbers for improving the larger-incident angle absorption." In: *Journal of Physics D: Applied Physics* 48.44 (2015), p. 445008. DOI: 10.1088/0022-3727/48/44/445008.

[74] W. K. Silk. "On the curving and twining of stems." In: *Environmental and Experimental Botany* 29.1 (1989), pp. 95–109. DOI: 10.1016/0098-8472(89)90042-7.

[75] E. J. Smith, W. Xi, D. Makarov, I. Mönch, S. Harazim, V. A. Bolaños Quiñones, C. K. Schmidt, Y. Mei, S. Sanchez, and O. G. Schmidt. "Lab-in-a-tube: ultracompact components for on-chip capture and detection of individual micro-/nanoorganisms." In: *Lab Chip* 12 (2012), pp. 1917–1931. DOI: 10.1039/C2LC21175K.

[76] Z. Song, T. Ma, R. Tang, Q. Cheng, X. Wang, D. Krishnaraju, R. Panat, C. K. Chan, H. Yu, and H. Jiang. "Origami lithium-ion batteries." In: *Nature Communications* 5 (2014), p. 3140. DOI: 10.1038/ncomms4140.

[77] Anthony J.M. Spencer. *Continuum Theory of the Mechanics of Fibre-Reinforced Composites*. Springer-Verlag, 1984.

[78] R. Stahlberg. "The phytomimetic potential of three types of hydration motors that drive nastic plant movements." In: *Mechanics of Materials* 41.10 (2009), pp. 1162–1171. DOI: 10.1016/j.mechmat.2009.05.003.

[79] G. V. Stoychev and L. Ionov. "Actuating fibers: design and applications." In: *ACS Applied Materials & Interfaces* 8.37 (2016), pp. 24281–24294. DOI: 10.1021/acsami.6b07374.

[80] G. Stoychev, L. Guiducci, S. Turcaud, J. W. C. Dunlop, and L. Ionov. "Hole-programmed superfast multistep folding of hydrogel bilayers." In: *Advanced Functional Materials* 26.42 (2016), pp. 7733–7739. DOI: 10.1002/adfm.201602394.

[81] G. Stoychev, S. Turcaud, J. W. C. Dunlop, and L. Ionov. "Hierarchical multi-step folding of polymer bilayers." In: *Advanced Functional Materials* 23.18 (2013), pp. 2295–2300. DOI: 10.1002/adfm.201203245.

[82] Ch. Strelow, H. Rehberg, C. M. Schultz, H. Welsch, Ch. Heyn, D. Heitmann, and T. Kipp. "Optical microcavities formed by semiconductor microtubes using a bottlelike geometry." In: *Physical Review Letters* 101 (2008), p. 127403. DOI: 10.1103/PhysRevLett.101.127403.

[83] A. Sydney Gladman, E. A. Matsumoto, R. G. Nuzzo, L. Mahadevan, and J. A. Lewis. "Biomimetic 4D printing." In: *Nature Materials* 15 (2016), pp. 413–418. DOI: 10.1038/nmat4544.

[84] Y. Tao et al. "Morphing pasta and beyond." In: *Science Advances* 7.19 (2021). DOI: 10.1126/sciadv.abf4098.

[85] L. Teresi and V. Varano. "Modeling helicoid to spiral-ribbon transitions of twist-nematic elastomers." In: *Soft Matter* 9 (2013), pp. 3081–3088. DOI: 10.1039/C3SM27491H.

[86] H. Thérien-Aubin, Z. L. Wu, Z. Nie, and E. Kumacheva. "Multiple shape transformations of composite hydrogel sheets." In: *Journal of the American Chemical Society* 135.12 (2013), pp. 4834–4839. DOI: 10.1021/ja400518c.

[87] S. Timoshenko. "Analysis of bimetal thermostats." In: *Journal of the Optical Society of America* 11 (1925), pp. 233–255. DOI: 10.1364/JOSA.11.000233.

[88] G. Wang, F. Qin, H. Liu, Y. Tao, Y. Zhang, Y. J. Zhang, and L. Yao. "MorphingCircuit: an integrated design, simulation, and fabrication workflow for self-morphing electronics." In: *Proceedings of the ACM Interactive, Mobile, Wearable Ubiquitous Technologies* 4.4 (2020). DOI: 10.1145/3432232.

[89] J. Wang, X. Zhang, A. Wang, X. Hu, L. Deng, L. Lou, and H. Shen. "The synthesis and simulations of solvent-responsive bilayer hydrogel." In: *Polymer* 204 (2020), p. 122801. DOI: 10.1016/j.polymer.2020.122801.

[90] M. Warner, C. D. Modes, and D. Corbett. "Curvature in nematic elastica responding to light and heat." In: *Proceedings of the Royal Society A: Mathematical, Physical and Engineering Sciences* 466.2122 (2010), pp. 2975–2989. DOI: 10.1098/rspa.2010.0135.

[91] M. Warner, C. D. Modes, and D. Corbett. "Suppression of curvature in nematic elastica." In: *Proceedings of the Royal Society A: Mathematical, Physical and Engineering Sciences* 466.2124 (2010), pp. 3561–3578. DOI: 10.1098/rspa.2010.0139.

[92] W. Wei, P. Xiao, V. K. Thakur, I. Chianella, and S. Li. "Smart bilayer polymer reactor with cascade/non-cascade switching catalyst characteristics." In: *Materials Today Chemistry* 17 (2020), p. 100279. DOI: 10.1016/j.mtchem.2020.100279.

[93] H. G. Wood and J. A. Hanna. "Contrasting bending energies from bulk elastic theories." In: *Soft Matter* 15 (2019), pp. 2411–2417. DOI: 10.1039/C8SM02297F.

[94] J. Wu, C. Yuan, Z. Ding, M. Isakov, Y. Mao, T. Wang, M. L. Dunn, and H. J. Qi. "Multi-shape active composites by 3D printing of digital shape memory polymers." In: *Scientific Reports* 6 (2016), p. 24224. DOI: 10.1038/srep24224.

[95] F. Yang and J. C. M. Li. "Diffusion-induced beam bending in hydrogen sensors." In: *Journal of Applied Physics* 93.11 (2003), pp. 9304–9309. DOI: 10.1063/1.1569980.

[96] X. Zhang, X. Xu, L. Chen, C. Zhang, and L. Liao. "Multi-responsive hydrogel actuator with photo-switchable color changing behaviors." In: *Dyes and Pigments* 174 (2020), p. 108042. DOI: 10.1016/j.dyepig.2019.108042.

[97] Z. Zhao, X. Kuang, C. Yuan, H. J. Qi, and D. Fang. "Hydrophilic/hydrophobic composite shape-shifting structures." In: *ACS Applied Materials & Interfaces* 10.23 (2018), pp. 19932–19939. DOI: 10.1021/acsami.8b02444.

[98] S. Y. Zheng, C. Y. Li, M. Du, J. Yin, J. Qian, Z. L. Wu, and Q. Zheng. "Programmable deformations of biomimetic composite hydrogels embedded with printed fibers." In: *ACS Applied Materials & Interfaces* 12.51 (2020), pp. 57497–57504. DOI: 10.1021/acsami.0c19656.